

PREDICTION OF INTERFACE FAILURE PROBABILITY
IN BI-MATERIAL CERAMIC JOINTS

Zur Erlangung des akademischen Grades
Doktor der Ingenieurwissenschaften
der Fakultät für Maschinenbau
Karlsruher Institut für Technologie (KIT)

genehmigte

Dissertation

von

M.Sc. Iryna Melikayeva
geboren am 13.11.1985
in Dnipropetrowsk, Ukraine

Tag der mündlichen Prüfung: 30.05.2011
Hauptreferent: Prof. Dr. rer. nat. Oliver Kraft
Korreferent: Prof. Dr. Volodymyr Loboda

Abstract

Bi-material ceramic joints are used in a number of engineering structures to enhance the functionality and lifetime of technological components. On the other hand, delamination of material composites, caused by the growth of natural flaws at material interfaces, can lead to catastrophic failure of the whole component and loss of the components functionality.

Since interface failure of brittle composites is determined by the scatter of interface flaws, the reliability must be evaluated based on probabilistic methods such as the Weibull theory. In the present work, the Weakest Link approach will be generalized for the case of bi-material ceramic joints in order to extend the probabilistic model available for homogeneous materials. Here, a fracture mechanics model is developed to obtain a failure criterion for interface cracks. It is shown that the interface failure probability becomes a function of the crack tip mode-mixity state. The mode-mixity influence is assessed for a general loading case of a bi-material strip with an internal interface crack. A simplified analysis, possible in the case of gradually varying stress fields, leads to a conservative assessment of the failure probability for interface cracks.

An adequate fracture mechanics algorithm for the prediction of the unstable propagation of interface natural flaws is developed in this work, allowing implementation into the finite element post-processor STAU. A parametric study is performed to relate limited experimental data for a specific interface system to reliability predictions of two possible specimen configurations.

The probabilistic framework that was developed constitutes an important step in the generalization of the Weakest Link Approach to interface failure. An essential aspect is that it allows predicting the interface failure in ceramic components in the design stage. Thus, this approach contributes to increase the

reliability of industrial applications and facilitates a systematic planning of reliability experiments.

Kurzzusammenfassung

Keramische Verbundwerkstoffe werden in einer Reihe von industriellen Bauteilen verwendet, um die Funktionalität und Lebensdauer von technischen Komponenten zu verbessern. Durch das Wachstum natürlicher Fehler an den Materialgrenzflächen kann es jedoch zu Delamination und somit zum katastrophalen Versagen des gesamten Bauteils und dem Verlust der Funktionalität der Komponente kommen.

Da das Versagen spröder Verbundwerkstoffe von der Streuung der Defekte in der Grenzfläche abhängt, muss die Zuverlässigkeit solcher Materialien auf Basis probabilistischer Methoden wie der Weibull Theorie ausgewertet werden. In der vorliegenden Arbeit wird der Weakest-Link-Ansatz für den Fall einer keramischen Grenzfläche verallgemeinert, um das probabilistische Modell für homogene Materialien zu erweitern. Hierfür wird ein bruchmechanisches Modell entwickelt, um ein Versagenskriterium für Grenzflächenrisse zu erhalten. Es wird gezeigt, dass die Versagenswahrscheinlichkeit der Grenzfläche eine Funktion des Mixed-Mode Zustands an der Rissspitze ist. Diese Mixed-Mode-Abhängigkeit wird für einen verallgemeinerten Belastungsfall anhand eines Risses in der Grenzfläche hergeleitet. Für schwach variierende Spannungsfelder erhält man einen konservativen Ansatz zur Vorhersage der Versagenswahrscheinlichkeit im Fall von Grenzflächenrissen.

In der vorliegenden Arbeit wird ein geeigneter Algorithmus zur Vorhersage der instabilen Ausbreitung natürlicher Fehler an Grenzflächen entwickelt und in das Programm STAU (Post-Prozessor einer Finite-Elemente Analyse) implementiert. Anhand einer Parameterstudie wird eine begrenzte experimentelle Datenbasis für ein spezifisches Grenzflächensystem mit Zuverlässigkeitsvorhersagen von zwei möglichen Komponentenkonfigurationen verbunden.

Die entwickelten probabilistischen Methoden sind ein wichtiger Beitrag zur Verallgemeinerung des Weakest-Link-Ansatz für Grenzflächenversagen. Ein wesentlicher Aspekt hierbei ist, dass das Grenzflächenversagen keramischer Verbundwerkstoffen bereits in der Planungsphase berücksichtigt werden kann. Somit trägt diese Arbeit dazu bei, die Zuverlässigkeit von Komponenten aus keramischem Verbundmaterial zu verbessern und die systematische Planung von Zuverlässigkeitstests zu ermöglichen.

Table of contents

Abstract.....	iii
Kurzzusammenfassung	v
List of symbols and Abbreviations	ix
1. Introduction	1
1.1 Motivation	1
1.2 State of the art.....	3
1.3 Overview of chapters.....	4
2. Fracture mechanics of interfaces.....	7
2.1 Role of interfaces	7
2.2 Mechanical behaviour, Dundurs' parameters	10
2.3 Interface stress singularities	13
2.4 Interface fracture mechanical parameters	16
2.5 Fracture resistance of interfaces	18
2.5.1 Crack kinking out of the interface	19
2.5.2 Crack propagation along the interface	23
3. Statistical aspects of failure	27
3.1 Basic ideas of the weakest-link approach	27
3.2 Weibull theory for brittle homogeneous materials.....	31
3.3 Numerical integration	33
3.3.1 Finite element postprocessor STAU.....	33
3.3.2 Gaussian integration method	34
3.4 Generalization for the case of interface flaws.....	36
3.5 Discussion of results	40

4. Mechanical problem of a bi-material strip	43
4.1 Mathematical statement of the problem	44
4.2 Solution procedure	45
4.2.1 Crack-free bi-material strip of infinite length.....	46
4.2.1.1 Derivation of singular integral equations	46
4.2.1.2 Numerical method for the solution of singular integral equations..	50
4.2.1.3 Verification of the solution procedure.....	51
4.2.2 An interface crack in an infinite bi-material joint.....	53
4.2.2.1 Derivation of the Hilbert problem	54
4.2.2.2 Solution procedure for the Hilbert problem	56
4.3 Parametric study and discussion of the results	57
5. Experimental characterization of material and interface strength	63
5.1 Estimation of Weibull parameters.....	63
5.2 Interface strength considerations	66
5.3 Discussion of results	70
6. Numerical study and discussions	73
6.1 Crack models under consideration.....	73
6.2 Stress analysis of interfaces	76
6.2.1 Two-dimensional finite element models	77
6.2.2 Three-dimensional finite element models.....	79
6.2.3 Equivalent stress and mode-mixity parameter	83
6.3 Interface failure probability results.....	86
6.3.1 Parametric study.....	86
6.3.2 Role of the mode-mixity parameter	91
6.4 Discussion.....	92
7. Summary	97
Reference list.....	101
Appendix A	109
Appendix B	115
Acknowledgement	119

List of symbols and Abbreviations

<i>Roman characters</i>	
Symbol	Description
a	Interface crack length
a_0	Minimum possible crack size
a_{cr}	Critical crack size
a_k	Length of a kinked crack
A_0	Surface unit area
A_i	Surface of interface
b	Weibull parameter (strength)
E_n	Young's modulus of material "n"
$f_a(a), f_V(\bar{x}), f_\Omega(\omega)$	Probability density functions of crack size, crack location and orientation, correspondingly
f_1, f_2	Unknown stress functions
g_1, g_2, g_3, g_4	Unknown displacement functions
G_i	Interface energy release rate
G_{Icr}	Pure mode-I toughness of interface
G_{icr}	Interface toughness
G_k	Energy release rate for kinked crack
$\vec{h}_i, h_{ix}, h_{iy}$	Weight functions for stress intensity factors
h_n	Height of material "n"
H_1, H_2	Bi-material constants
H_V	Normalized stress integral

List of symbols and Abbreviations

Symbol	Description
J_A, J_V, J_Ω	Jacobian determinants
K	Complex stress intensity factor
K_1, K_2	Real and imaginary components of stress intensity factor, correspondingly
K_I, K_{II}, K_{III}	Conventional stress intensity factors
K_{Icr}	Material toughness
K_{eq}	Equivalent complex stress intensity factor
K_T	Thermally induced stress intensity factor
L	Characteristic length
L_f	Likelihood function
L_N	Legendre polynomials
m	Weibull parameter (scatter of strength)
M_0	Average number of flaws in unit volume/surface
n	Number of material in joint
P	Applied normal stress
P_F	Failure probability
P_S	Survival probability
Q	Applied shear stress
r	Radial coordinate in cylindrical coordinate system
R	Radius of Brazilian disk
$U_i^{(n)}$	"i"-th component of displacement in material "n"
V_0	Unit volume
V_{eff}	Effective volume integral
Y_i	Geometry weight-function
x, y, z	Coordinates in Cartesian system

<i>Greek characters</i>	
Symbol	Description
α	1-st Dundur's parameter
α_T	Coefficient of thermal expansion
β	2-nd Dundur's parameter
δ	Distance from the crack tip along interface
ε	Oscillatory index
ϕ	Mode-mixity parameter (amount of out-of-plane stress to in-plane stresses)
Γ	Gamma-function
η_n	Quantity inversely proportional to height of material "n"
θ	Tangential coordinate in cylindrical coordinate system
λ_n	Lamé constant in material "n"
μ_n	Shear modulus in material "n"
ν_n	Poisson ratio in material "n"
σ_0	Characteristic strength parameter
σ^*	Reference stress
σ_{eq}	Equivalent stress
$\sigma_{kl}^{(n)}$	Component of stress tensor in material "n"
σ_n	Normal stress along the interface
σ_τ	Shear stress along the interface
ψ	Mode-mixity parameter (amount of shear stress to tensile stresses)
ω	Angle of crack orientation
ω_k	Angle of crack kinking
Ω	Range of possible crack orientations

Abbreviations

Symbol	Description
2D- / 3D model	Two- / three dimensional model
4PB	Four point bending
cSIF	Complex stress intensity factor
ERR	Energy release rate
FE	Finite Element
iERR	Interface energy release rate
MLM	Maximum Likelihood method
PDF	Probability density function
SEM	Scanning Electron Microscopy
SIE	Singular integral equations
SIF	Stress intensity factor
STAU	Acronym for Weakest-link Finite Element Postprocessing Program



1. Introduction

In this work the classical Weibull theory, used for failure probability calculations, is generalized for the case of interface failure in ceramic-ceramic joints.

1.1 Motivation

Ceramic materials are often used in high temperature applications because of their attractive chemical and mechanical properties compared to metals and polymers. The main features of ceramic materials are low density, high strength at high temperatures, resistance to wear and corrosion combined with low electrical and thermal conductivity [53]. Today, functional properties of ceramics gain increasingly importance. However, the inherent brittleness of ceramics is limiting their use in many applications.

In order to increase the usage efficiency of ceramic materials new ceramic composite components, and ceramic composites, have been developed. A composite was originally considered to be a combination of two materials, but now this class of materials is regarded as any material combination, which possesses structural or functional properties not present in any individual component. The main concept of use of composites is the aim to design and manufacture a new range of functional or structural materials that beneficially combine the optional properties of its contents. Except the functional needs, another more global goal of the “material efficiency” is to provide a significant reduction in the total environmental cost of the world economy. The idea of substituting the existing materials by e.g. their combinations with the same or better properties in order to have a reduced material impact was described by Allwood et al. [3].

1. Introduction

Nowadays, most functional engineering structures are generally made of materials with different elastic and physical properties. The most common area of application is, of course, automobile industry. One typical example is a Lambda-sensor – an electronic device, the size of finger, that measures the proportion of oxygen in the exhaust gas. This ceramic element contains a number of interfaces as can be seen in [Figure 1.1a](#). Under periodically changing temperature conditions special attention should be paid to the mechanical behaviour of the material joints. Another surprising reason of interface damage in this device can be caused by an external voltage applied to the Zirconia Lambda sensors, for example during their checking with an ohmmeter.

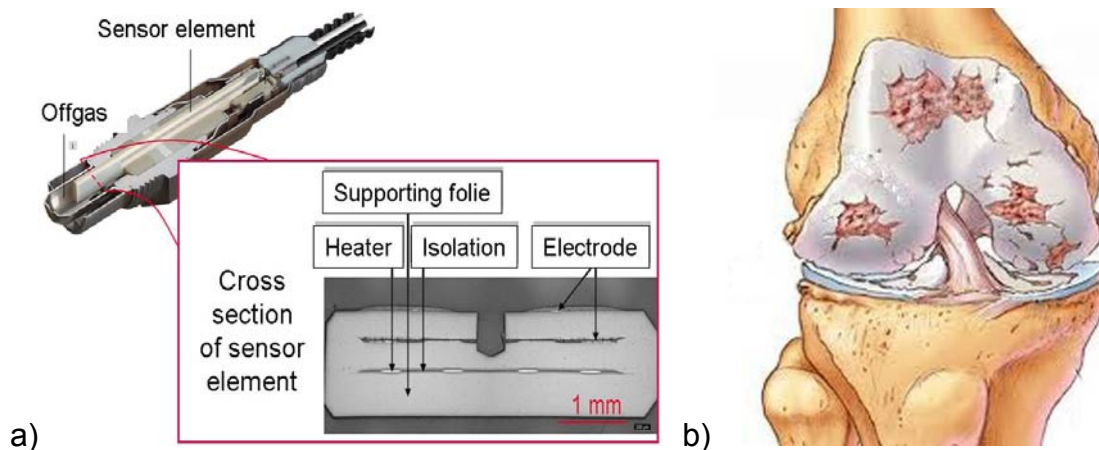


Figure 1.1 – Application examples of ceramic material joints: a) Lambda-sensor [13]; b) knee implant [65]

Another prominent example, where the behaviour of material joints is very important nowadays is orthopaedic surgery. In [Figure 1.1b](#) one can see an advanced arthritis and avascular necrosis of the knee. When non-surgical and arthroscopic therapy no longer provides satisfactory results, joint replacement is a necessary treatment. In this case the reliability of bone-implant interfaces (e.g. bone-cement interface) becomes a primary problem, regarding the high wear characteristics of the mechanics and motion. Ceramic implants are also often used as dentures, due to their improved physical and biomechanical properties, including high bending and fracture resistance. Again, the reliability of interfaces between the denture material and tooth is critical.

These examples illustrate that the area of ceramic bi-materials is very wide. The behaviour of bonded joints in all these structures plays an important role,

especially in transient service conditions, where interfacial cracks at material joints are of special concern with respect to the reliability of the whole component.

1.2 State of the art

The fracture mechanics assessment of interface failure was considered in a large number of papers dealing with different aspects. The main aspects of interface cracks are the mixed-mode character of crack tip fields even for pure mode-I remote loading (i.e. crack tip tensile and shear effects are inseparable), the presence of oscillatory singularities in the elastic stress and displacement fields [21, 24], the choice of an appropriate crack tip model for the definition of fracture parameters [19, 37], and selection of a suitable fracture criterion [25, 40, 61].

The statistical aspect of the analysis of fracture by relating strength to microstructure was provided by a number of authors (e.g. Neville and Knott [58] using order statistics for various kinds of microstructure; Zweben and Rosen [75] using a representative volume approach) for homogeneous as well as for inhomogeneous materials, including the case of fibrous fracture. The probabilistic models have also been developed to analyze the fracture stresses in metals (Lin et al [43] for brittle transgranular cleavage fracture; Poncelet et al [60] for high cycle fatigue failure; Wu and Knott [72] for the modelling of degradation processes). In most cases, a local approach [11] based on weakest-link type fracture is used, even if plastic deformation precedes cleavage fracture.

Failure probability of brittle ceramic materials is generally assessed using Weibull theory [70] with fracture mechanics extensions [9, 26, 49], where failure of the whole component occurs if the most unfavourable flaw or crack becomes critical. Appropriate numerical tools for a corresponding reliability analysis are available (Cares/Life [57], STAU [14, 36]). The fracture mechanics failure description used in the reliability tools is based on a number of assumptions, including the assumption that stresses can be considered constant along the crack faces. In the case of bi-material ceramic joints the stress field depends on the material combination and changes significantly along the faces of interface flaws or cracks ([19, 25, 61]). Consequently, classical Weibull failure theory

needs to be modified in order to properly take into account the high stress gradients. While high stress gradient generalizations already exist in the case of homogeneous materials [15], the aim of the present work is to generalize the Weibull approach for the case of interface fracture. In particular, the interface mode-mixity parameter should be included to calculate the failure probability of the interface.

1.3 Overview of chapters

In order to obtain the appropriate theory for determining the interface failure probability, suitable probabilistic and fracture mechanics methods have to be combined. The fracture mechanics of interfaces is discussed in Chapter 2. The main criteria of interface crack propagation as well as mechanical behaviour of interface stresses are treated. In Chapter 3 the statistical aspects of failure phenomenon are introduced. The Weibull theory is generalized to the case of interface failure according to the weakest-link approach and a fracture mechanical model, which is based on the energy release rate fracture criterion. The comparison of the interface statistical model with ordinary Weibull theory for brittle homogeneous materials shows an appearance of a new term, which measures the mode-mixity of the stress state. In order to determine the impact of this parameter on interface failure probability a detailed analysis of stress state at the interface of a bi-material strip is presented in Chapter 4. The solution procedure requires to split the main problem into two special cases. Their superposition gives the solution for the general case with arbitrary boundary conditions. The mathematical statement of the problem is given in the form of a system of singular integral equations, which are solved numerically. The values of mode-mixity parameter ψ , can be calculated near the tip of internal crack for any remote loading case, after the influence of this parameter on the interface failure probability is studied.

Eventually, an experimental characterization of bi-materials is also important in order to gain statistical data corresponding to the strength of interfaces. Sample configurations and test setups, as well as methods of data evaluation are described in Chapter 5. A numerical stress evaluation, including calculation of equivalent stresses and mode-mixity parameters, is presented in

Chapter 6. Using finite element analysis results, an algorithm for interface failure probability determination is introduced with the purpose to study the role of Weibull parameters. Moreover, the role of different crack models, such as “through-wall” crack model and “penny-shaped” crack model, was studied. At the end some recommendations for future experimental analysis are given.

The results of this work allow the implementation of modified Weibull theory into the existing version of STAU-program, which will be used for the interface failure probability calculations of different bi-material components under different mechanical loading conditions.



2. Fracture mechanics of interfaces

Ceramic composites have been developed for enhancing the strength and reliability of ceramic components. For this instance, they allow to improve fracture toughness of the whole component by the means of energy release mechanisms (crack deflection [34] or crack bifurcation (e.g. [32, 59])). On the one hand, interfaces can be treated as obstacles for the propagation of the cracks that have been originated in the individual materials. On the other hand, interface cracks or cracks kinked from interface into the base material can lead to the failure of the whole joint. Such interface cracks and their role for component damage is considered in this work. Therefore, the quality of interface between joined materials is one of the characteristic features in composites. In this section, the main properties of bi-materials, such as mechanical compatibility, mismatch in elastic properties over the interface, interface toughness and interface crack behaviour, are discussed.

2.1 Role of interfaces

The joined components consist of different materials and usually such composite materials or material joints fail by initiation or propagation of natural flaws in highly stressed interfacial regions. It is proper to distinguish two different kinds of interfaces: those which have low strength and/or toughness, so called weak interfaces, and those which are nearly ideally strong, and thereby promote perfect adherence and can be considered as a strong interfaces.

Weak interfaces assume that the stiffness of joined materials is higher than the stiffness of interface layers. During the fracture process the propagating crack kinks into the weak interface, where it continues to grow (i.e. to form a delamination crack). [Figure 2.1](#) schematically shows a load – deflection diagram

2. Fracture mechanics of interfaces

of a bending test on a material composite which contains weak interfaces. The behaviour of the same monolithic ceramic without interfaces is shown for comparison. The first part of the laminate curve is identical with the curve of monolith. At the point A the first lamina breaks, but the load can be increased to drive the delamination crack forward. Each load drop corresponds to the failure of one individual material layer. Subsequently the crack is deflected into the interface again. Failure continues in the same manner and this gives the typical saw-tooth shaped load-deflection diagram for laminates with weak interfaces [46].

This example illustrates that forming of ceramic composites in the configuration of layered system with weak interfaces is one of the ways to fabricate stronger and tougher ceramic components. An additional advantage of such layered systems is the possibility to prevent catastrophic spontaneous fracture, which is inherent to ceramics.

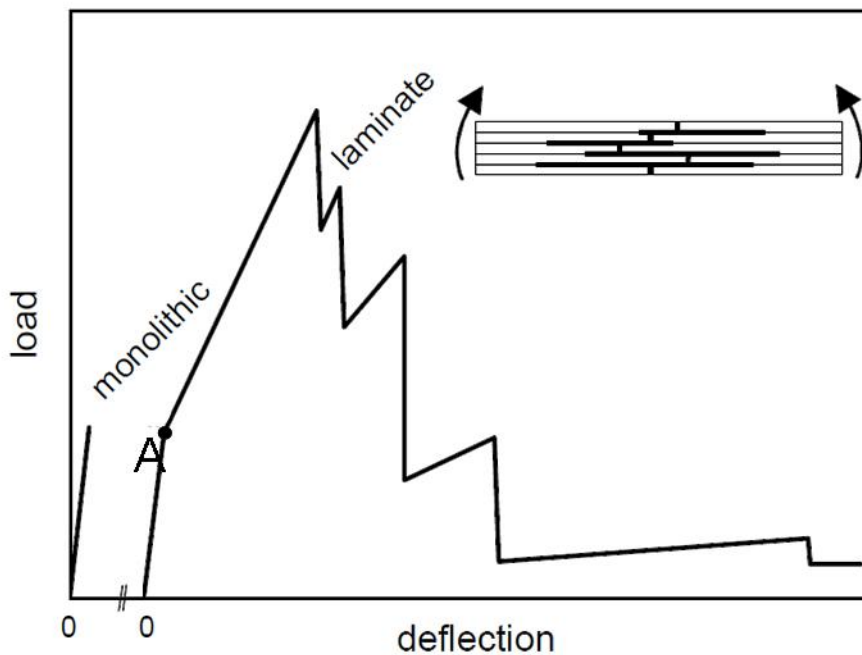


Figure 2.1 - Typical load-deflection diagram of a laminate with weak interfaces

In the case of strong interfaces, where dissimilar materials are joined together by perfectly adherent interface, residual stresses are present after the production process. In such components a predisposed crack coming from a more compliant material into stiffer material will deflect away from the interface

due to the tension induced in the stiffer material. In the case of an appropriate position of materials, when, for example, compliant material is surrounded by strong interfaces, effect of “crack arrest” appears. Strong interfaces hinder the crack propagation, and may prevent failure extending the lifetime of component.

In order to describe the quality of material composites, it is necessary to know the conditions of crack initiation and propagation (see chapter 2.5) as well as to understand the role of other mechanical properties like strength, elastic modulus or thermal expansion coefficients of joined ceramics. The bonding properties of dissimilar materials depend on their chemical and mechanical compatibilities. In reality the bonding region of real bi-materials is characterized by a diffusion zone of finite thickness or by thin layer of reaction products, but for our purpose we will consider a sharp interface between two elastic and ideally bonded materials. This simplification provides a useful tool for description of bond strength and mechanical compatibility. According to Suga et al. [63], the coefficient for the thermally induced stress intensity (K_T) at the interface can be used as a representative parameter to measure the mechanical compatibility of materials with different thermal expansion behaviour. This parameter depends on the elastic properties of the joined materials and is determined as:

$$K_T = \frac{2\Delta\alpha_T\mu_1\mu_2}{\sqrt{(\mu_1 + \mu_2(3 - 4\nu_1))(\mu_2 + \mu_1(3 - 4\nu_2))}} \quad (2.1)$$

Herein $\Delta\alpha_T$ is the difference in coefficients of thermal expansion, μ_n , and ν_n are shear modulus and Poisson ratio of the material n ($n = \overline{1,2}$) correspondingly. The K_T values for engineering materials lie between 0 and 1 MPa/K. Suga et. al. [63] examined a number of composite materials and proposed their classification with regard to their mechanical compatibility into six groups, depending on the values of K_T parameter and the level of anisotropy at the interface. Most ceramic-ceramic combinations possess a low or medium level of anisotropy combined with low values of interfacial thermal stresses. According to the introduced division they fall into group 5 or 6, which are notable for good mechanical compatibility. This feature leads to high values of the interfacial fracture energy and fracture resistance, if a chemical bond is developed with the sufficient chemical compatibility.

In this work we will study weak interfaces between dissimilar ceramics. These materials are often separated by cracking, which would be expected if the toughness of interface is low compared to that of the abutting materials.

2.2 Mechanical behaviour, Dundurs' parameters

In this work a bi-material joint is considered as a combination of two isotropic and elastic materials. For simplicity, we will consider the interface as the horizontal plane and refer to the materials as “above” and “below” the interface. The material above the interface has the shear modulus μ_1 and Poisson's ratio ν_1 , whereas material below the interface is characterized by μ_2 and ν_2 correspondingly.

The elastic behaviour of bi-material interfaces can be described using composite parameters formed from the elastic constants of both materials. Dundurs [21, 22] derived parameters α and β and showed that the stress field of a composite in a state of plane deformations depends only on these two properties.

$$\alpha = \frac{\mu_2(1-\nu_1) - \mu_1(1-\nu_2)}{\mu_2(1-\nu_1) + \mu_1(1-\nu_2)} \quad (2.2)$$

$$\beta = \frac{1}{2} \frac{\mu_2(1-2\nu_1) - \mu_1(1-2\nu_2)}{\mu_2(1-\nu_1) + \mu_1(1-\nu_2)} \quad (2.3)$$

α measures the mismatch in the tensile modulus across the interface and represents the relative stiffness of the two materials. It must lie in the range $-1 < \alpha < 1$ for all possible material combinations. Combinations with $\alpha = 1$ indicate that material 1 is much stiffer than material 2, while $\alpha = -1$ signifies the opposite case. The second parameter β is a measure of mismatch in bulk modulus across the interface. Both parameters vanish for identical materials across the interface. When the indexes of materials 1 and 2 change places, the sign of parameters α and β changes without change of their absolute values.

For Poisson's ratios in the range $0 < \nu < 0.5$, one can see that the physically admissible values of Dundurs' parameters are restricted to the parallelogram: $-1 < \alpha - 4\beta < 1$ and $-1 < \alpha < 1$, which is shown in [Figure 2.2](#).

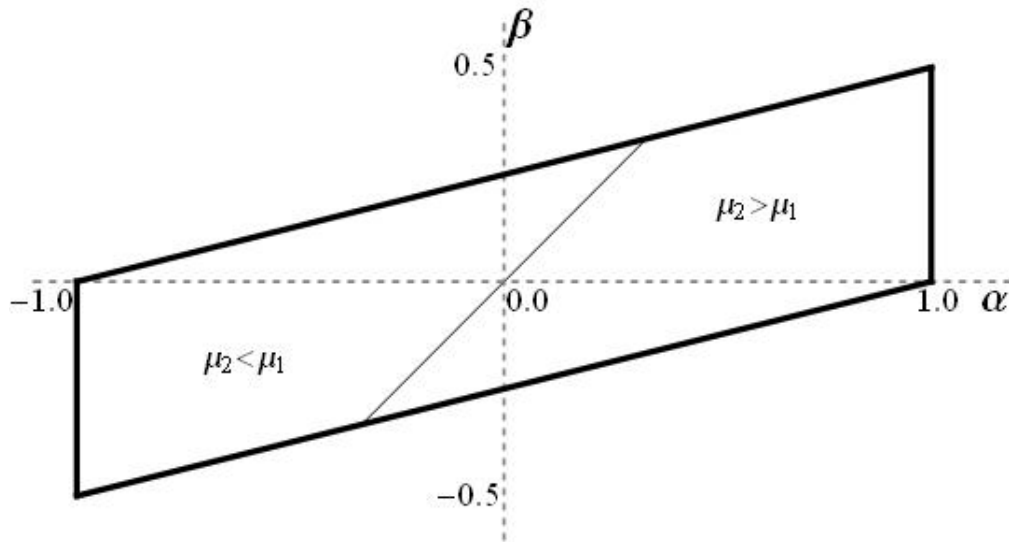


Figure 2.2 - Parallelogram of Dundurs' composite parameters

The $\alpha - \beta$ -plane provides a convenient way to classify material joints with regard to their physical behaviour. The four elastic constants for a pair of materials determine a unique point in the $\alpha - \beta$ -plane. At the same time, one point in this diagram may correspond to a number of material combinations. The origin $\alpha = \beta = 0$ represents the combination of two elastically identical materials. The parallelogram can be divided into two zones by a straight line $\beta = \alpha$, along which the shear modules of joined materials are equal. The zone on the left side of the line contains combinations with $\mu_1 > \mu_2$, while the other corresponds to combinations with $\mu_1 < \mu_2$, respectively.

It was also noticed by Hutchinson [40] that for real existing materials the range of Dundurs' parameters is somewhat more restricted. Most of (α, β) -combinations fall between the lines $\beta = 0$ and $\beta = \alpha/4$ (see [Figure 2.3](#)), whereas α values are distributed over the whole possible region. Here the sign of parameter α is chosen to be always positive by suitably selecting the indexes of joined materials 1 and 2.

2. Fracture mechanics of interfaces

Combinations that satisfy $\beta = 0$ correspond to the case of more simple structure of the interface crack tip fields than those combinations with $\beta \neq 0$ [61]. The plain strain parameter β vanishes, when either two identical materials are joined or both materials are incompressible ($\nu_1 = \nu_2 = 0.5$).

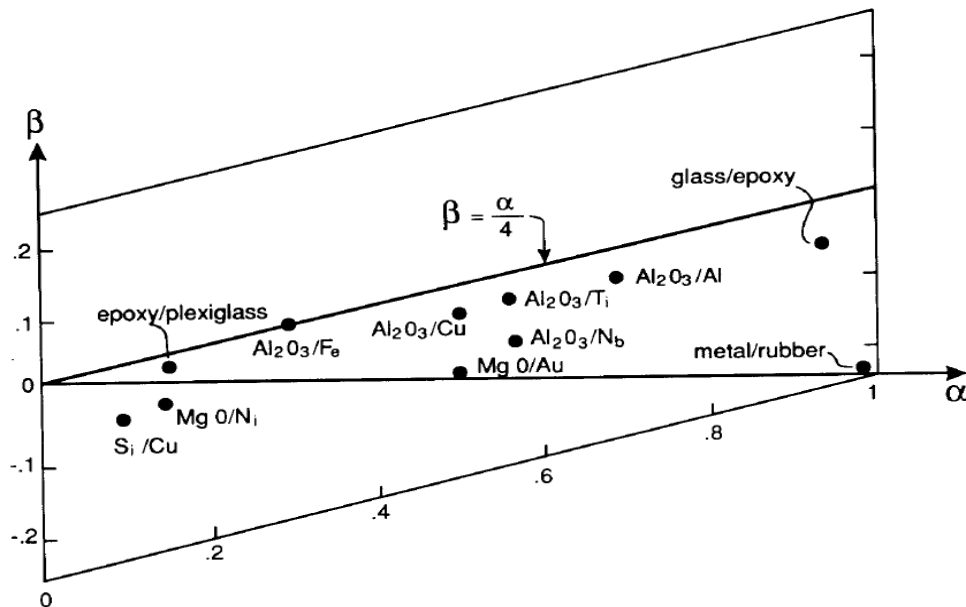


Figure 2.3 - Values of Dundurs' parameters for some typical material combinations [40]

This reduction in the number of elastic constants from four to two simplifies the analysis considerably. The incorporation of the composite parameters into the analysis of elastic bi-material problems leads to more simple description and generalization of the solutions in an interfacial problem.

One more important parameter to determine the stress state at the interface is the so called "oscillatory index", which depends only on second Dundurs' parameter (2.3) and is defined as

$$\varepsilon = \frac{1}{2\pi} \ln \left(\frac{1-\beta}{1+\beta} \right) \quad (2.4)$$

For most ceramic combinations the value of ε is very small, typically of order 0.01 or so. In the case of $\varepsilon = 0$ the stress behaviour at the interface will be similar to the homogeneous case, at the same time a small difference in the

elastic properties of the joined materials causes high stress gradients on the crack faces.

2.3 Interface stress singularities

Williams [71] in 1959 was the first one to carry out the crack tip singularity analysis and for dissimilar media. He showed that the stresses near interface crack tips are proportional to $r^{\Lambda-1}$ and that in general the order of stress singularity is no longer $r^{-1/2}$ like for cracks in homogeneous materials. The asymptotic representation of the interface crack tip stresses σ_{kl} (Figure 2.4) is [42]:

$$\sigma_{kl}(r, \theta) = Kr^{\Lambda-1}g_{kl}(\theta) + O(r^{\Lambda}), \quad k, l = 1, 2, 3 \quad (2.5)$$

where r, θ are polar coordinates defined at the crack tip, $g_{kl}(\theta)$ is an angle function, stress intensity factor K takes into account the influence of applied loading, the geometry of the component and the crack length. The parameter $\Lambda = \Lambda(\alpha, \beta)$ describes the order of singularity.

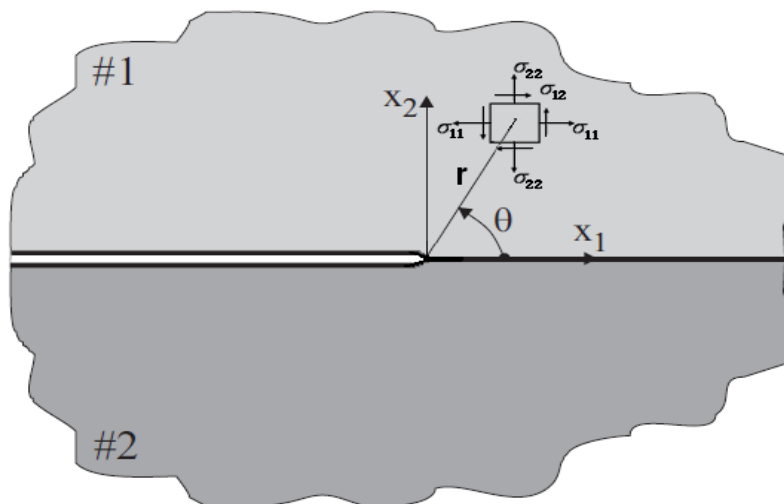


Figure 2.4 - Polar coordinate system at the tip of interface crack

Commonly one of the following three methods is used to calculate the stress singularity order:

2. Fracture mechanics of interfaces

- complex stress functions method, built on a suitably chosen approach (e.g. [18, 19]),
- eigenvalue – eigenfunction method for the Airy function (e.g. [71, 27]),
- Mellin – transformation technique (e.g. [12]).

Below, for the example of the second approach, the algorithm for determination of the stress singularity at the tip of the interfacial crack is shown.

According to the eigenvalue – eigenfunction method, the Airy function A_n has to be determined for each material ($n = 1, 2$):

$$A_n(r, \theta) = r^{\Lambda+1} F_n(\theta, \Lambda), \quad (2.6)$$

where functions $F_n(\theta, \Lambda)$ should correspond to the solution of the differential bipotential equation $\nabla^4 A_n = 0$ and therefore can be written in the form:

$$F_n(\theta, \Lambda) = a_n \sin(\Lambda + 1)\theta + b_n \cos(\Lambda + 1)\theta + c_n \sin(\Lambda - 1)\theta + d_n \cos(\Lambda - 1)\theta, \quad (2.7)$$

The boundary conditions of a traction free crack surface and continuity conditions on the uncracked part of interface form a system of eight equations with eight unknown coefficients a_n, b_n, c_n, d_n ($n = 1, 2$). Due to the homogeneity of equations, a non-trivial solution exists only when the determinant of the coefficient matrix for the system of linear equations vanishes. Thus, the equation $f(\Lambda) = \text{Det}|A| = 0$ gives us the solution for the parameter Λ , which turn out to be the eigenvalues of the system. For the problem of an interface crack lying between two materials, the value order of stress singularity is a complex number, which is found to be $\Lambda = 1/2 + i\varepsilon$ ($i = \sqrt{-1}$ is the imaginary unit). This implies that the stresses change their signs infinitely often in the vicinity of the crack tip and their values are oscillating between the raising asymptote as it is shown on the [Figure 2.5](#).

The oscillatory feature of the elastic field occurs due to the non-zero value of ε . The behaviour of the stresses makes it difficult to obtain a convenient definition of the corresponding fracture parameters in the vicinity of the crack tip and as a result of the oscillation phenomena, it is also difficult to unambiguously

separate the loading into normal and shear components – an opening stress induces shear effects near the crack tip and vice-versa.

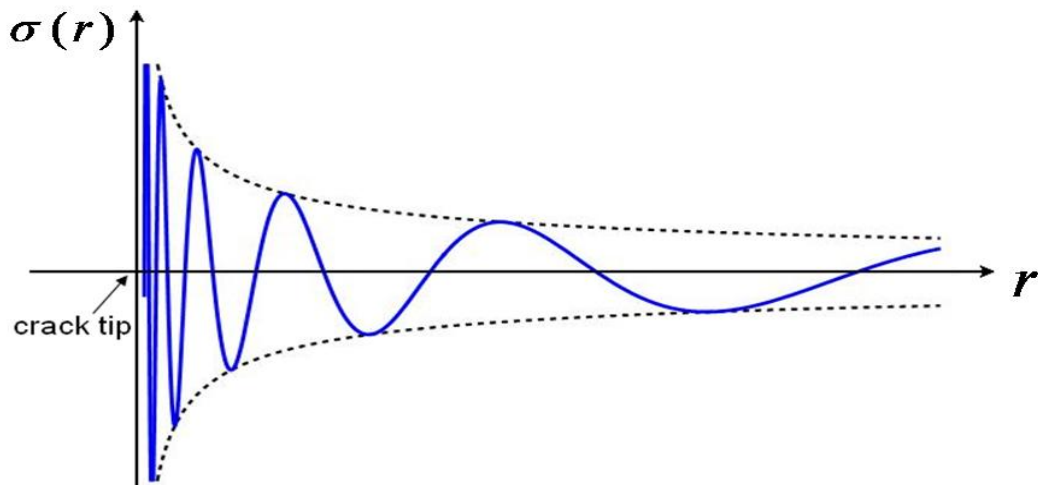


Figure 2.5 - Oscillation behaviour of the stresses in vicinity of interface crack

At the same time the oscillation behaviour of displacements takes place as well. It means that the solution predicts that the crack faces overlap near the crack tip, which is physically impossible. This problem was discussed by number of authors (e.g. [19, 24, 25, 61]). Some special crack tip models (for example, the contact zone model [19] or the interlock model [47]) were proposed. The Comninou contact zone model assumes that the crack is not completely open and its faces are in frictionless contact near the tips. The extent of the contact zone is unknown and must be determined as part of the stress solution. On the other hand, the standard procedure in linear elastic interfacial fracture mechanics is to ignore the overlap between crack faces. It was shown by a number of authors (e.g. [24, 38]) that the size of the oscillation zone is very small compared to the crack length (in the worst theoretical case, which is practically never reached, it is about 10^{-4} of the crack length). Consequently, from physical arguments, it will be acceptable to use a stress solution, which is provided on distance δ from the ends of the crack, where $\delta \geq 1.26 \cdot 10^{-4} a$ and a is a characteristic size of the interface crack.

The way of measuring “stress intensity” is introduced in the chapter 2.4 in order to predict more accurately the stress state at the tip of interface crack, caused by a remote loading or residual stresses.

2.4 Interface fracture mechanical parameters

The mechanical fracture behaviour of interface cracks is of major importance with respect to the strength of the bonded materials. The singular behaviour of the stresses can be uniquely characterized by the complex stress intensity factor (cSIF) $K = K_1 + iK_2$ as [71]:

$$\sigma_{kl}^{(n)}(r, \theta) = \frac{1}{\sqrt{2\pi r}} \left(\operatorname{Re} [Kr^{i\varepsilon}] \sigma_{kl}^{(n)I}(\theta) + \operatorname{Im} [Kr^{i\varepsilon}] \sigma_{kl}^{(n)II}(\theta) \right), \quad (2.8)$$

where $n = 1, 2$ denotes the upper and lower materials, Re and Im are the real and imaginary parts of the quantities in the parentheses, $i = \sqrt{-1}$, expressions $\sigma_{kl}^{(n)I}(\theta)$ and $\sigma_{kl}^{(n)II}(\theta)$ are normalized mode-I and mode-II stresses, which depend upon polar angle θ and elastic material constants.

In the same way, displacements at the interface crack tip are governed by cSIF:

$$U_k^{(n)}(r, \theta) = \sqrt{\frac{r}{2\pi}} \left(\operatorname{Re} [Kr^{i\varepsilon}] U_k^{(n)I}(\theta) + \operatorname{Im} [Kr^{i\varepsilon}] U_k^{(n)II}(\theta) \right), \quad (2.9)$$

where $U_k^{(n)I}(\theta)$ and $U_k^{(n)II}(\theta)$ are normalized mode-I and mode-II displacements.

The combination of tensile (σ_{22}) and shear (σ_{12}) stresses acting along the interface ($\theta = 0$) can be presented by the following expression:

$$\sigma_{22} + i\sigma_{12} = \frac{r^{i\varepsilon}}{\sqrt{2\pi r}} (K_1 + iK_2). \quad (2.10)$$

K_1 and K_2 are analogues of the classical stress intensity factors (K_I , K_{II}), but they no longer represent in-plane tensile and shear modes like in the case of homogeneous material. From the expressions for stresses on the interface near the crack tip (2.10) one can see that even the presence of only tensile stresses leads to the combination of both stress intensity factors K_1 and K_2 :

$$\operatorname{Re}\left[(K_1 + iK_2)r^{i\varepsilon}\right] = \sigma_{22}\sqrt{2\pi r} \quad (2.11)$$

According to Rice [61] a global stress intensity factor ($MPa\sqrt{m}$) may be defined in the usual manner for fixed length of radial distance ahead of the interface crack tip ($r = \tilde{r}$):

$$K_I(\tilde{r}) = K_1 \cos(\varepsilon \ln(\tilde{r})) - K_2 \sin(\varepsilon \ln(\tilde{r})) \quad (2.12)$$

$$K_{II}(\tilde{r}) = K_1 \sin(\varepsilon \ln(\tilde{r})) + K_2 \cos(\varepsilon \ln(\tilde{r})) \quad (2.13)$$

Complex stress intensity factor $K = K_1 + iK_2$ reduces to $K = K_I + iK_{II}$ if the material mismatch is zero ($\varepsilon = 0$), where K_I and K_{II} are stress intensity factors associated with pure mode-I and mode-II loading. At the same time, as every complex number, the cSIF can be rewritten in trigonometric form using Euler's formula:

$$K = K_1 + iK_2 = |K|e^{i\psi}L^{-i\varepsilon}, \quad (2.14)$$

where L is some characteristic length from the crack tip, $|K|$ and ψ are modulus and an argument of a complex number correspondingly, which are determined as:

$$|K| = \sqrt{K_1^2 + K_2^2} \quad (2.15)$$

$$\psi = \tan^{-1}\left(\frac{\operatorname{Im}\left[(K_1 + iK_2)L^{i\varepsilon}\right]}{\operatorname{Re}\left[(K_1 + iK_2)L^{i\varepsilon}\right]}\right) \quad (2.16)$$

Thus, it's necessary to say that there are three main parameters characterizing the stress state near the crack of the crack: an arbitrary characteristic length L , the magnitude of the complex stress intensity factor $|K|$ and the phase angle of the loading ψ . Arbitrary characteristic length is usually taken to be $100\mu m$, and thereby exceeds the size of oscillatory zone. All fracture parameters can be uniquely determined at the distance L from the crack tip. The

values of $|K|$ and ψ are determined by the component's shape and the way of loading. From (2.16) one can see that the value of the loading phase angle also depends on the choice of the characteristic length L . The freedom in the choice of reference length is a consequence of the simple transformation rule [40] from one choice ($L = l_1$) to another ($L = l_2$): $\psi_2 = \psi_1 + \varepsilon \ln(l_2 / l_1)$.

Taking into account equation (2.10), the interface fracture parameters $|K|$ and ψ from (2.14) and (2.16) can be introduced through the stresses acting on the interface in the following manner:

$$|K| = e^{-i\psi} \lim_{r \rightarrow 0} (\sigma_{22} + i\sigma_{12}) \left(\frac{r}{L} \right)^{-i\varepsilon} \sqrt{2\pi r} \quad (2.17)$$

$$\psi = \tan^{-1} \left(\frac{K_2}{K_1} \right) = \tan^{-1} \left(\frac{\sigma_{12}(r=L)}{\sigma_{22}(r=L)} \right) \quad (2.18)$$

The expression (2.18) illustrates that phase angle ψ measures the relative amount of shear stresses to normal stresses acting at the distance L from the crack tip along the interface. Throughout this paper we will call this parameter the mode-mixity parameter.

The asymptotic crack tip field for an interface crack is strikingly different to the corresponding solution for a homogeneous solid. The bi-material crack is always intrinsically under the mixed mode, as a result of elastic mismatch of joined materials, regardless of the nature of the remote loading conditions.

2.5 Fracture resistance of interfaces

Knowledge of the stress state at the tip of the crack is important to describe the behaviour of the crack and to assess whether an interface crack will tend to propagate along the interface or whether it will advance by kinking out of the interface. To understand the fundamental mechanisms responsible for the above mentioned fracture modes the analysis of the interface energy release rate (iERR) has to be carried out.

Subsequently iERR introduces the energy dissipated during the fracture per unit of newly created fracture surface area. The relationship between the iERR

(G_i) and the absolute value of the cSIF ($|K|$) of an interfacial crack is independent of the chosen crack tip model and is given by [48]:

$$G_i = \frac{1}{H_1} |K|^2 \quad \text{or} \quad G_i = \frac{1}{H_1} (K_1^2 + K_2^2) \quad (2.19)$$

where the subscript i represents the interface and G_i has units of energy per area. H_1 depends upon the material properties (E_n – Young's modulus, ν_n – Poisson ratio) of the considered bi-material and has the following form:

$$\frac{1}{H_1} = \frac{(1-\nu_1^2)E_2 + (1-\nu_2^2)E_1}{2E_1E_2 \cosh^2(\pi\varepsilon)}$$

The majority of fracture criteria are focused on the propagation of cracks subjected to opening (mode-I) conditions. But especially along the interfaces, the microstructural fracture phenomena, as it was shown above, tends to be a mixed mode problem. It should be noted that inherently for any interface both stress intensity factors K_1 and K_2 must be prescribed (2.19). To make a conclusion if the interface crack kinks into one of joined materials, interrelations between iERR (G_i) and the toughness of the more compliant material (see chapter 2.5.1) are necessary. In characterizing an interface fracture due to crack propagation, one may prescribe a relation between K_1 and K_2 at fracture, or what is commonly done, introduce the critical energy release rate $G_{i_{cr}}$ (see chapter 2.5.2).

2.5.1 Crack kinking out of the interface

In this chapter an analysis of a crack kinking out of an interface is performed. The analysed crack tip geometry is shown in [Figure 2.6](#). The main interfacial crack lies between two different elastic materials. A straight crack segment of the length a_k kinks downwards into the lower material under the angle ω_k (if upper material 1 is much stiffer than lower material 2). The length a_k is assumed to be small compared to the length of the interfacial crack itself. The stress field prior to kinking is a singular field (as discussed in chapter 2.3), which

2. Fracture mechanics of interfaces

is described by cSIF $K = K_I + iK_{II}$. Since the tip of the kinked crack is surrounded by the homogeneous material 2, the stress state can be uniquely described by conventional mode-I and mode-II stress intensity factors, K_I and K_{II} of material 2:

$$\sigma_{22'} + i\sigma_{12'} = \frac{1}{\sqrt{2\pi x_1'}} (K_I + iK_{II}), \quad (2.20)$$

where $x_1'x_2'$ is the coordinate system with origin at the tip of the kinked crack.

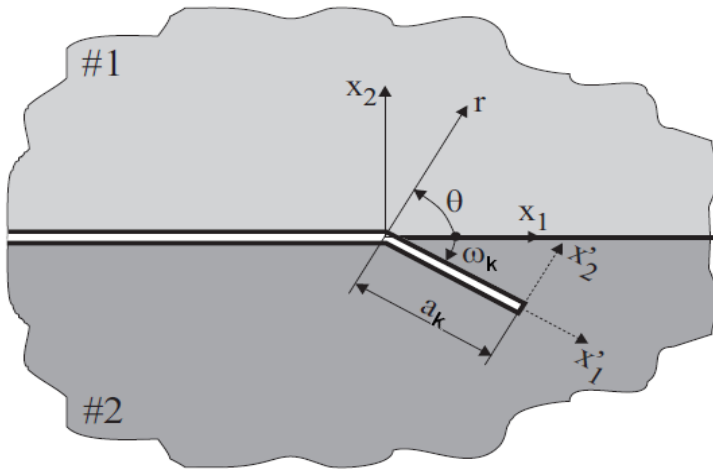


Figure 2.6 - Geometry at the tip of a kinked crack

The relationship between the intensity factors of a kinked crack and the prescribed complex interface intensity K obtained by He and Hutchinson [35] and Cotterell and Rice [20] can be written as:

$$K_I + iK_{II} = c(\omega_k, \alpha, \beta) K a_k^{i\varepsilon} + \bar{d}(\omega_k, \alpha, \beta) \bar{K} a_k^{-i\varepsilon}, \quad (2.21)$$

where $(\bar{\quad})$ denotes complex conjugation, functions $c(\omega_k, \alpha, \beta)$ and $d(\omega_k, \alpha, \beta)$ are complex-valued functions of kinking angle ω_k and Dundurs parameters α and β .

According to the relationship (2.21), the ratio of the energy release rates for a kinked crack (G_k) and an interfacial crack (G_i) can be found as:

$$\frac{G_k}{G_i} = \left(\frac{1+\alpha}{1-\beta^2} \right) \left(|c|^2 + |d|^2 + 2 \operatorname{Re} [cde^{2i\tilde{\psi}}] \right), \quad (2.22)$$

where $\tilde{\psi} = \psi + \varepsilon \ln \left(\frac{a_k}{L} \right)$ is used as a measure of the loading combination.

Tabulated values for $c = c_R + ic_I$ and $d = d_R + id_I$ are given by [33].

The ratio (2.22) is an important factor to predict the behaviour of an interface crack. To explain its role, the graphs which show the dependence of the kinked angle ω_k on the ratio of energy release rates G_k / G_i , are built for two different material joints in [Figure 2.7](#) (Fig. 2.7a – material joint with both Dundurs' parameters equal zero, Fig. 2.7b – Alumina-Zirconia ceramic joint with $\alpha = 0.209$ and $\beta = 0.015$). The choice of these two material combinations can be explained by the fact that the first joint corresponds to the homogeneous ceramic material, while the second $Al_2O_3 - ZrO_2$ joint was selected as a typical engineering bi-material, which occurs e.g. in Lambda-sensor designs.

Each line in [Figure 2.7](#) corresponds to different loading combinations, the lowest one ($\psi = 0$) represents pure mode-I, other lines represent mixed-modes with different relative amount of mode-II to mode-I (parameter ψ varies from 0 to $\pi/2$). Eventually the pure mode-II stress state at the interface is reached for $\psi = \pi/2$. It was noted in [35] that the ratio of toughness (2.22) strongly depends on α , while the effect of the second Dundurs' parameter β appears to be weak, especially in the range of $|\beta| < 0.1$.

For each material combination the dashed line shows the minimum value of ratio G_k / G_i which is needed to ensure crack kinking out of interface for any applied loading conditions. One can see that for a joint of two identical materials this value becomes 1.8. At the same time for a combination of Alumina-Zirconia materials, the toughness of Zirconia has to be twice greater than the interface energy release rate to keep the crack staying at the interface for any loading combination ψ . In the case of a pure mode-I stress state at the tip of the interfacial crack for both considered bi-materials, the crack will propagate along the interface without kinking when the simple for understanding condition $G_i < G_k$ ($G_k / G_i > 1$) takes place.

2. Fracture mechanics of interfaces

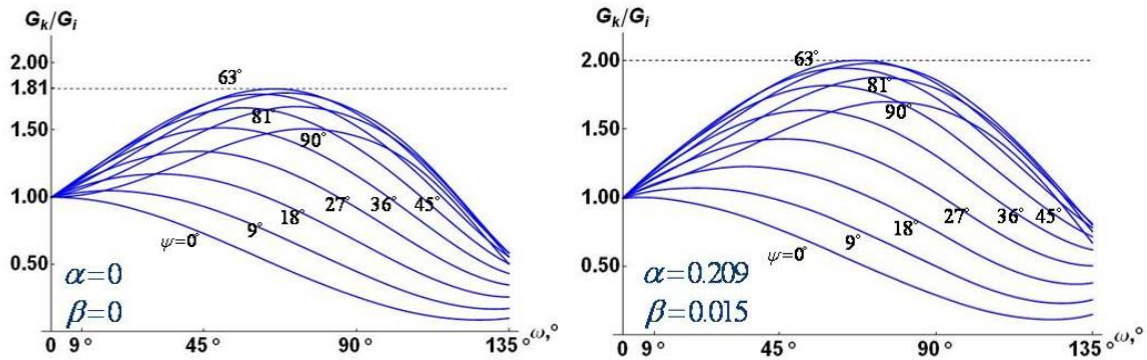


Figure 2.7 - Variations of G_k/G_i with kink angle ω_k for range of loading combinations: a) joint of identical materials; b) $ZrO_2(Mg-PSZ) / Al_2O_3$ (por. 0.1%)

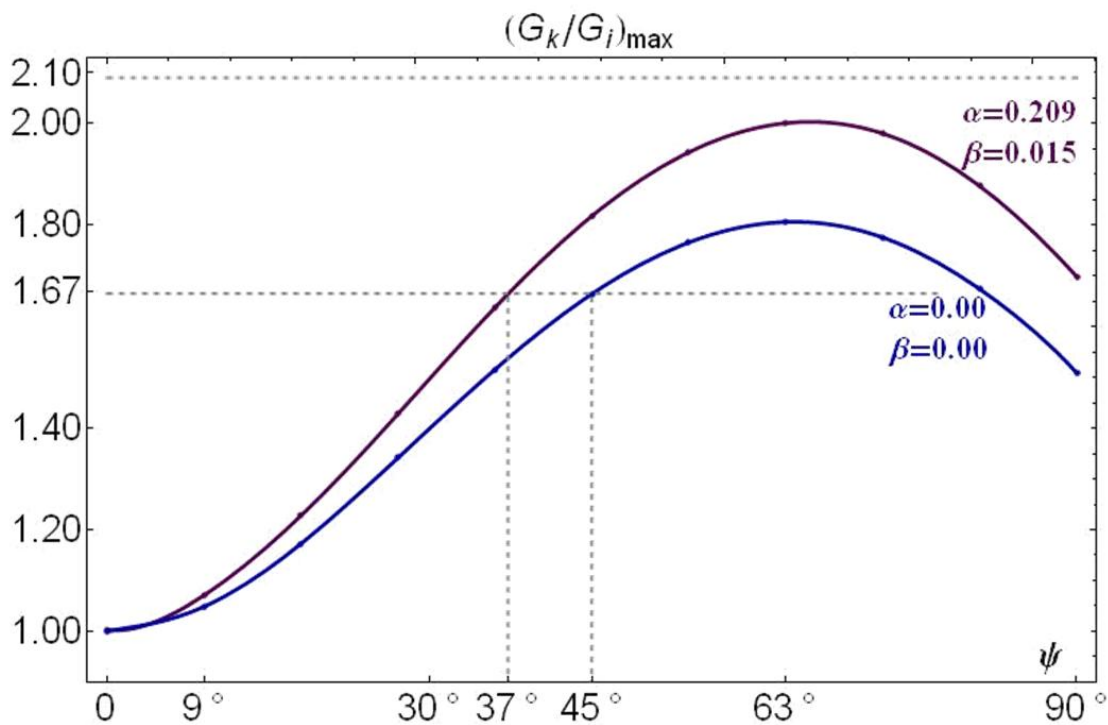


Figure 2.8 - The minimum value of the toughness ratio to ensure crack kinking for different loading combinations ψ

It should be noted that in the case of mode-mixity stress state, the ratio depends on the bi-material properties as well. Thus, the following conclusions can be made: if G_k is sufficiently large compared to iERR (G_i) the crack will never kink into the compliant material. However if G_k is comparable to G_i there

will still be a loading range of $0 \leq \psi \leq \psi_{\max}$, such that the crack stays in the interface, while for other loading combinations $\psi > \psi_{\max}$ the crack kinking will take place. Figure 2.8 displays the dependence of ψ_{\max} on the toughness ratio G_k / G_i and allows to illustrate the arguments from above. The lines show for each material the minimum value of the ratio (2.22) needed to ensure that the interfacial crack will not leave the interface. If the ratio of the toughness G_k / G_i is 2.1, the dashed line is above both material curves means that kinking will never occur for bi-material 1 ($\alpha = 0.0$, $\beta = 0.0$) and also for bi-material 2 ($\alpha = 0.209$, $\beta = 0.015$). In case that of G_k / G_i equals 1.67, the dashed line crosses the material curves and the points of intersection give us the values of ψ_{\max} . For bi-material 1 until $\psi < \psi_{\max} = 45^\circ$ crack will stay at interface. When the equal bi-action of shear and tensile stresses is achieved ($\psi = 45^\circ$) the crack will kink into the compliant component of the joint under the angle $\omega_k = 57^\circ$. But in the case of bi-material 2 the range of mode-mixed stress states to keep the crack at interface is somewhat narrower and crack kinking will occur for $\psi \geq \psi_{\max} = 37^\circ$.

In summary, the condition for crack kinking from the interface into one of the joined materials depends on the combination of the toughness of the joined materials and the interface as well as of the loading conditions. From here on, we assume that the crack stays on the interface to facilitate the reliability analysis of interfaces.

2.5.2 Crack propagation along the interface

According to the energy release rate approach (based on Griffith's criterion [30]) failure occurs when the iERR reaches a critical value G_{icr} , the fracture energy or toughness of the interface. Thus, the following behaviours can be distinguished:

$$\begin{aligned}
 G_i < G_{icr} & \text{ - no crack growth,} \\
 G_i = G_{icr} & \text{ - the crack will begin to propagate,} \\
 G_i > G_{icr} & \text{ - the crack propagates and failure occurs;}
 \end{aligned}
 \tag{2.23}$$

2. Fracture mechanics of interfaces

In the case of a homogeneous material, the energy, which is needed to create a unit fracture surface, is a parameter that depends only on the material. For interfaces in bi-material joints, it will be shown below that the interface toughness G_{icr} is not a pure material property but it depends strongly on the mode-mixity parameter ψ . According to expression (2.19), G_{icr} can be rewritten as:

$$G_{icr} = \frac{1}{H_1} (K_{1cr}^2 + K_{2cr}^2) = \frac{K_{1cr}^2}{H_1} \left(1 + \frac{K_{2cr}^2}{K_{1cr}^2} \right).$$

Using (2.18) and designating ratio K_{1cr}^2 / H_1 as G_I , where G_I is the pure mode-I toughness, the critical energy release rate can be explicitly denoted as:

$$G_{icr} = G_I (1 + \tan^2 \psi) \quad (2.24)$$

It should be noted, that G_{icr} is associated only with cSIF K_1 and depends on K_2 only through the phase angle ψ .

Criterion (2.24) is similar to the empirical expressions presented by Hutchinson and Suo [40], who suggested two functions to describe the critical iERR:

$$G_{icr}(\psi) = G_I (1 + \tan^2 [(1 - \gamma)\psi]) \quad (2.25)$$

$$G_{icr}(\psi) = G_I (1 + (1 - \gamma) \tan^2 \psi), \quad (2.26)$$

which coincide with equation (2.24) for $\gamma = 0$ (γ is a parameter, which adjusts the sensibility to mode-II contribution in the criterion).

Another alternative formulation of the energy release criterion, where the roughness of interface is taking into account, was presented by Charalambides in [16]. There, it is assumed that fracture is caused by a mode-I energy release rate G_0 , which is presented from two sides as:

$$G_0 = G_I + \sin^2 \varpi G_{II}, \quad (2.27)$$

$$G_0 = G_{icr} \left[\cos^2(\Psi - \Psi_0) + \sin^2 \varpi \sin^2(\Psi - \Psi_0) \right], \quad (2.28)$$

with ϖ representing the surface roughness slope. In order to employ this criterion, three experimental observations are required to determine G_0 , ϖ and the bi-material phase shift Ψ_0 . For a bi-material pair of ceramic materials, the roughness slope ϖ may be taken to be zero. Then from (2.27) and (2.28) we can obtain an expression:

$$G_{icr} = G_I \left[1 + \tan^2(\Psi - \Psi_0) \right], \quad (2.29)$$

which can be compared to (2.24). They are essentially the same except the phase shift Ψ_0 , the third free parameter. It was noted [5] that the effect of this parameter is similar to the effect of choosing another value for the reference length L in (2.16).

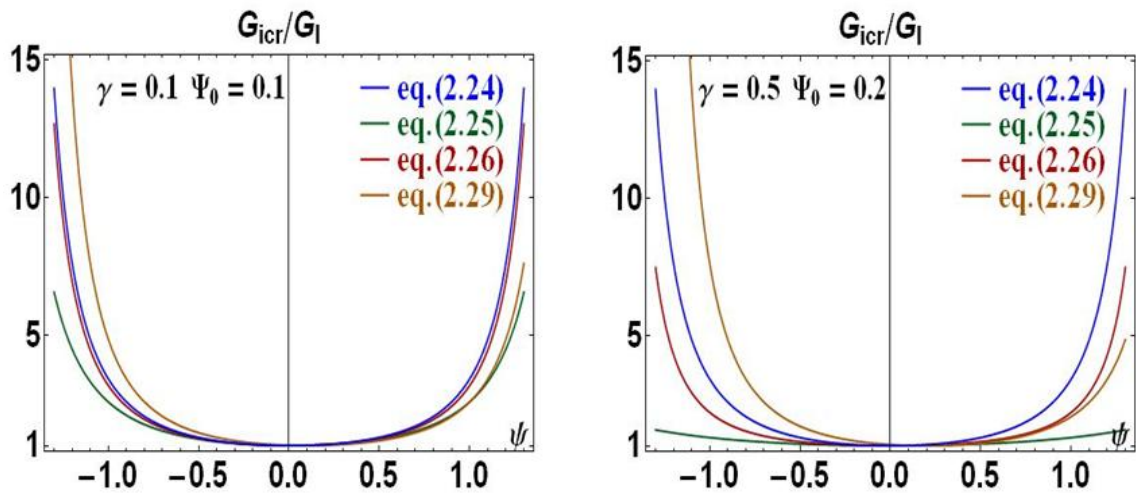


Figure 2.9 - Comparison of fracture criteria for different values of free parameters

For comparison of the above-mentioned fracture criteria [Figure 2.9](#) is presented. The four fracture energy release criteria differ by parameters γ and Ψ_0 , which have been chosen to fit experimental data. The total fracture energy of interfacial cracks is found to increase as mode-II loading increases, especially for

2. Fracture mechanics of interfaces

brittle interfaces. Also it can be noted that at some interval near $\psi = 0$ (mode-I stress state) all the criteria are essentially the same, nevertheless they differ with increasing of mode-mixity parameter, what means they differently describe the impact of stress mode-II.

In this work, it is expected that the failure will occur for interface cracks under mode-mixed loading conditions, where normal stresses predominate over the shear stresses ($|\psi| < 0.5$). Thus, without losing in accuracy the energy release rate fracture criteria based on equation (2.24) for interface toughness will be used.

3. Statistical aspects of failure

The natural flaws, such as pores, inclusions, imperfect grain boundaries or surface machining defects, occur in components due to the fabrication procedure or further processing. The failure of ceramic components is often caused by an unstable propagation of cracks originated from such natural imperfections. The reliability of brittle materials is generally assessed using the Weibull theory [70], which is based on a weakest-link approach (see chapter 3.1). Following the idea of probabilistic methods, the distribution of material strength is presented as a function of the defects size distribution with its fracture mechanics extensions. Models for the failure probability determination for homogeneous brittle materials are based on a number of assumptions, e.g. that stresses can be considered constant along the crack faces [74, 36]. In the case of bi-material ceramic joints the stress field depends on the material combination and changes significantly along the faces of interface flaws or cracks. This means that the classical Weibull failure theory needs to be modified in order to describe the role of cracks at interfaces properly.

3.1 Basic ideas of the weakest-link approach

The weakest-link model is used to determine the reliability of bi-material ceramic components subjected to the multiaxial stress state. According to this approach, the most dangerous natural flaw is the one, which has the most unfavourable combination of size, location and orientation in the stress field. To predict the failure of the component in the frame of a statistical model, the following assumptions are made [74]:

- a) The material contains a number of defects of different size, which can be described as cracks with fracture mechanics methods,

3. Statistical aspects of failure

- b) the size of the defect is a random variable, which is described by a certain distribution function,
- c) there are no interactions between the natural flaws, i.e. failure of a crack is not affected by the presence of other cracks,
- d) failure of the worst natural flaw (i.e. where the combination between high stress and large size is most unfavourable) causes the failure of the whole component,
- e) location and orientation of the natural flaws are random.

Thus, failure occurs in a stress field if the size a of natural flaw exceeds some critical value a_{cr} . The critical crack size depends on the location $\vec{x} = (x, y, z)$ and orientation $\omega = (\omega, \varphi)$ of the crack in the existing stress field (see Figure 3.1). The failure probability of the component, which contains exactly one flaw of random size, location and orientation can be written as:

$$Q_1 = \int_V f_V(\vec{x}) dV \cdot \int_{\Omega} f_{\Omega}(\omega) d\Omega \cdot \int_{a_{cr}(x,\omega)}^{\infty} f_a(a) da \quad (3.1)$$

where $f_V(\vec{x})$, $f_{\Omega}(\omega)$ and $f_a(a)$ are probability density functions (PDF) of the location, orientation and the random flaw size a , respectively.

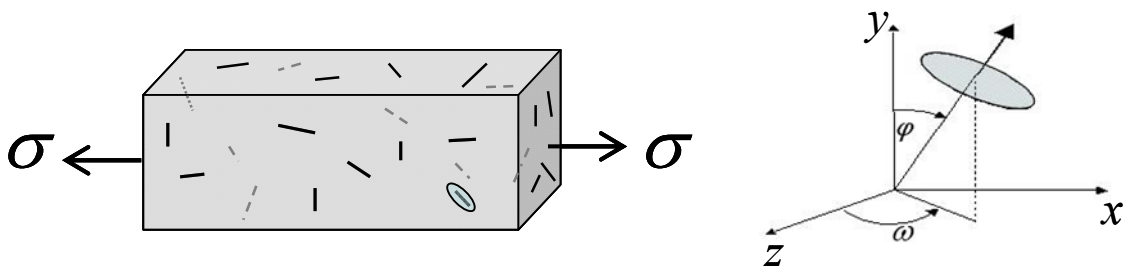


Figure 3.1 - Locations and orientations of natural flaws in stress field

For homogeneous isotropic materials the distribution of the flaws locations and orientations are uniform distributions over the volume V and all possible orientations Ω (which in three-dimensional space is 4π), with following PDFs $f_V(\vec{x})$ and $f_{\Omega}(\omega)$:

$$f_V(\bar{x}) = \frac{1}{V}, \quad (3.2)$$

$$f_\Omega(\omega) = \frac{1}{4\pi}. \quad (3.3)$$

The probability that a flaw exceeds the critical value $a_{cr}(x, \omega)$ is given by:

$$P_a = P(a > a_{cr}) = \int_{a_{cr}(x, \omega)}^{\infty} f_a(a) da, \quad (3.4)$$

Where the PDF $f_a(a)$ of the flaw size is generally modelled corresponding to the Pareto distribution [31, 74]:

$$\int_{a_{cr}(x, \omega)}^{\infty} f_a(a) = 1 - F_a(a) = \left(\frac{a_0}{a}\right)^{r-1}, \quad (3.5)$$

where $a_0 \leq a$ is the minimum possible flaw size considered and ensures normalization of the PDF.

Taking the probability density functions (3.2), (3.3) and (3.5) into account, the failure probability of a homogeneous isotropic component with one natural flaw is given by:

$$Q_1 = \frac{1}{V} \int_V \frac{1}{4\pi} \int_{\Omega} (1 - F_a(a_{cr})) d\Omega dV \quad (3.6)$$

The corresponding survival probability for a component with only one natural flaw is $P_S^{(1)} = 1 - Q_1$. According to the assumption c), the survival probability for a component with n natural defects can be presented as the simultaneous survival probability of n different components (see [Figure 3.2](#)), each of them exhibiting only one natural flaw: $P_S^{(n)} = (1 - Q_1)^n$.

3. Statistical aspects of failure

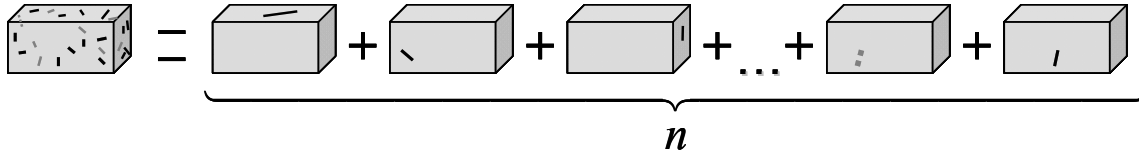


Figure 3.2 – Schematic illustrating the probability of independent events: one component with n flaws can be represented by n components with one flaw.

The actual number of the natural flaws in a specific component is a random quantity. For statistically independent infinitesimal volume elements, dV , the number of flaws, n , contained can be described by a Poisson distribution, what is in good agreement with empirical data. Correspondingly the probability (P_n) of having exactly n flaws in the volume V of a component is [14, 36]:

$$P_n = \frac{M^n e^{-M}}{n!}, \quad (3.7)$$

where M is the average number of flaws in such components.

Now, the survival probability of a component containing an arbitrary number of flaws can be given by the product of the probabilities P_n and $P_S^{(n)}$ and the sum over all possible numbers of flaws:

$$\begin{aligned} P_S &= \sum_{n=0}^{\infty} P_n \cdot P_S^{(n)} = \sum_{n=0}^{\infty} \frac{M^n e^{-M}}{n!} \cdot (1 - Q_1)^n = \\ &= e^{-M} \sum_{n=0}^{\infty} \frac{[M(1 - Q_1)]^n}{n!} = \left\{ e^h = \sum_{k=0}^{\infty} \frac{h^k}{k!} \right\} = e^{-M} e^{M(1 - Q_1)} = e^{-MQ_1} \end{aligned} \quad (3.8)$$

Finally the expression for the failure probability of a component with an arbitrary number of natural flaws is obtained as:

$$P_F = 1 - \exp(-M \cdot Q_1) \quad (3.9)$$

or in full form inserting equation (3.6):

$$P_F = 1 - \exp \left(-M \frac{1}{V} \int_V \frac{1}{4\pi} \int_{\Omega} \left(\frac{a_0}{a_{cr}(\vec{x}, \omega)} \right)^{r-1} d\Omega dV \right) \quad (3.10)$$

One can see that the failure probability of the component, caused by unstable propagation of the natural flaws, is a function of the critical crack size of the most dangerous flaw in the applied stress field. A similar equation can be formulated if failure is induced by surface flaws. The worst flaw in the component determines the effective permissible load for a prescribed failure probability. The dependence of the critical flaw size on the local stress field has to be derived from an appropriate fracture mechanics model [9].

3.2 Weibull theory for brittle homogeneous materials

For homogeneous components subjected to mixed-mode loading, fracture occurs when the equivalent mode-I stress intensity factor (K_{Ieq}) exceeds the fracture toughness (K_{Ic}) of the material. $K_{Ieq}(K_I, K_{II}, K_{III}) = \sigma_{eq} \sqrt{a} Y_I$ is a function of the mode I-III stress intensity factors, and depends on the multiaxial stress field as well as on the fracture mechanics geometry factor Y_I , accounting for the crack shape, the specimens geometry and the geometry of the applied loading.

According to the failure criterion $K_{Ieq} \geq K_{Ic}$ the following expression for the critical crack size a_{cr} is obtained:

$$a_{cr}(\vec{x}, \omega) = \left(\frac{K_{Ic}}{\sigma_{eq}(\vec{x}, \omega) \cdot Y_I} \right)^2 \quad (3.11)$$

This representation is only valid if $\sigma_{eq}(\vec{x}, \omega)$ is considered to be constant along the crack size a or if only small stress gradients exist. Different functional criteria for determination equivalent stresses can be introduced in order to described the sensitivity of material to mixed-mode loading.

The failure probability (3.10), rewritten in terms of stresses, using (3.11), has the following form:

3. Statistical aspects of failure

$$P_F = 1 - \exp \left(- \frac{1}{V_0} \int_V \frac{1}{4\pi} \int_{\Omega} \left(\frac{\sigma_{eq}(\vec{x}, \omega)}{\sigma_0} \right)^m d\Omega dV \right), \quad (3.12)$$

where $m = 2(r-1)$ characterizes the scatter of the strength distribution, V_0 is the unit volume containing an average number of M_0 flaws and σ_0 is a characteristic strength value:

$$\sigma_0 = \frac{K_{Ic}}{Y_I \sqrt{a_0} M_0^{1/m}} \quad (3.13)$$

Introducing a reference stress σ^* , which characterizes the load level, the expression for failure probability can be brought to the form of a Weibull distribution [14, 36, 39, 62, 74]:

$$P_F = 1 - \exp \left[- \left(\frac{\sigma}{b} \right)^m \right] \quad (3.14)$$

with the two Weibull parameters m and b reflecting the distribution of flaws in the material. First, m is a dimensionless number corresponding to the variability in the measured strength, while the Weibull parameter b has the dimension of stress. Parameter b depends on the material parameters m and σ_0 , the volume of the component and the load level, described by σ^* :

$$b = \sigma_0 \left[\frac{1}{2\pi A_0} \int_A \int_{\Omega} \left(\frac{\sigma_{eq}(\vec{x}, \omega)}{\sigma^*} \right)^m dA d\Omega \right]^{-1/m} \quad (3.15)$$

According to (3.15) we can introduce the relation between b and σ_0 in the form: $\sigma_0 = b \cdot H_V$, with the normalized stress integral $H_V = [V_{eff}/V_0]^{1/m}$, where

$$V_{eff} = \int_V \frac{1}{4\pi} \int_{\Omega} \left(\frac{\sigma_{eq}(\vec{x}, \omega)}{\sigma^*} \right)^m d\Omega dV, \quad (3.16)$$

is an effective volume integral or so called stress integral. This parameter describes the dependence of the Weibull parameter b on the component's geometry, while the parameter σ_0 relates only to material properties. It means that for the same material, but different geometry configurations of the component, we will have the following general relations:

$$\sigma_0 = b_1 \cdot H_{V1} = b_2 \cdot H_{V2} = b_3 \cdot H_{V3} = \text{const} \quad (3.17)$$

where H_{Vj} have to be evaluated separately for each component. Equation (3.17) is an important basis for failure probability calculations and the assessment of size effects.

3.3 Numerical integration

For determining the failure probability, a numerical integration over the entire volume of a component and different flaw orientations becomes necessary (see eq. (3.12)) due to the possible complexity of the component's geometry and the stress representation. The main principle of postprocessor STAU (German acronym for Statistische Auswertung \equiv statistical analysis) used for this purpose is discussed in chapter 3.3.1. This program was initially developed as a numerical integration scheme for the calculation of failure probability and it is based on the Gaussian integration method (see chapter 3.3.2).

3.3.1 Finite element postprocessor STAU

STAU is a weakest-link finite element (FE) postprocessor tool, which provides the integration routine required for equation (3.12). The input for STAU are the results of a FE-analysis, containing the solution of the stress distribution over the volume of a component. The schematic process of a failure probability analysis with STAU is shown in [Figure 3.3](#). Material properties and the component's geometry as well as the applied loading and boundary conditions determine the stress distribution, which is the basis for the prediction of the failure probability.

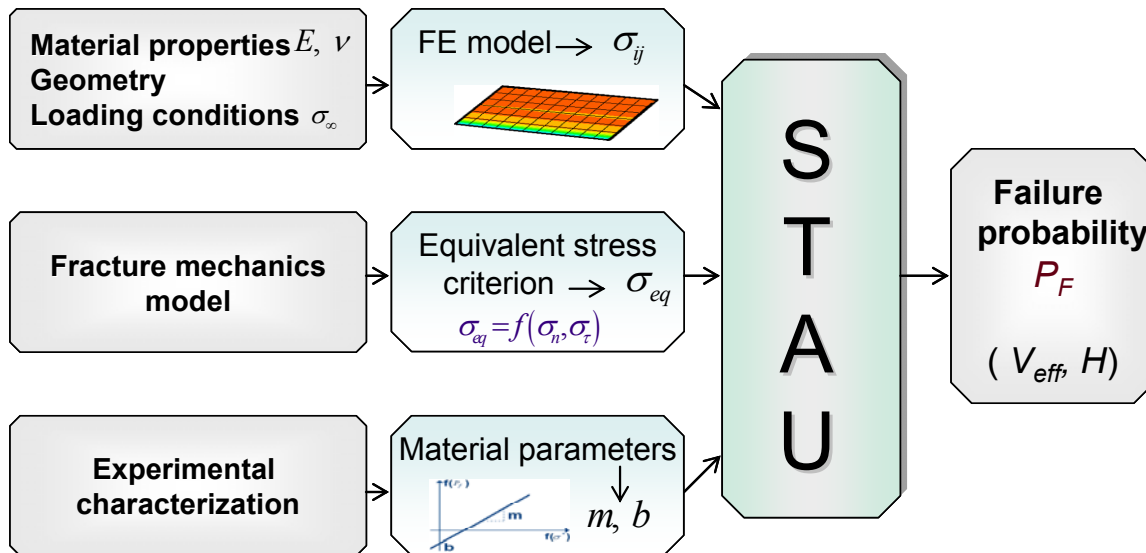


Figure 3.3 – Failure probability analysis using STAU

The geometry of the component is realized in STAU as a set of nodes and elements of a FE-mesh. The stress state of the component is given by the stress values in the nodes of the FE-model. The material parameters m and σ_0 need to be specified by the user as well as appropriate equivalent stress criteria. For the integration process STAU introduces additional integration points (Gaussian collocation points), in which interpolated stress functions are calculated. This procedure leads to an enhanced numerical accuracy.

Compared to other similar tools, STAU is a unique program due to a number of possibilities. One can solve the problems associated with spontaneous fracture, sub-critical crack propagation under transient loading, or thermo-mechanical problems, including thermal shock and contact loading [62].

3.3.2 Gaussian integration method

In a numerical analysis according to Gaussian quadrature rule, the definite integral of a function is usually approximated by a weighted sum of function values at specified points within the domain of integration, which is conventionally taken as $[-1, 1]$:

$$\int_{-1}^1 f(x)dx \approx \sum_{n=1}^N h x_n f(x_n), \quad (3.18)$$

3.3 Numerical integration

here N -point Gaussian quadrature rule yields an exact result for polynomials of degree $2N-1$ or less by a suitable choice of the collocation points x_n and weight coefficients hx_n ($n = \overline{1, N}$).

An integral over an arbitrary interval $[a, b]$ must be mapped into an integral over $[-1, 1]$ before applying the Gaussian quadrature rule. The corresponding numerical solution can be obtained in the form:

$$\int_a^b f(x)dx \approx \frac{b-a}{2} \sum_{n=1}^N hx_n f\left(\frac{b-a}{2}x_n + \frac{b+a}{2}\right) \quad (3.19)$$

The collocation points x_n are determined as the roots of the Legendre polynomials L_N [2] and the respective weight functions are given by:

$$hx_n = \frac{2}{(1-x_n^2)[L'_N(x_n)]^2} \quad (3.20)$$

Now the integrals in expression (3.12) can be rewritten by taking into account that the stress values ($\sigma_{eq,k}$) are given in N_{FE} -number of elements of corresponding the FE-model:

$$\begin{aligned} \frac{1}{4\pi V_0} \int_V \int_{\Omega} \left(\frac{\sigma_{eq}(\bar{x}, \omega)}{\sigma_0} \right)^m d\Omega dV &= \frac{1}{4\pi V_0} \sum_{k=1}^{N_{FE}} \int_{V_k} \int_{\Omega} \left(\frac{\sigma_{eq,k}(\bar{x}, \omega)}{\sigma_0} \right)^m d\Omega dV_k = \\ &= \frac{1}{4\pi V_0} \sum_{k=1}^{N_{FE}} \int_x \int_y \int_z \int_0^{2\pi} \int_0^{2\pi} \left(\frac{\sigma_{eq,k}(\bar{x}, \omega, \varphi)}{\sigma_0} \right)^m d\omega d\varphi dz dy dx = \\ &= \frac{1}{4\pi V_0} \sum_{k=1}^{N_{FE}} \int_{-1}^1 \int_{-1}^1 \int_{-1}^1 \int_{-1}^1 \left(\frac{\sigma_{eq,k}(\tilde{x}, \tilde{y}, \tilde{z}, \tilde{\omega}, \tilde{\varphi})}{\sigma_0} \right)^m J_V J_{\Omega} d\tilde{\varphi} d\tilde{\omega} d\tilde{z} d\tilde{y} d\tilde{x} = \\ &= \frac{1}{4\pi V_0} \sum_{k=1}^{N_{FE}} \sum_{\alpha=1}^{N_{\alpha}} hx_{\alpha} \sum_{\gamma=1}^{N_{\gamma}} hy_{\gamma} \sum_{\xi=1}^{N_{\xi}} hz_{\xi} \sum_{\varpi=1}^{N_{\varpi}} h\omega_{\varpi} \sum_{\phi=1}^{N_{\phi}} h\varphi_{\phi} \left(\frac{\sigma_{eq,k}(\tilde{x}_{\alpha}, \tilde{y}_{\gamma}, \tilde{z}_{\xi}, \tilde{\omega}_{\varpi}, \tilde{\varphi}_{\phi})}{\sigma_0} \right)^m J_V J_{\Omega} \end{aligned} \quad (3.21)$$

where J_V , J_{Ω} are Jacobian matrices, which describe the change of the integration intervals according to (3.19), \tilde{x}_{α} , \tilde{y}_{γ} , \tilde{z}_{ξ} , $\tilde{\omega}_{\varpi}$ and $\tilde{\varphi}_{\phi}$ are Gaussian collocation points with their respective weights hx_{α} , hy_{γ} , hz_{ξ} , $h\omega_{\varpi}$ and $h\varphi_{\phi}$.

3.4 Generalization for the case of interface flaws

Equation (3.12) represents the failure probability of homogeneous components. In our research, due to the presence of interfaces, the assumptions of the classical Weibull theory have to be adapted for the case of interface failure. The statements that there are no interactions between natural flaws and that all of them could have arbitrary location and orientation with a random distribution of the defect size are still relevant. But in this special case the focus will only be on the natural flaws lying at the interface A_i , the location of natural defects is described by $\vec{x} = (x, z)$ and their orientation by single angle ω (see [Figure 3.4](#)). Also ordinary Weibull theory considers stresses to be constant over the crack faces, where the relation between stress state and critical flaw length is given by (3.11). This assumption is not valid any longer in the case of bi-material joints, where the stress field at the interface depends on the material combination and changes significantly near the tips of interface cracks.

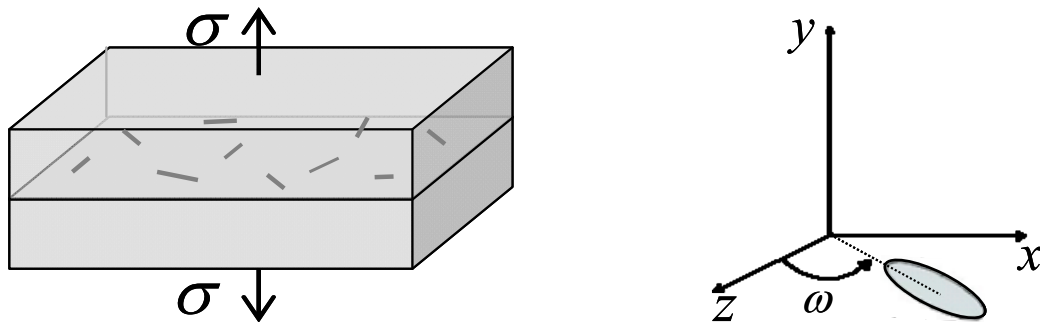


Figure 3.4 - Locations and orientations of interface natural flaws in a stress field

As mentioned above, the stress state at the interface can be uniquely described by the cSIF $K = K_1 + iK_2$. Most methods require a separate calculation of SIFs for each given stress distribution and each crack length. A weight function approach for bi-material joints, as proposed by L. Banks-Sills [4], simplifies this procedure and SIFs for specified geometry can be found with the help of two arbitrary reference solutions ($K^{(k)}$, $K^{(m)}$) through the weight functions $\vec{h}_i = (h_{ix}, h_{iy})$ for bi-material components ($i = \overline{1, 2}$):

$$\begin{aligned}
 K_1 &= \int_{S_T} \left(h_{1x}(s, a) \cdot \sigma(s) + h_{1y}(s, a) \tau(s) \right) ds \\
 K_2 &= \int_{S_T} \left(h_{2x}(s, a) \sigma(s) + h_{2y}(s, a) \tau(s) \right) ds
 \end{aligned} \tag{3.22}$$

where S_T is a boundary with applied arbitrary tractions $\vec{T} = (\sigma, \tau)$ and expressions for the weight functions are given by:

$$\begin{aligned}
 \vec{h}_1 &= \frac{H_1}{2\Sigma^2} \left(K_2^{(k)} \frac{\partial \vec{U}^{(m)}}{\partial a} - K_2^{(m)} \frac{\partial \vec{U}^{(k)}}{\partial a} \right) \\
 \vec{h}_2 &= \frac{H_1}{2\Sigma^2} \left(K_1^{(m)} \frac{\partial \vec{U}^{(k)}}{\partial a} - K_1^{(k)} \frac{\partial \vec{U}^{(m)}}{\partial a} \right) \\
 \Sigma^2 &= K_1^{(m)} K_2^{(k)} - K_2^{(m)} K_1^{(k)} \neq 0,
 \end{aligned} \tag{3.23}$$

Where the stress intensity factors $K_i^{(k)}$, $K_i^{(m)}$ and the displacement fields $\vec{U}^{(k)}$, $\vec{U}^{(m)}$ are known for two reference loading systems, denoted by k and m , applied to the same cracked body.

The failure state for the same bi-material component can be reached for different values of principal stresses depending also on their combination. Therefore, introduction of equivalent stresses is needed. Implying the equivalent stress (σ_{eq}) as the mode-I stress, which produces the same interface energy release rate as the given mixed mode stresses, the equivalent cSIF can be written as $|K_{eq}|^2 = K_{1eq}^2 + K_{2eq}^2 = \sigma_{eq}^2 Y_x^2$, where Y_x is a combination of the weight functions \vec{h}_i and describes the remote loading conditions.

Combining (2.19) and (2.24), we obtain the following equation for the critical crack length (a_{cr}) at the interface fracture of the bi-material:

$$\frac{\sigma_{eq}^2}{H_1} [Y_x(a_{cr})]^2 = G_{1cr} (1 + \tan^2 \psi) \tag{3.24}$$

While in most cases this equation can be solved only numerically for a_{cr} due to the complicated form of the correction factor Y_x , an analytical solution can

3. Statistical aspects of failure

be given for the special case of an infinite bi-material joint with internal interfacial crack. This particular case is useful, because it corresponds to the case of natural flaws lying at the interface, whose size a is infinitesimally small compared to the component's dimensions.

Stress intensity factors for this type of crack geometry were provided by various authors (e.g. [4, 17, 41, 61]) and they read:

$$K_1 + iK_2 = (1 + 2i\varepsilon)(\sigma_{22} + i\sigma_{12})\sqrt{\frac{\pi a}{2}}(a)^{-i\varepsilon} \quad (3.25)$$

or through the far-field equivalent stresses:

$$K_{1eq} + iK_{2eq} = (1 + 2i\varepsilon)\sigma_{eq}\sqrt{\frac{\pi a}{2}}(a)^{-i\varepsilon}. \quad (3.26)$$

Now, separating real and imaginary parts, the stress intensity factors K_{1eq} and K_{2eq} can be obtained to calculate iERR according to (2.19):

$$\begin{aligned} K_{eq} &= K_{1eq} + iK_{2eq} = \sqrt{\frac{\pi a}{2}}\sigma_{eq}(1 + 2i\varepsilon)(\cos[\varepsilon \ln(a)] - i\sin[\varepsilon \ln(a)]) = \\ &= \sqrt{\frac{\pi a}{2}}\sigma_{eq}\{(\cos[\varepsilon \ln(a)] + 2\varepsilon \sin[\varepsilon \ln(a)]) - i(\sin[\varepsilon \ln(a)] - 2\varepsilon \cos[\varepsilon \ln(a)])\} \end{aligned}$$

Consequently,

$$K_{1eq} = (\operatorname{Re}[K_{eq}]) = \sqrt{\frac{\pi a}{2}}\sigma_{eq}(\cos[\varepsilon \ln(a)] + 2\varepsilon \sin[\varepsilon \ln(a)]) \quad (3.27)$$

$$K_{2eq} = (\operatorname{Im}[K_{eq}]) = \sqrt{\frac{\pi a}{2}}\sigma_{eq}(2\varepsilon \cos[\varepsilon \ln(a)] - \sin[\varepsilon \ln(a)]) \quad (3.28)$$

Thus, the modulus of the equivalent complex stress intensity factor $|K_{eq}|$ according to (2.15) is:

$$\begin{aligned}
 |K_{eq}|^2 &= \left(\operatorname{Re}[K_{eq}] \right)^2 + \left(\operatorname{Im}[K_{eq}] \right)^2 = \frac{\pi a}{2} \sigma_{eq}^2 \left\{ \left(\cos[\varepsilon \ln(a)] + 2\varepsilon \sin[\varepsilon \ln(a)] \right)^2 + \right. \\
 &\quad \left. + \left(2\varepsilon \cos[\varepsilon \ln(a)] - \sin[\varepsilon \ln(a)] \right)^2 \right\} = \frac{\pi a}{2} \sigma_{eq}^2 \left(\cos^2[\varepsilon \ln(a)] + \right. \\
 &\quad \left. + 4\varepsilon \cos[\varepsilon \ln(a)] \sin[\varepsilon \ln(a)] + 4\varepsilon^2 \sin^2[\varepsilon \ln(a)] + 4\varepsilon^2 \cos^2[\varepsilon \ln(a)] - \right. \\
 &\quad \left. - 4\varepsilon \cos[\varepsilon \ln(a)] \sin[\varepsilon \ln(a)] + \sin^2[\varepsilon \ln(a)] \right) = \\
 &= \frac{\pi a}{2} \sigma_{eq}^2 (1 + 4\varepsilon^2)
 \end{aligned} \tag{3.29}$$

Therefore expressions (3.24) and (3.29) yield to a linear equation with respect to the critical crack length and the solution is given by:

$$a_{cr} = \frac{G_{1cr} H_1 (1 + \tan^2 \psi)}{\sigma_{eq}^2 Y_i^2}, \tag{3.30}$$

where $Y_i = \sqrt{\pi(1+4\varepsilon^2)}/2$ is a real constant for the given specified material combination.

The interface failure probability following (3.10) rewritten in terms of stresses becomes:

$$P_F = 1 - \exp \left(- \frac{1}{A_0} \int_{A_i} \frac{1}{2\pi} \int_{\Omega} \left(\frac{\sigma_{eq}(\bar{x}, \omega)}{\sigma_0 \sqrt{1 + \tan^2 \psi}} \right)^m d\Omega dA_i \right), \tag{3.31}$$

where the integration is performed over the whole interface plane A_i . A_0 is a unit area containing an average number of M_0 flaws. In the form of a Weibull distribution (3.14) for interface failure the Weibull parameter b for the bi-material joint is:

$$b = \sigma_0 \left[\frac{1}{2\pi A_0} \int_{A_i} \int_{\Omega} \left(\frac{\sigma_{eq}(\bar{x}, \omega)}{\sigma^* \sqrt{1 + \tan^2 \psi}} \right)^m dA_i d\Omega \right]^{-1/m} \quad \sigma_0 = \frac{\sqrt{G_{1cr} H_1}}{Y_i \sqrt{a_0} M_0^{1/m}} \tag{3.32}$$

The integration over Ω takes the orientation dependence of the equivalent stresses due to the non-symmetrical shape of the in-plane crack into account.

In the next chapter the comparison of the failure probability expressions for the case of a homogeneous brittle component (3.12) and the case of interface failure in a ceramic bi-material (3.31) is provided.

3.5 Discussion of results

As it was mentioned [15, 62], ordinary Weibull theory for homogeneous materials has some limitations. First, it is built on a similar fracture mechanical model ($K_{Icr} = \sigma_{eq} \sqrt{a_{cr}} Y$), while in the general case of bi-material, as it was shown in (3.24), the relation between the critical interface flaw size and the equivalent stress cannot be written in terms of simple power law ($G_{icr} = \sigma_{eq} \sqrt{a_{cr}} Y(a_{cr})$). However, for both – cracks in homogeneous material and interfacial cracks – once the critical crack size is known as a function of equivalent stresses in the volume or over the interface plane, the failure probability formulation in terms of stresses can be determined directly, as it is exemplified for the infinite bi-material joint with an one-dimensional crack model. The second important limitation of classical Weibull theory is the fact that unstable crack propagation in homogeneous material is described through the fracture toughness, which is a material constant. For a bi-material this is not the case any more and the interface toughness becomes a function of the applied loading combination, determined by (2.24).

This difference becomes evident when comparing the obtained results for the interface failure probability (3.31), (3.32) with the ordinary Weibull theory for brittle fracture of homogeneous ceramics (3.12), (3.13) and (3.15). The failure probability relation for bi-material case mainly corresponds to that of the homogeneous case, except the $\tan^2 \psi$ -term in the denominator of the geometry-dependent strength parameter b . This term appears, namely due to the fact that the interface toughness is not a pure material constant, but a function of mode-mixity at the tip of the crack. This leads to a dependence of the interface failure probability on the way of the applied loading.

Similar to (3.21), the integrals in expression (3.31) with given stress values $\sigma_{eq,k}$ from the corresponding FE-model and the calculated values of mode-mixity

parameters (ψ_k) at the tips of potential cracks (in each FE-node) are the following:

$$\begin{aligned}
 & \frac{1}{2\pi A_0} \iint_{A \Omega} \left(\frac{\sigma_{eq}(\bar{x}, \omega)}{\sigma_0 \sqrt{1 + \tan^2 \psi}} \right)^m d\Omega dA = \frac{1}{2\pi A_0} \sum_{k=1}^{N_{FE}} \int_{A_k} \int_0^{2\pi} \left(\frac{\sigma_{eq,k}(\bar{x}, \omega)}{\sigma_0 \sqrt{1 + \tan^2 \psi(\bar{x}, \omega)}} \right)^m d\omega dA_k = \\
 & = \frac{1}{2\pi A_0} \sum_{k=1}^{N_{FE}} \int_{-1}^1 \int_{-1}^1 \int_{-1}^1 \left(\frac{\sigma_{eq,k}(\tilde{x}, \tilde{z}, \tilde{\omega})}{\sigma_0 \sqrt{1 + \tan^2 \psi_k(\tilde{x}, \tilde{z}, \tilde{\omega})}} \right)^m J_A J_\Omega d\tilde{\omega} d\tilde{z} d\tilde{x} = \\
 & = \frac{1}{2\pi A_0} \sum_{k=1}^{N_{FE}} \sum_{\alpha=1}^{N_\alpha} h x_\alpha \sum_{\xi=1}^{N_\xi} h z_\xi \sum_{\varpi=1}^{N_\varpi} h \omega_\varpi \left(\frac{\sigma_{eq,k}(\tilde{x}_\alpha, \tilde{z}_\xi, \tilde{\omega}_\varpi)}{\sigma_0 \sqrt{1 + \tan^2 \psi_k(\tilde{x}_\alpha, \tilde{z}_\xi, \tilde{\omega}_\varpi)}} \right)^m J_A J_\Omega \quad (3.33)
 \end{aligned}$$

where J_A , J_Ω are Jacobian matrices, which describe the change of the integration intervals according to (3.19), \tilde{x}_α , \tilde{z}_ξ and $\tilde{\omega}_\varpi$ are Gaussian collocation points with their corresponding weights $h x_\alpha$, $h z_\xi$, and $h \omega_\varpi$, which are calculated from (3.20).

The main task of the next chapter will be to consider the impact of the $\tan^2 \psi$ -term on the failure probability prediction. For this purpose, an auxiliary problem of a bi-material strip with internal interfacial crack under remote stress field is considered.

4. Mechanical problem of a bi-material strip

The plane elasticity problem for a bi-material strip of infinite length is considered (Figure 4.1). The origin of a Cartesian coordinate system (x_1, x_2) is located at the centre of a crack. It is assumed that the upper material (E_1, ν_1) , occupying $0 < x_2 < h_1$, is perfectly bonded to the lower material (E_2, ν_2) , occupying $-h_2 < x_2 < 0$, everywhere on the interface $x_2 = 0$ except along the crack faces $-a < x_1 < a$.

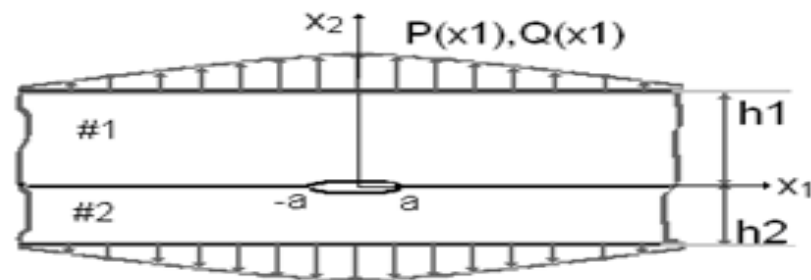


Figure 4.1 - Bi-material strip with an interface crack at $x_2 = 0$, remote loading by tensile $P(x_1)$ and shear $Q(x_1)$ stresses.

The considered bi-material strip is loaded on the upper ($x_2 = h_1$) and lower ($x_2 = -h_2$) borders by tensile and shear loading. Our task is to find the stress state at the interface of the bi-material strip. To be more precise, the value of mode-mixity parameter ψ is of special interest; which measures the ratio of shear and normal stresses at the tip of the crack and depends on the loading conditions and the geometry of the strip.

4.1 Mathematical statement of the problem

The remote loading, presented by tensile $P(x_1)$ and shear $Q(x_1)$ stresses, is applied on the upper and lower surface of the component. Thus, the boundary conditions in terms of stresses are the following:

$$\sigma_{12}^{(1)}(x_1, h_1) = Q(x_1) \quad \sigma_{12}^{(2)}(x_1, -h_2) = Q(x_1) \quad (4.1)$$

$$\sigma_{22}^{(1)}(x_1, h_1) = P(x_1) \quad \sigma_{22}^{(2)}(x_1, -h_2) = -P(x_1) \quad (4.2)$$

Along the un-cracked part of the interface, the following continuity conditions for the stress components and displacements are imposed:

$$\left. \begin{aligned} \sigma_{k2}^{(1)}(x_1, 0) &= \sigma_{k2}^{(2)}(x_1, 0) \\ U_k^{(1)}(x_1, 0) &= U_k^{(2)}(x_1, 0) \end{aligned} \right\}, \quad \text{where } a \leq |x_1| < \infty \quad k = \overline{1, 2} \quad (4.3)$$

and the conditions, which describe that the crack surfaces are free of loading, are:

$$\sigma_{k2}^{(1)}(x_1, 0) = \sigma_{k2}^{(2)}(x_1, 0) = 0, \quad \text{where } |x_1| \leq a \quad k = \overline{1, 2} \quad (4.4)$$

Assuming a state of plane strain, the relations between stresses ($\sigma_{kj}^{(n)}$) and displacements ($U_k^{(n)}$) in each material can be described by Hooke's law:

$$\sigma_{kj}^{(n)} = \lambda_n \left(\frac{\partial U_1^{(n)}}{\partial x_1} + \frac{\partial U_2^{(n)}}{\partial x_2} \right) \delta_{kj} + \mu_n \left(\frac{\partial U_k^{(n)}}{\partial x_j} + \frac{\partial U_j^{(n)}}{\partial x_k} \right) \quad (4.5)$$

where index (n) indicates the number of material; λ_n , μ_n ($n = 1, 2$) are elastic Lamé constants, which are defined through the given material properties as:

$$\lambda_n = \frac{E_n \nu_n}{(1 + \nu_n)(1 - 2\nu_n)}, \quad \mu_n = \frac{E_n \nu_n}{2(1 + \nu_n)}.$$

The system of equations of equilibrium for the considered materials, in terms of displacements, has the following form:

$$\begin{cases} (\lambda_n + 2\mu_n) \frac{\partial^2 U_1^{(n)}}{\partial x_1^2} + \mu_n \frac{\partial^2 U_1^{(n)}}{\partial x_2^2} + (\lambda_n + \mu_n) \frac{\partial^2 U_2^{(n)}}{\partial x_1 \partial x_2} = 0 \\ (\lambda_n + 2\mu_n) \frac{\partial^2 U_2^{(n)}}{\partial x_2^2} + \mu_n \frac{\partial^2 U_2^{(n)}}{\partial x_1^2} + (\lambda_n + \mu_n) \frac{\partial^2 U_1^{(n)}}{\partial x_1 \partial x_2} = 0 \end{cases} \quad (4.6)$$

Thus, the mathematical statement of the considered plane problem of a bi-material strip with internal interface crack is given by the system of four differential equations (4.6) under the above stated boundary (4.1), (4.2) and interfacial (4.3), (4.4) conditions.

4.2 Solution procedure

The problem formulated in the previous chapter can be represented as a superposition of two sub problems (Figure 4.2), for which solutions can be obtained in analytical or half-analytical way by means of solving singular integral equations (SIE). Problem (a) – an un-cracked bi-material strip of infinite length, where normal and shear stresses are applied on the boundaries: this sub problem represents itself a problem of theory of elasticity and allows to vary the boundary conditions and geometry of the strip. Problem (b) – an infinite bi-material joint with an interface crack of finite length, where no remote loading is applied – represents the fracture mechanical part [51].

The stress state at the interface for the originally compound problem ($\sigma^{(com)}$) is then given as a sum of the solutions for problems (a) and (b), respectively:

$$\sigma_{kj}^{(com)}(x_1, 0) = \sigma_{kj}^{(a)}(x_1, 0) + \sigma_{kj}^{(b)}(x_1, 0) \quad (4.7)$$

4. Mechanical problem of a bi-material strip

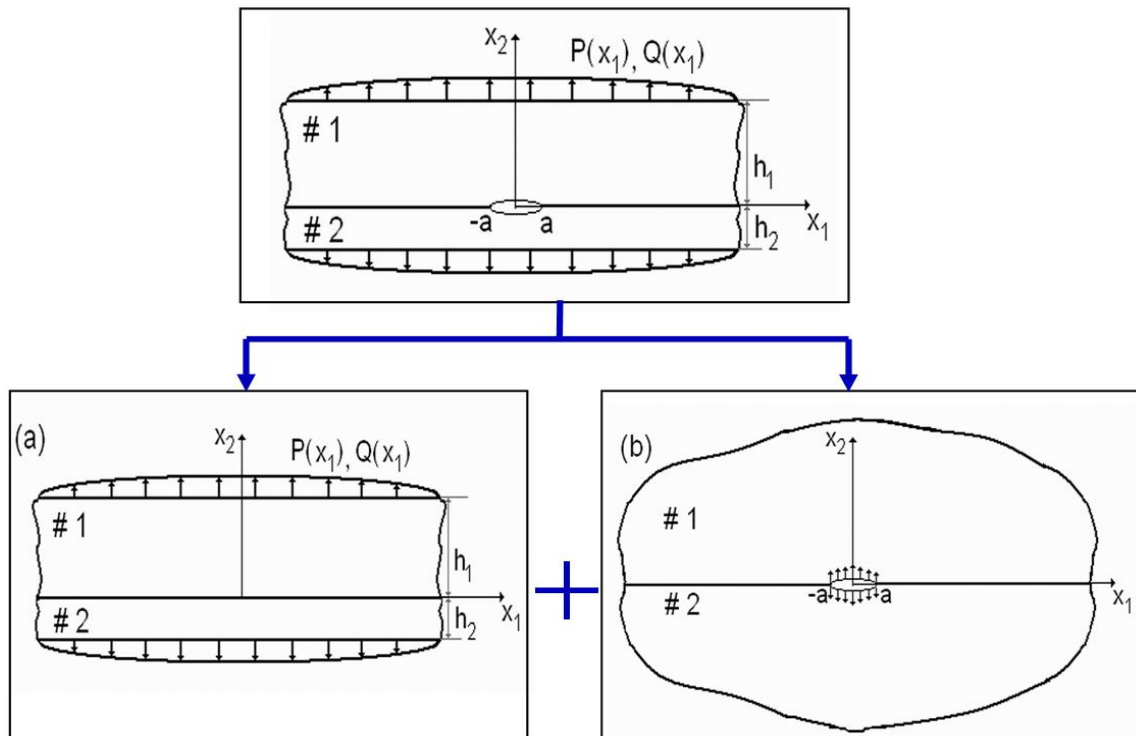


Figure 4.2 - Superposition for a bi-material strip with an internal crack

4.2.1 Crack-free bi-material strip of infinite length

The mathematical statement of the problem (a) is presented by the equilibrium equation (4.6) with the boundary conditions (4.1), (4.2) and following stress and displacement continuity conditions at the interface:

$$\left. \begin{aligned} \sigma_{kj}^{(1)}(x_1, 0) &= \sigma_{kj}^{(2)}(x_1, 0) \\ U_k^{(1)}(x_1, 0) &= U_k^{(2)}(x_1, 0) \end{aligned} \right\}, \quad \text{where } -\infty < x_1 < \infty \quad (4.8)$$

4.2.1.1 Derivation of singular integral equations

Because of symmetry it is sufficient to consider the elastic strip problem for $0 < x_1 < \infty$ only. We introduce six unknown functions $g_1, g_2, g_3, g_4, f_1, f_2$ representing the stresses and displacements for a specific choice of the strip geometry in the following way, similar to [29, 44]:

4.2 Solution procedure

$$\begin{aligned}
 g_1(x_1) &= \sigma_{12}^{(1)}(x_1, h_1), & g_2(x_1) &= U_2^{(1)}(x_1, h_1) \\
 f_1(x_1) &= \sigma_{12}^{(1)}(x_1, 0) = \sigma_{12}^{(2)}(x_1, 0) & f_2(x_1) &= U_2^{(1)}(x_1, 0) = U_2^{(2)}(x_1, 0) \\
 g_3(x_1) &= \sigma_{12}^{(2)}(x_1, -h_2), & g_4(x_1) &= U_2^{(2)}(x_1, -h_2)
 \end{aligned} \tag{4.9}$$

In order to solve the differential equation (4.6) we apply the finite Fourier transforms on x_2 -direction. They allow us to reduce the number of independent variables in the partial differential equations [67]. Thereby, for the upper material we obtain:

$$\begin{aligned}
 \bar{U}_1^{(1)}(x_1, p) &= \int_0^{h_1} U_1^{(1)}(x_1, x_2) \cos(\eta_1 p x_2) dx_2 \\
 \bar{U}_2^{(1)}(x_1, p) &= \int_0^{h_1} U_2^{(1)}(x_1, x_2) \sin(\eta_1 p x_2) dx_2
 \end{aligned} \tag{4.10}$$

where $\eta_1 = \frac{\pi}{h_1}$ and the symbol $(\bar{\quad})$ indicates the Fourier transforms. In this case functions $\bar{U}_1^{(1)}(x_1, p)$ and $\bar{U}_2^{(1)}(x_1, p)$ are governed by the system of ordinary differential equations:

$$\begin{cases}
 (\lambda_1 + 2\mu_1) \frac{d^2 \bar{U}_1^{(1)}}{dx_1^2} + (\lambda_1 + \mu_1) \eta_1 p \frac{d \bar{U}_2^{(1)}}{dx_1} - \mu_1 \eta_1^2 p^2 \bar{U}_1^{(1)} = -(-1)^p g_1 + f_1 - \lambda_1 (-1)^p g_2' + \lambda_1 f_2' \\
 \mu_1 \frac{d^2 \bar{U}_2^{(1)}}{dx_1^2} - (\lambda_1 + \mu_1) \eta_1 p \frac{d \bar{U}_1^{(1)}}{dx_1} - (\lambda_1 + 2\mu_1) \eta_1^2 p^2 \bar{U}_2^{(1)} = (\lambda_1 + 2\mu_1) \eta_1 p ((-1)^p g_2 - f_2)
 \end{cases}$$

Introducing additional infinite Fourier transforms with respect to the x_1 -coordinate

$$\begin{aligned}
 \bar{\bar{U}}_1^{(1)}(t, p) &= \int_0^{\infty} \bar{U}_1^{(1)}(x_1, p) \sin(tx_1) dx_1 \\
 \bar{\bar{U}}_2^{(1)}(t, p) &= \int_0^{\infty} \bar{U}_2^{(1)}(x_1, p) \cos(tx_1) dx_1
 \end{aligned} \tag{4.11}$$

4. Mechanical problem of a bi-material strip

to the previous system of equations, we will arrive at the following algebraic system of linear equations concerning the second transforms of displacements:

$\bar{\bar{U}}_1^{(1)}(t, p)$ and $\bar{\bar{U}}_2^{(1)}(t, p)$:

$$\begin{cases} ((\lambda_1 + 2\mu_1)t^2 + \mu_1\eta_1^2 p^2)\bar{\bar{U}}_1^{(1)} + (\lambda_1 + \mu_1)\eta_1 p t \bar{\bar{U}}_2^{(1)} = (-1)^p \bar{g}_1 - \bar{f}_1 + \lambda_1 (-1)^p \bar{g}'_2 - \lambda_1 \bar{f}'_2 \\ (\lambda_1 + \mu_1)\eta_1 p t \bar{\bar{U}}_1^{(1)} + ((\lambda_1 + 2\mu_1)\eta_1^2 p^2 + \mu_1 t^2)\bar{\bar{U}}_2^{(1)} = \frac{1}{t}(\lambda_1 + 2\mu_1)\eta_1 p ((-1)^p \bar{g}'_2 - \bar{f}'_2) \end{cases} \quad (4.12)$$

where

$$\begin{aligned} \bar{g}_1(t) &= \int_0^\infty g_1(x_1) \sin(tx_1) dx_1, & \bar{f}_1(t) &= \int_0^\infty f_1(x_1) \sin(tx_1) dx_1, \\ \bar{g}'_2(t) &= \int_0^\infty g'_2(x_1) \sin(tx_1) dx_1, & \bar{f}'_2(t) &= \int_0^\infty f'_2(x_1) \sin(tx_1) dx_1, \end{aligned}$$

symbol ()' indicates total derivative, t, p – are Fourier variables.

Thus, the system of differential equations (4.6) was reduced to an algebraic system of linear equations with respect to integral transforms of variables. The solution of the system (4.12) and both inverse transforms will lead to the following expressions for displacements in the upper material through the unknown functions g_1, g'_2, f_1, f'_2 :

$$\begin{aligned} \frac{\partial u_1^{(1)}}{\partial x_1}(x_1, x_2) &= \int_0^\infty g_1(\tau) A_1^{(1)}(x_1, x_2, \tau) d\tau + \int_0^\infty g'_2(\tau) B_1^{(1)}(x_1, x_2, \tau) d\tau + \\ &+ \int_0^\infty f_1(\tau) C_1^{(1)}(x_1, x_2, \tau) d\tau + \int_0^\infty f'_2(\tau) D_1^{(1)}(x_1, x_2, \tau) d\tau, \end{aligned} \quad (4.13)$$

and

$$\frac{\partial u_2^{(1)}}{\partial x_2}(x_1, x_2) = \int_0^\infty g_1(\tau) A_2^{(1)}(x_1, x_2, \tau) d\tau + \int_0^\infty g'_2(\tau) B_2^{(1)}(x_1, x_2, \tau) d\tau +$$

$$+ \int_0^{\infty} f_1(\tau) C_2^{(1)}(x_1, x_2, \tau) d\tau + \int_0^{\infty} f_2'(\tau) D_2^{(1)}(x_1, x_2, \tau) d\tau, \quad (4.14)$$

where functions $A_k^{(1)}(x_1, x_2, \tau)$, $B_k^{(1)}(x_1, x_2, \tau)$, $C_k^{(1)}(x_1, x_2, \tau)$ and $D_k^{(1)}(x_1, x_2, \tau)$ are determined and introduced in Appendix A.

The normal stress component can be found according to Hooke's law (4.5), therefore:

$$\begin{aligned} \sigma_{22}^{(1)}(x_1, x_2) = & \int_0^{\infty} g_1(\tau) A_3^{(1)}(x_1, x_2, \tau) d\tau + \int_0^{\infty} g_2'(\tau) B_3^{(1)}(x_1, x_2, \tau) d\tau + \\ & + \int_0^{\infty} f_1(\tau) C_3^{(1)}(x_1, x_2, \tau) d\tau + \int_0^{\infty} f_2'(\tau) D_3^{(1)}(x_1, x_2, \tau) d\tau, \end{aligned} \quad (4.15)$$

where the functions $A_3^{(1)}$ to $D_3^{(1)}$ are known functions of material properties and geometry parameters and can be obtained subsequently as a combination of the above-mentioned functions $A_k^{(1)}$ to $D_k^{(1)}$ ($k = \overline{1, 2}$).

Similar expressions can be obtained for stress and displacement components in the lower material by analogical considerations (see eq. (A.1)-(A.3)).

Thus, the mathematical statement can be reformulated in terms of singular integral equations (SIE) of Cauchy-type similar to [29, 44, 73]. These equations with respect to g_2' , g_4' , f_1 , f_2' are the following (an expanded form is provided in Appendix A):

$$\begin{cases} \sigma_{22}^{(1)}(x_1, h_1, g_1, g_2', f_1, f_2') = P(x_1) \\ \sigma_{22}^{(2)}(x_1, -h_2, g_3, g_4', f_1, f_2) = -P(x_1) \\ \sigma_{22}^{(1)}(x_1, 0, g_1, g_2', f_1, f_2') - \sigma_{22}^{(2)}(x_1, 0, g_3, g_4', f_1, f_2) = 0 \\ \frac{\partial U_1^{(1)}}{\partial x_1}(x_1, 0, g_1, g_2', f_1, f_2') - \frac{\partial U_1^{(2)}}{\partial x_1}(x_1, 0, g_3, g_4', f_1, f_2) = 0 \end{cases} \quad (4.16)$$

The unknown functions g_1 and g_3 can be found directly from the boundary conditions (4.1) by taking into account equation (4.9), the other four unknown functions can be determined by solving system (4.16).

4.2.1.2 Numerical method for the solution of singular integral equations

Analysing the obtained system of integral equations (4.16) with the help of expressions for integral kernels introduced in Appendix A, one can see that the functions $A_k^{(n)}(x_1, 0, \tau)$, $B_k^{(n)}(x_1, 0, \tau)$, $C_k^{(n)}(x_1, h, \tau)$ and $D_k^{(n)}(x_1, h, \tau)$ are continuous functions all over x_1 , whereas the functions $A_k^{(n)}(x_1, h, \tau)$, $B_k^{(n)}(x_1, h, \tau)$, $C_k^{(n)}(x_1, 0, \tau)$ and $D_k^{(n)}(x_1, 0, \tau)$ are singular for $x_1 \rightarrow \tau$ and the singular part is given by:

$$S_1(x_1, \tau) = \frac{1}{x_1 - \tau} \quad (4.17)$$

In integrals (4.13) - (4.15) and analogical integrals for the lower material (A.1) – (A.3), due to St. Venant's principle, one can use $c \gg \max\{h_1; h_2\}$ instead of infinity (∞). Substituting $x_1 = (c + c\chi_1)/2$, $\tau = (c + ct)/2$, system (4.16) can be rewritten in matrix form:

$$\int_{-1}^1 (S_1(\chi_1, t) + Y(\chi_1, t))\Phi(t)dt = F(\chi_1) \quad (4.18)$$

In this form the system of equations (4.16), which describes the equilibrium state of the un-cracked bi-material strip, can be recognized as a system of Fredholm integral equations of first kind with Cauchy-type singular kernels [54]. In (4.18) $\Phi(t)$ is a vector of the unknown functions g_2' , g_4' , f_1 and f_2' , $Y(\chi_1, t)$ is a matrix of regular parts of integral kernels, which can be easily obtained as an algebraic combination of integral kerns $A_k^{(n)}$ to $D_k^{(n)}$ ($k = \overline{1,3}$). The functions in vector $F(\chi_1)$ represent the boundary conditions from the right side of equations in (4.16).

The solution for obtained system of equations is presented in the form [52, 54]:

$$\Phi(t) = \frac{\Phi^{**}(t)}{\sqrt{1-t^2}} \quad (4.19)$$

By applying the Gauss-quadrature rule to (4.18), with taking into account (4.19), the system of four integral equations will reduce to the following 4N-order system of algebraic equations:

$$\begin{cases} \sum_{m=1}^N \frac{\pi}{N} \left(\frac{1}{\chi_l - t_m} + Y(\chi_l, t_m) \right) \Phi^{**}(t_m) = F(\chi_l) \\ \sum_{m=1}^N \frac{\pi}{N} \Phi^{**}(t_m) = Const \end{cases} \quad l = \overline{1, N-1} \quad (4.20)$$

where $t_m = \text{Cos}(\pi(2m-1)/N)$ are roots of Chebyshev polynomials of the first kind of order N and χ_l are determined as $\chi_l = \text{Cos}(\pi l/N)$.

This system has a unique solution with respect to the unknown variables $g'_{2m}, g'_{4m}, f_{1m}, f'_{2m}$ ($m = \overline{1, N}$), which correspond to the values of the unknown functions $g'_2(\tau), g'_4(\tau), f_1(\tau), f'_2(\tau)$ at the collocation points t_m . Thus, the sought-for functions introduced by (4.9) are obtained as a result of interpolation. Therefore, the stress distributions on the interface from (4.15) are evaluated numerically for the case of uncracked bi-material strip depending on the given geometry of joined materials and on the given applied remote loading.

The dependence of obtained solution on the loading conditions is obviously determined by the right side of equation (4.16), while the effect of different strip geometries is more hidden, but could be found in dependences of integral kernels of expressions (4.13)-(4.16) and (A.1)-(A.3) on the height of joined materials h_1 and h_2 . Simple replacement of the height parameters by appropriate geometrical values will lead to solutions inherent for chosen geometries. However, it should be noted that the solution is presented for an infinite bi-material strips, what means that the height of bi-material is significantly smaller than the length of the strip.

4.2.1.3 Verification of the solution procedure

To illustrate the above presented mechanism of solution of singular integral equations, we consider the problem of a homogeneous material strip, infinite in x_1 -direction, with fixed lower border and loaded with uniform distributed tensile stress on the upper border ([Figure 4.3a](#)), as a test case.

4. Mechanical problem of a bi-material strip

The boundary conditions instead of (4.1), (4.2) and (4.3) will be presented as following:

$$\begin{aligned}\sigma_{12}^{(1)}(x_1, h_1) &= 0 & \sigma_{22}^{(1)}(x_1, h_1) &= P \\ U_1^{(1)}(x_1, 0) &= 0 & U_2^{(1)}(x_1, 0) &= 0\end{aligned}\quad (4.21)$$

According to above introduced analyses, the derived system of SIE (4.16) for the problem of a homogeneous strip has a more simple view and can be written as:

$$\begin{cases} \int_0^{\infty} [g_2'(\tau)B_3^{(1)}(x_1, h_1, \tau) + f_1(\tau)C_3^{(1)}(x_1, h_1, \tau)] d\tau = P \\ \int_0^{\infty} [g_2'(\tau)B_1^{(1)}(x_1, 0, \tau) + f_1(\tau)C_1^{(1)}(x_1, 0, \tau)] d\tau = 0 \end{cases}\quad (4.22)$$

In this case we have only two unknown functions $g_2'(\tau)$ and $f_1(\tau)$. The solution of (4.22) is searched in the form of (4.19). Thus, unknown functions can be introduced as $q_2'(t) = \frac{q_2^*(t)}{\sqrt{1-t^2}}$, $f_1(t) = \frac{f_1^*(t)}{\sqrt{1-t^2}}$ using following additional conditions:

$$\int_{-1}^1 q_2^*(t) dt = 0, \quad \int_{-1}^1 f_1^*(t) dt = 0 \quad (4.23)$$

Finally, the 2N-order system of algebraic equations can be written as:

$$\begin{cases} \sum_{k=1}^N \frac{\pi}{N} (g_2^*(t_k)B_3^{(1)}(\chi_l, h_1, t_k) + f_1^*(t_k)C_3^{(1)}(\chi_l, h_1, t_k)) = P \\ \sum_{k=1}^N \frac{\pi}{N} (g_2^*(t_k)B_3^{(1)}(\chi_l, 0, t_k) + f_1^*(t_k)C_3^{(1)}(\chi_l, 0, t_k)) = 0 \\ \sum_{k=1}^N \frac{\pi}{N} g_2^*(t_k) = 0 \\ \sum_{k=1}^N \frac{\pi}{N} f_1^*(t_k) = 0 \end{cases} \quad l = \overline{1, N-1} \quad (4.24)$$

The stress component $\sigma_{22}(x_1, x_2)$ can be obtained from (4.15) using the found functions:

$$\sigma_{22}^{(1)}(x_1, x_2) = \int_0^{\infty} g_2'(\tau) B_3^{(1)}(x_1, x_2, \tau) d\tau + \int_0^{\infty} f_1(\tau) C_3^{(1)}(x_1, x_2, \tau) d\tau.$$

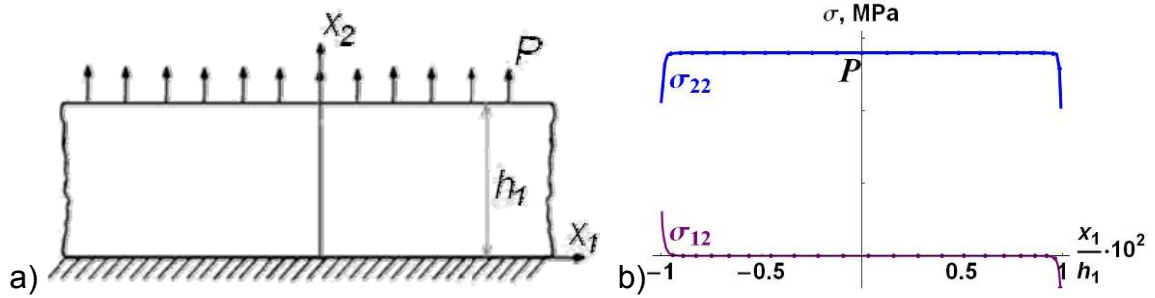


Figure 4.3 - Homogeneous strip with an fixed end under the uniform tensile loading: a) geometry configuration; b) stresses at the “interface” ($x_2 = 0$)

The stress solution on the fixed end of the strip is shown qualitatively in Figure 4.3b. The abscissa coordinate is a coordinate along the fixed end ($x_2 = 0$), normalized by the height of the component. One can see a persistent behaviour of obtained results over the whole interface, except the small regions near the ends of the strip. These effects appear due to the replacement of the upper limit in integrals (4.22) from infinity to $c = 100h_1$. This stress behaviour is limited to the very neighborhood of the strip ends and can be neglected for the case of an infinite strip. The solution is found to be in a good agreement with the numerical results, obtained from a simple FE-model and the results, presented earlier in the literature (e.g. [29, 44, 45]).

4.2.2 An interface crack in an infinite bi-material joint

The mathematical statement for the interface crack in infinite bi-material joint is presented by equilibrium equations (4.6) with the following stress conditions on the bi-material interface:

$$\left. \begin{aligned} \sigma_{k2}^{(1)}(x_1, 0) = \sigma_{k2}^{(2)}(x_1, 0) = 0 \\ U_k^{(1)}(x_1, 0) = U_k^{(2)}(x_1, 0) \end{aligned} \right\}, \quad \text{for } 0 < a \leq |x_1| < \infty \quad k = \overline{1, 2} \quad (4.25)$$

4. Mechanical problem of a bi-material strip

$$\sigma_{22}^{(1)}(x_1, 0) - i\sigma_{12}^{(2)}(x_1, 0) = -p(x_1) + iq(x_1), \quad \text{for } |x_1| \leq a \quad (4.26)$$

where $p(x_1)$ and $q(x_1)$ represent tensile and shear stresses acting on the interface ($x_2 = 0$). According to the solution of problem (a), they are $-\sigma_{22}^{(a)}(x_1, 0)$, $\sigma_{12}^{(a)}(x_1, 0)$ correspondingly.

Problems of such kind were considered by England [24], Erdogan [25] and others.

4.2.2.1 Derivation of the Hilbert problem

Problem (b) simplifies to the classical Hilbert problem. The solution for the stress state at the tip of interface crack is obtained by rewriting the basic relations for two-dimensional classical elasticity in the form of Kolosov-Muskhelishvili equations. This means that stresses and displacements in any point of the component are presented in terms of two unknown functions – complex potentials $\varphi(z)$ and $\Psi(z)$ [55]:

$$\begin{cases} \sigma_{11}^{(n)} + \sigma_{22}^{(n)} = 4[\varphi_n'(z) + \overline{\varphi_n'(\bar{z})}] \\ \sigma_{22}^{(n)} - i\sigma_{12}^{(n)} = 2[\varphi_n'(z) + \overline{\varphi_n'(\bar{z})} + \overline{\varphi_n''(\bar{z})} + \overline{\Psi_n''(\bar{z})}] \\ \mu_n(U_1^{(n)} + U_2^{(n)}) = (3 - 4\nu_n)\varphi_n(z) - z\overline{\varphi_n'(\bar{z})} - \overline{\Psi_n'(z)} \end{cases}, \quad (4.27)$$

where $z = x_1 + ix_2$ and $\bar{z} = x_1 - ix_2$.

If we denote $\lim_{x_2 \rightarrow 0^+} \varphi(z) = \varphi^+(x_1)$ and $\lim_{x_2 \rightarrow 0^-} \varphi(z) = \varphi^-(x_1)$, then from continuity conditions (4.25) and representation (4.27) for the displacements in the upper and lower material we can rewrite:

$$\mu_2 \left[(3 - 4\nu_1)\varphi_1^+(x_1) - x_1 \overline{\varphi_1'^-(x_1)} - \overline{\Psi_1'^-(x_1)} \right] = \mu_1 \left[(3 - 4\nu_2)\varphi_2^-(x_1) - x_1 \overline{\varphi_2'^+(x_1)} - \overline{\Psi_2'^+(x_1)} \right]$$

or

$$\mu_2(3 - 4\nu_1)\varphi_1^+(x_1) + \mu_1 x_1 \overline{\varphi_2'^+(x_1)} + \mu_1 \overline{\Psi_2'^+(x_1)} = \mu_1(3 - 4\nu_2)\varphi_2^-(x_1) + \mu_2 x_1 \overline{\varphi_1'^-(x_1)} + \mu_2 \overline{\Psi_1'^-(x_1)}$$

This equation describes the fact that displacements are continuous over the uncracked part of the interface. This will be identically satisfied, if we present a function $\Phi(z)$ in following way:

$$\begin{aligned} \mu_2(3-4\nu_1)\varphi_1(z) + \mu_1 z \overline{\varphi_2'(z)} + \mu_1 \overline{\Psi_2'(z)} &= \Phi(z), & z \in S^+ \\ \mu_1(3-4\nu_2)\varphi_2(z) + \mu_2 z \overline{\varphi_1'(z)} + \mu_2 \overline{\Psi_1'(z)} &= \Phi(z), & z \in S^- \end{aligned} \quad (4.28)$$

where S^+ denotes the upper half-plane and S^- the lower half-plane respectively. Function $\Phi(z)$ is a holomorphic function over the whole plane cut along the crack length.

In a similar way another holomorphic function $\Theta(z)$ in whole plane cut along $(-a, a)$ can be presented. This function provides the continuity conditions of the stresses over the interface:

$$\begin{aligned} \varphi_1'(z) - \overline{\varphi_2'(z)} - z \overline{\varphi_2''(z)} - \overline{\Psi_2''(z)} &= \Theta(z), & z \in S^+ \\ \varphi_2'(z) - \overline{\varphi_1'(z)} - z \overline{\varphi_1''(z)} - \overline{\Psi_1''(z)} &= \Theta(z), & z \in S^- \end{aligned} \quad (4.29)$$

Solving equations (4.28) and (4.29) with respect to complex potentials, we find:

$$\begin{aligned} (\mu_1 + \mu_2(3-4\nu_1))\varphi_1'(z) &= \mu_1\Theta(z) + \Phi'(z), & z \in S^+ \\ (\mu_2 + \mu_1(3-4\nu_2))\varphi_2'(z) &= \mu_2\Theta(z) + \Phi'(z), & z \in S^- \end{aligned} \quad (4.30)$$

and the complex potentials $\overline{\Psi_1'(z)}$, $\overline{\Psi_2'(z)}$ are determined in (4.28). Thus, the continuity conditions at the interface are satisfied and only one boundary condition (4.26), which describes the stress state at the crack faces, is remaining. Combining (4.26) with expressions (4.28) and (4.30), and assuming that stress and rotation in materials vanish at infinity for large $|z|$ ($\Phi'(z) = O(1/z^2)$ and $\Theta(z) = O(1/z^2)$), our problem will reduce to a Hilbert problem in the form:

4. Mechanical problem of a bi-material strip

$$\Phi'^+(x_1) + \frac{\mu_1 + \mu_2(3-4\nu_1)}{\mu_2 + \mu_1(3-4\nu_2)} \Phi'^-(x_1) = \frac{\mu_1 + \mu_2(3-4\nu_1)}{2} [p(x_1) - iq(x_1)] \quad (4.31)$$

for $|x_1| \leq a$

from which the piecewise-holomorphic function should be determined.

4.2.2.2 Solution procedure for the Hilbert problem

Muskhelishvili [56] gave a solution to the Hilbert problem for the case when the crack is presented by the union of line segments (what corresponds to the finite number of interface cracks). Applying his solution to the case of a single line crack, one can get:

$$\Phi'(z) = -\frac{\mu_1 + \mu_2(3-4\nu_1)}{4\pi i \sqrt{z^2 - a^2}} \left(\frac{z+a}{z-a}\right)^{-i\epsilon} \int_{-a}^a \left[\frac{\sqrt{t^2 - a^2}}{(t-z)} \left(\frac{t+a}{t-a}\right)^{i\epsilon} (p(t) - iq(t)) \right] dt + \frac{1}{\sqrt{z^2 - a^2}} \left(\frac{z+a}{z-a}\right)^{-i\epsilon} N(z) \quad (4.32)$$

This solution refers to the branches which are holomorphic in the whole plane cut along $(-a, a)$, with an arbitrary polynomial $N(z)$. Since $\Phi'(z) = O(1/z^2)$ for $|z| \rightarrow \infty$, it leads to $N(z) \equiv 0$.

Now, the stresses over the interface for the problem (b) can be determined from (4.27), (4.28) and (4.30), what yields to:

$$\sigma_{22}^{(b)}(x_1, 0) - i\sigma_{12}^{(b)}(x_1, 0) = 2 \left[\frac{1}{\mu_1 + \mu_2(3-4\nu_1)} \Phi'^+(x_1) + \frac{1}{\mu_2 + \mu_1(3-4\nu_2)} \Phi'^-(x_1) \right] \quad (4.33)$$

with

$$\Phi'(z) = -\frac{\mu_1 + \mu_2(3-4\nu_1)}{4\pi i \sqrt{z^2 - a^2}} \left(\frac{z+a}{z-a}\right)^{-i\epsilon} \int_{-a}^a \left[\frac{\sqrt{t^2 - a^2}}{(t-y)} \left(\frac{t+a}{t-a}\right)^{i\epsilon} (\sigma_{22}^{(a)}(t, 0) - i\sigma_{12}^{(a)}(t, 0)) \right] dt \quad (4.34)$$

According to the superposition principle (4.7), presented in the beginning of the chapter (4.2) and using the obtained expressions for the interface stresses of problem (a) – (4.9), (4.15) and problem (b) – (4.33), the initial problem of a bi-material strip with interface crack is considered to be solved.

Thus, when tensile and shear stresses at the interface are known, the value of the mode-mixity parameter can be found from the interface stresses $\sigma_{22}^{(com)}(x_1, 0)$ and $\sigma_{12}^{(com)}(x_1, 0)$ of the combined solution. Because of logarithmic singularities in the expressions of stress components at the tip of the interface crack, the value of mode-mixity parameter $\psi = \tan^{-1} \left(\sigma_{12}^{(com)}(x_1, 0) / \sigma_{22}^{(com)}(x_1, 0) \right)$ has to be determined at some distance L from the tip crack, as it was described in (2.18). England [24] showed that the good correspondence of the solution with the physical state of the component is provided for points at a small distance not less than $L = 2,52 \cdot 10^{-4} a$ from the end of the crack.

4.3 Parametric study and discussion of the results

We consider a specific case of the general solution – the problem of a bi-material strip with an internal interface crack (Figure 4.1) under uniform loading. That means constant normal and shear stresses ($P(x_1) = Const, Q(x_1) = Const$), with respect to x_1 -coordinate are applied on the upper and lower boundaries of the examined bi-material strip.

According to the solution procedure presented in section 4.2, the stress components $\sigma_{k2}^{(n)}$ ($k=1,2$) for the problems (a) and (b) can be determined on the interface of the two materials. It should be noted that for the problem (b) the expression for the holomorphic function $\Phi'(y)$ can be simplified, in this case the integral in (4.34) is evaluated analytically and one obtains:

$$\Phi'(z) = -\frac{(\mu_1 + \mu_2(3 - 4\nu_1))(\mu_2 + \mu_1(3 - 4\nu_2))}{8(\mu_2(1 - \nu_1) + \mu_1(1 - \nu_2))} \left[1 - \left(\frac{z+a}{z-a} \right)^{-i\varepsilon} \frac{(z+2ai\varepsilon)}{\sqrt{z^2 - a^2}} \right] (P - iQ) \quad (4.35)$$

Thus, normal ($\sigma_{22}^{(b)}$) and shear ($\sigma_{12}^{(b)}$) stresses can be evaluated from (4.33) by separating real and imaginary parts of the expression and taking into account

4. Mechanical problem of a bi-material strip

that on the uncracked part of the interface $\Phi^{'+}(x_1) = \Phi'^-(x_1) = \Phi'(x_1)$ holds. The solution of the problem is obtained according to the superposition principle (4.7).

Numerical calculations were carried out for a bi-material strip consisting of a material pair $Al_2O_3 - ZrO_2$ with $E_1 = 347GPa$, $\nu_1 = 0.21$ and $E_2 = 213GPa$, $\nu_2 = 0.32$. The corresponding Dundurs' parameters, which characterize the bi-material behaviour are calculated as $\alpha = 0.209$ and $\beta = 0.015$. The corresponding oscillation index for the bi-material pair is $\varepsilon = 0.0048$.

Three characteristic loading cases are considered and analysed:

- a. Pure uniform tensile stresses are acting on the boundaries of the bi-material strip ($P(x_1) = P$, $Q(x_1) = 0$).
- b. Pure uniform shear stresses are acting on the boundaries of the bi-material strip ($P(x_1) = 0$, $Q(x_1) = Q$).
- c. Combined uniform tensile and shear stresses of equal magnitude are applied on the boundaries of the bi-material strip ($P(x_1) = P$, $Q(x_1) = Q$, $Q/P = 1$).

In [Figure 4.4](#) normal and shear stress distributions over the interface part close to the crack tip are shown for the three cases (a), (b), (c).

One can see that the presence of pure tensile stresses (Figure 4.4a) acting on the borders of the bi-material strip ($Q/P = 0$) causes weak shear effects near the tip of the crack. The mode-mixity factor in this case is $\psi = 0.03$ compared to $\psi = 0$ for the homogeneous material. The effect of elastic mismatch across the interface is also observed for the loading combinations (b) (Figure 4.4b) and (c) (Figure 4.4c), where it causes slight differences in the normal (σ_{22}) and shear (σ_{12}) stresses.

The dependence of crack-tip parameter ψ on the varying ratio of applied shear and tensile loadings (Q/P) is shown in [Figure 4.5](#). The dashed line corresponds to a homogeneous material with Dundurs' parameters $\alpha = 0$, $\beta = 0$. One can see that for the considered $Al_2O_3 - ZrO_2$ pair of materials (red curve) the effect of dissimilarity in elastic constants of joined materials is only weak ($\psi = 0.03$) compared with the homogeneous case.

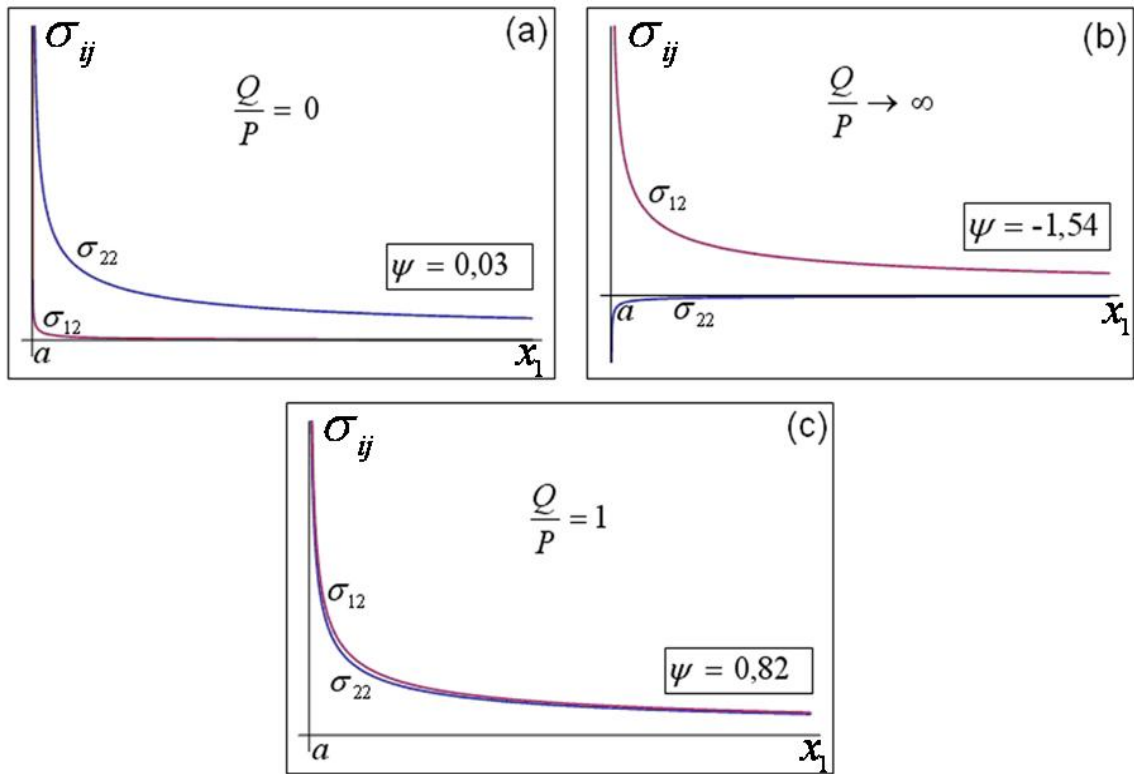


Figure 4.4 - Stresses on the interface of a bi-material strip: (a) $Q/P = 0$; (b) $Q/P \rightarrow \infty$; (c) $Q/P = 1$.

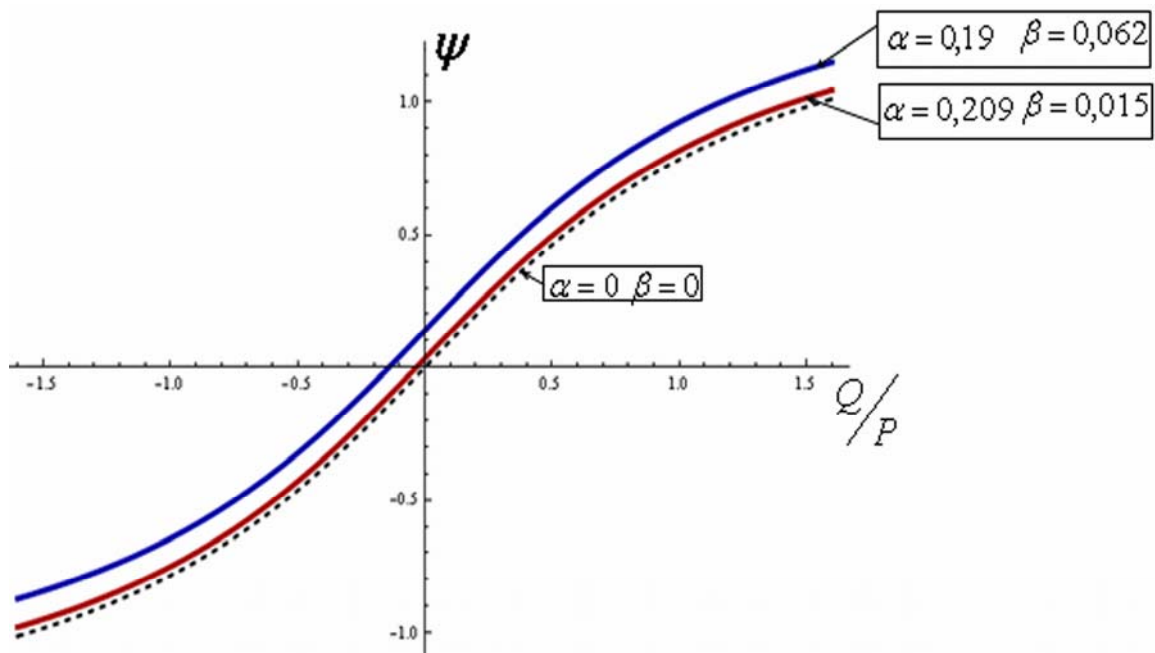


Figure 4.5 - Dependence of mode-mixity parameter on the ratio of applied shear and tensile loading.

4. Mechanical problem of a bi-material strip

For a comparison, the blue curve in Figure 4.5 shows the dependence of the ψ -parameter on Q/P -ratio for a variation of the bi-material combination, where the same ZrO_2 ceramic is combined with an Al_2O_3 of higher porosity ($E_1 = 147 \text{ GPa}$, $\nu_1 = 0.30$). Dundur's parameters can be found to be $\alpha = 0.190$, $\beta = 0.62$. Here, the oscillation index is larger than in the previous case and equals $\varepsilon = 0.02$. As a result, we observe a larger shift with a ψ value of 0.14 for applied pure mode-I ($Q/P = 0$).

An important result is the fact that the mode-mixity parameter is a non-local quantity in this case, i.e. that its value depends on the local crack tip stress field only through the remote boundary loading conditions P and Q . This will still be approximately the case for the general problem of a bi-material strip under an arbitrary stress state, as long as the remote loading ratio of shear to tensile stress (Q/P) does not vary strongly along the x_1 -axis. Thus, the mode-mixity parameter can be treated as a global quantity in the general loading case. Therefore, the term $\sqrt{1 + \tan^2 \psi}$ can be taken out of the integrals in equation (3.31), since it is independent of the integration variables - crack location and orientation in the stress field.

For the case of a constant Q/P -ratio with respect to the in-plane coordinates, applying simple algebraic transformations to the expression (3.31), the interface failure probability can be rewritten as:

$$P_F = 1 - \exp \left[- \left(\frac{\sigma^*}{b_1 \sqrt{1 + \tan^2 \psi}} \right)^m \right] \quad (4.36)$$

with b being replaced by $b_1 \sqrt{1 + \tan^2 \psi}$.

The parameters m and b_1 of the Weibull distribution, which are independent of the ψ -parameter, have to be determined experimentally for each bi-material pair. The schematic representation of interface failure probability depending on the crack tip stress state is shown in [Figure 4.6](#), where P_F^I is the value of failure probability for vanishing mode-mixity parameter.

One can see that a maximum of P_F is achieved when the crack tip is under mode-I ($\psi = 0$) loading. For the case of pure mode-II ($\psi = \pi/2$) loading the probability of component's failure due to the crack propagation along the interface vanishes. However, it should be noted that in this case crack kinking out of the interface has to be considered as a failure mode, depending on the toughness of the joined materials, as it was shown in (2.22). Thus, the value of interface failure probability for a specified bi-material joint under arbitrary loading conditions can be either estimated conservatively by the maximum value at $\psi = 0$ or calculated according to the algorithm presented above considering the exact stress state at the interface.

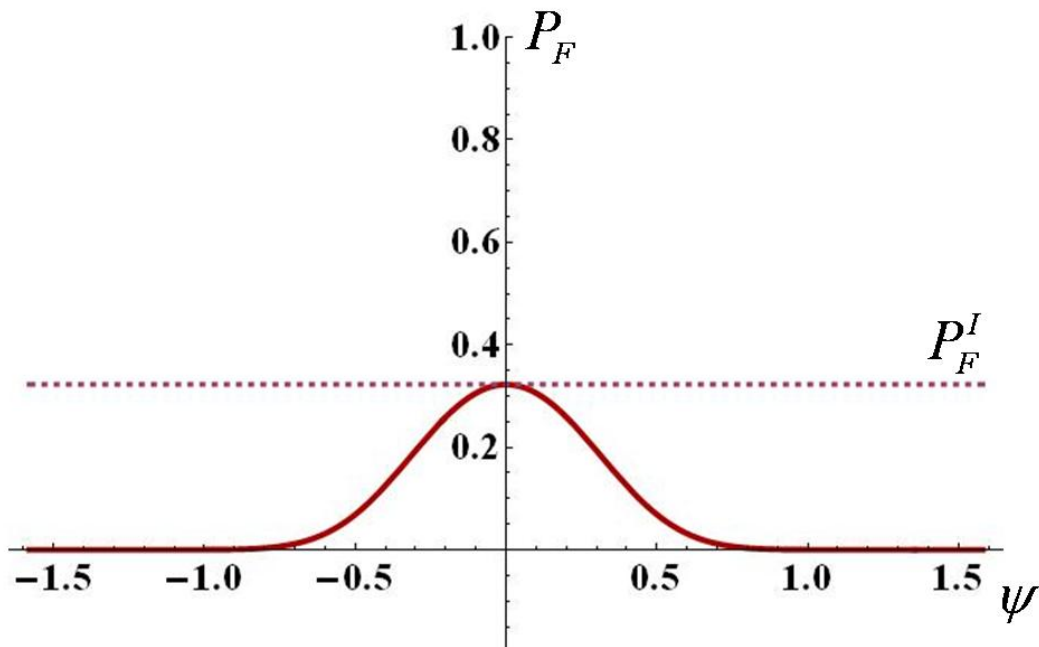


Figure 4.6 - Dependence of interface failure probability on the ψ -parameter (P_F^I corresponds to pure mode-I loading).

The presented solution algorithm for the stress state on the interface based on the evaluation of singular integral equations and complex variable method allows a general treatment of weakest-link interface failure probability in the case of complex component geometries. The remote stresses for the boundary conditions will generally be taken from a Finite Element stress analysis of the whole component under consideration.

5. Experimental characterization of material and interface strength

The experimental characterization of interfaces is an essential part of the reliability analysis of composite components. As it was shown in the previous chapters, the strength distribution of interfaces in ceramic joints can be described by two material parameters m and b . These parameters of the Weibull distribution for the strength of the interfaces need to be determined from the empirically observed data. The numerical procedure of the estimation of m and b based on experiments is presented in chapter 5.1 by the example of the commonly used Maximum-Likelihood method (MLM). The course of experiments as well as the results of the tests and their analysis are presented in chapters 5.2 and 5.3.

5.1 Estimation of Weibull parameters

The strength of brittle materials varies from specimen to specimen. As a consequence, the material resistance against failure is not a specific value, but a distribution of strength values. The scatter in the strength of ceramic materials is significantly larger compared to metals. For ceramic-ceramic interfaces, as in the case of homogeneous materials, cracks originate from small defects. Therefore, the scatter of interface strength is caused by the scatter of the interface flaw size.

For accurate results in determining the distribution parameters, m and b , the Maximum-Likelihood method is used. This method requires to specify density functions $f(x_i | \mathcal{G}_1, \dots, \mathcal{G}_p)$ for all the observations x_i , where $\mathcal{G}_j (j = \overline{1, p})$ are the distribution parameters. In our case p equals 2 ($\mathcal{G}_1 = m$ and $\mathcal{G}_2 = b$) and $x_i (i = \overline{1, N})$ are random values of the distribution, which correspond to the

5. Experimental characterization of material and interface strength

strength values σ_{ci} , that are measured in each i -th experiment. Now, the Likelihood function can be written as:

$$L_f(m, b, \sigma_{c1}, \dots, \sigma_{cN}) = f(\sigma_{c1} | m, b) \cdot f(\sigma_{c2} | m, b) \cdot \dots \cdot f(\sigma_{cN} | m, b) \quad (5.1)$$

The best set of parameters m and b leads to the maximum value of the L -function. Searching for supremum

$$\frac{\partial L_f(\sigma_{c1}, \dots, \sigma_{cN}, \vartheta_1, \vartheta_2)}{\partial \vartheta_i} \quad (5.2)$$

the estimators of Weibull parameters for given sample values σ_{ci} will be found.

Expression (5.2) reduces to a system of two non-linear equations in the case of a Weibull distribution [53]:

$$\begin{cases} \frac{1}{m} = \frac{\sum_{i=1}^N (\ln \sigma_{ci} \cdot \sigma_{ci}^m)}{\sum_{i=1}^N (\sigma_{ci}^m)} - \frac{1}{N} \sum_{i=1}^N (\ln \sigma_{ci}) \\ b^m = \frac{1}{N} \sum_{i=1}^N (\sigma_{ci}^m) \end{cases} \quad (5.3)$$

From the first equation of system (5.3), one can see that the value of the Weibull parameter m can be directly determined based on the experimentally obtained data and the second equation provides the geometry dependent parameter b . Applying (3.17), the material dependent Weibull parameter σ_0 can be found and subsequently converted for any geometry.

Another method, which is less exact but gives fast and good visualised estimation procedure, is a probability plotting method. Equation (3.14) describes the strength distribution of interfaces, with Weibull parameter b determined by (3.32). Finding the logarithm of the left- and right-side of (3.14) one gets:

$$\ln \ln \left(\frac{1}{1 - P_F} \right) = m \ln(\sigma_*) - m \ln(b) \quad (5.4)$$

5.1 Estimation of Weibull parameters

For plotting the strength data (σ_{ci}) obtained from N experiments ($i = \overline{1, N}$) are ranked in increasing order. Each strength value σ_{ci} is related to the failure probability P_{Fi} . Different estimations used for the probability function are listed in [10]. Here, we use the form valid for the approximation of an average value for each i -th observation, namely P_{Fi} is defined as:

$$P_{Fi} = \frac{i}{N+1} \quad (5.5)$$

The plot $\ln \ln(1/(1-P_F))$ versus $\ln(\sigma_*)$ will provide the Weibull parameters. For clarity the representation of the strength scatter data for Al_2O_3 (99.6%) is shown in [Figure 5.1](#).

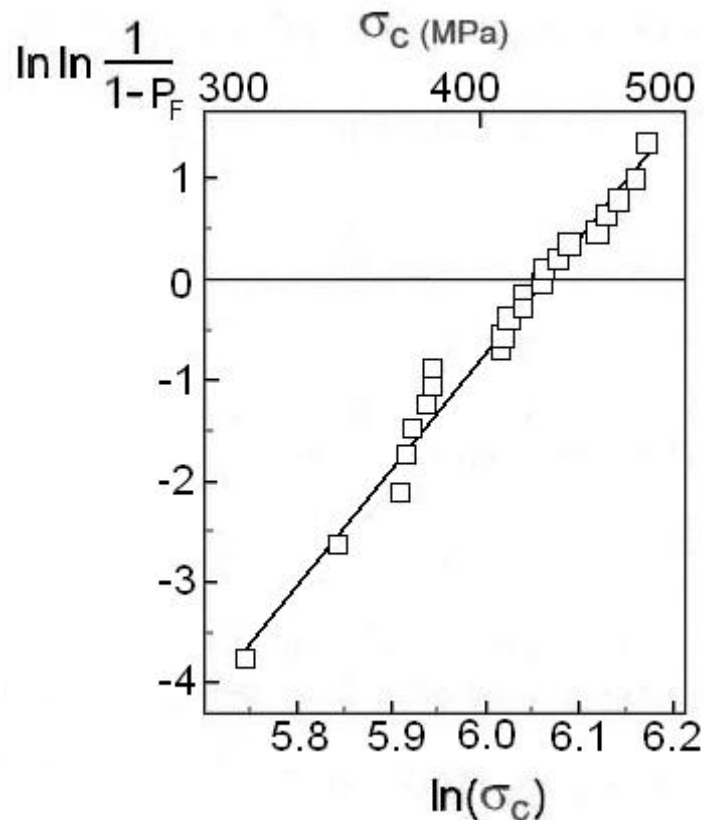


Figure 5.1 – Representation of the scatter in strength by a Weibull diagram for Al_2O_3 (99.6%) [53]

5. Experimental characterization of material and interface strength

The slope of the straight approximation line corresponds to the value of parameter m . Coefficient $\ln b$ is obtained as a shift of the line along the axis of abscissas. It follows from (5.4) that Weibull parameter b corresponds to the strength value σ_c with $P_F = 63.2\%$ ($\ln \ln(1/(1-P_F)) = 0$).

5.2 Interface strength considerations

To characterize the strength of ceramic-ceramic interfaces a number of experiments were carried out using the facilities of an industrial partner (Robert Bosch GmbH) [64]. For determination of the maximum interface stresses four point bending (4PB) tests were performed. During these tests three main specimen configurations were used to keep the material interface on different distances from the zero-axis (see [Figure 5.2](#)). Correspondingly, interfaces experience either compressive or tensile stresses.

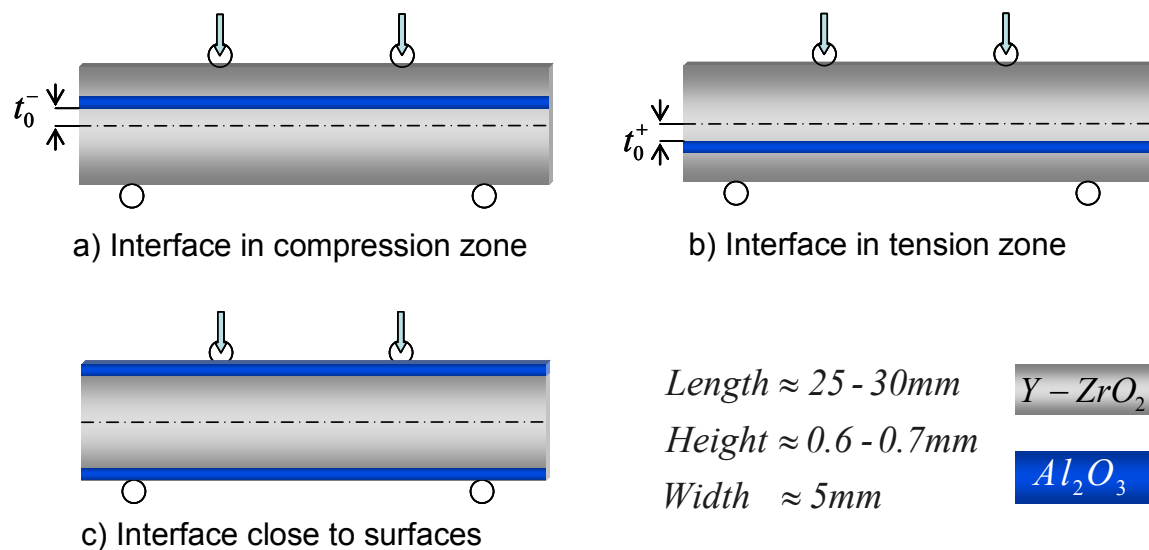


Figure 5.2 – Schematic representation of the 4PB test samples

The samples were produced by the tape casting and the screen printing methods. Materials used for the 4PB specimens were Ytria-stabilised Zirconia ($Y-ZrO_2$) and Alumina of two different types ($Al_2O_3(LP)$ -low porosity and $Al_2O_3(HP)$ -high porosity). Mechanical properties of these materials are summarized in [Table 5.1](#).

5.2 Interface strength considerations

For the example of pre-notched 4PB specimen, the typical result for a layered component is shown in [Figure 5.3](#). A schematic load-displacement diagram contains four representative sections: the first straight line segment represents the linear-elastic behaviour, which is described by Hooke's law. It is followed by a sudden load drop related to the instantaneous crack propagation towards to the interface. The third domain is a plateau, which corresponds to the crack growth along the interface and the last segment is related to the crack propagation into the substrate material and the straight line has the slope equal to the remaining sample stiffness.

In our case, initially uncracked samples were tested and during the loading process load-displacement curves were examined.

Table 5.1 – Mechanical properties of joined materials

	$Y-ZrO_2$	Low porosity $Al_2O_3(LP)$	High porosity $Al_2O_3(HP)$
Density (g/cm^3)	5.75	3.63	2.757
Young's modulus (GPa)	213	347	147
Poisson ratio	0.32	0.21	0.3
Expansion coefficient (1/K)	9.29 e-06	6.7 e-06	7.09 e-06

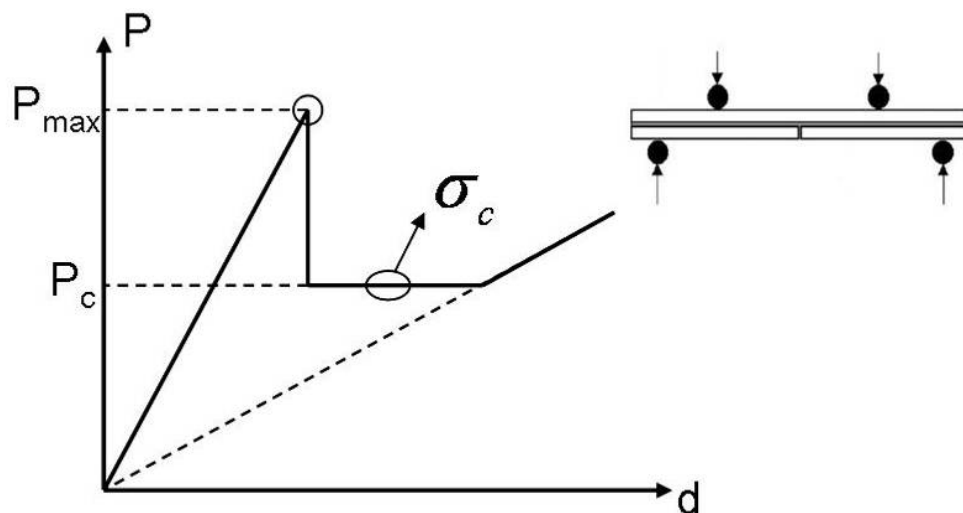


Figure 5.3 – Schematic load-displacement plot for notched 4PB specimen

5. Experimental characterization of material and interface strength

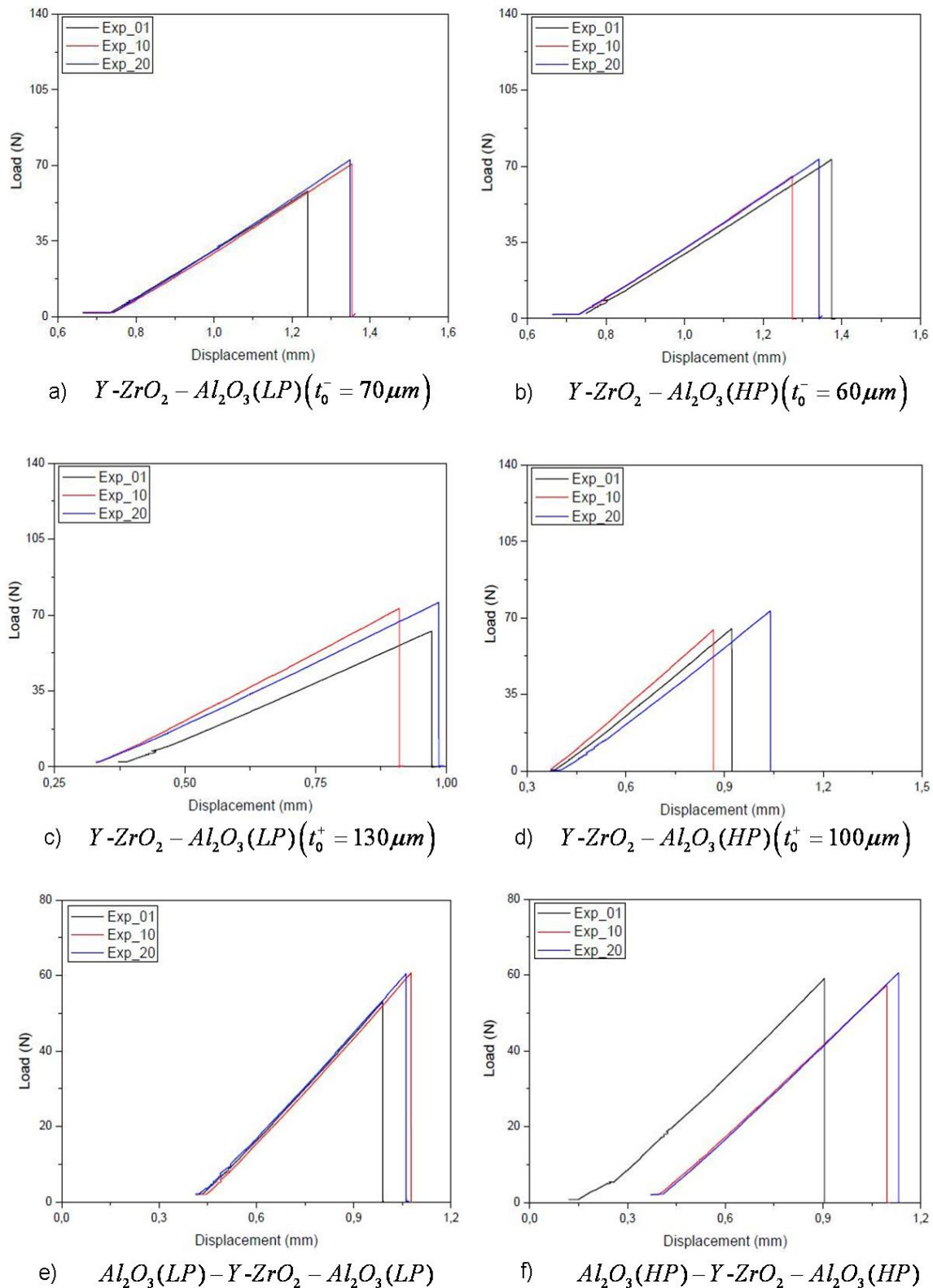


Figure 5.4 – Load-displacement plots [64] for various specimen geometries (see Figure 5.2)

For each material combination and geometry structure 20 samples were tested to obtain statistical data. The bending of the samples was carried out

under displacement control with the constant displacement rate of 0.5mm per minute.

Typical load-displacement plots are shown in [Figure 5.4](#). It can be seen that there are no specific indications in the data, which could be related to interface failure. Contrary to the expectations, no load plateau, load drop or slope change occurred. This indicates that the failure was most likely caused by surface defects. The fractographic analysis confirmed that in most cases fracture origin was located at the tensile surface of the specimens.

For the samples of the $\text{Al}_2\text{O}_3 - \text{Y-ZrO}_2 - \text{Al}_2\text{O}_3$ type (Figure 5.2c), where the material interface is close to the fracture surface, most of the natural flaws which consequently caused the fracture were observed very close to the interface, but still in the Y-ZrO_2 -layer (see [Figure 5.5](#)). Only for one specimen, the fracture origin was present right at the interface as noticed by Scanning Electron Microscopy (SEM) results. Since no interface fracture occurred, an assessment of the interface strength is not possible from these experimental results and alternative methods are necessary.

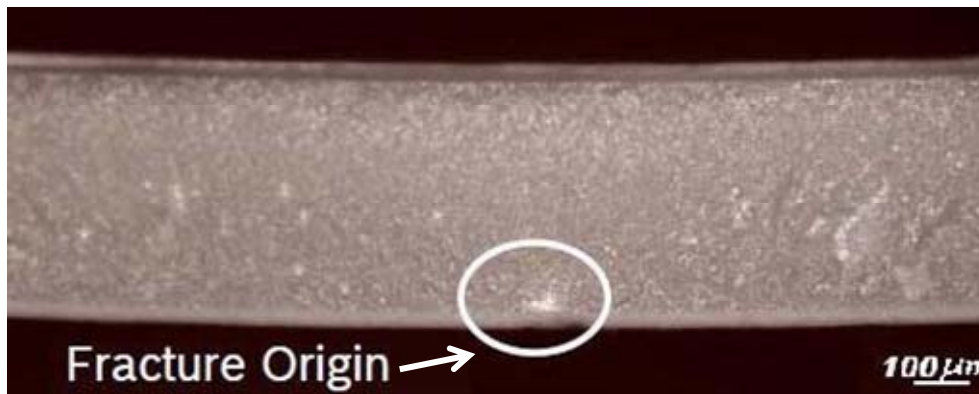


Figure 5.5 – Fracture origin in $\text{Al}_2\text{O}_3(\text{HP}) - \text{Y-ZrO}_2 - \text{Al}_2\text{O}_3(\text{HP})$ specimen [64]

This first approach to characterize the strength of ceramic interfaces by 4PB strength tests proved essentially unsuccessful. Although a number of authors have used macroscopic pre-cracks to investigate the fracture mechanical properties of interfaces [7, 8, 66, 68], probabilistic strength data of such components, especially for ceramic interfaces where natural flaws are relevant for fracture, are not available. Alternative sample geometries, which possibly

5. Experimental characterization of material and interface strength

produce more informative results, were proposed by Tahir [64], but have not been tested so far.

5.3 Discussion of results

As mentioned in the previous section, experimental results were not sufficient to provide a data base for the strength of interfaces. As a rough estimation, however, using the limited empirical data which were obtained, the interval for the values of Weibull strength parameter σ_0 will be assessed.

For the single observed interface crack, which occurred in the case of $Al_2O_3(HP) - Y-ZrO_2 - Al_2O_3(HP)$ 4PB specimen, the critical crack length $a_{ex} = 19,74 \mu m$ was measured from the SEM image (see [Figure 5.6](#)).

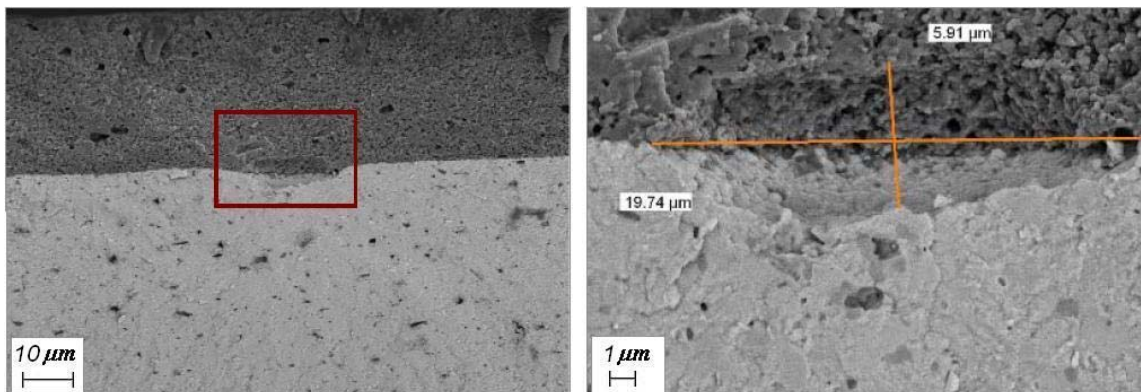


Figure 5.6 – Sizing of the observed interface crack from Scanning Electron Microscopy image [64]

Moreover, interface toughness measurements were conducted for notched 4PB specimen. The energy release rate for $Al_2O_3 - Y-ZrO_2$ interface was calculated to be $G_{i,ex} = 24,2 J / m^2$. Using expression (3.30) and assuming that the specimen with only one interface crack of given length is under tensile loading ($\psi_{ex} = 0.14$), one can find the outer fibre stress σ^* at fracture. The numerical value is equal to 390 MPa.

Since we do not have enough information about the possible crack size distribution, we will assume that the obtained value of stress at fracture is typical either of the smallest flaws, which cause failure only in 10% of all cases, or of the

flaws of the largest size, which cause failure in 90% of cases. These values correspond to two limiting cases and will be used to estimate the interval of material strength parameter σ_0 for the $Al_2O_3 - Y-ZrO_2$ interface.

According to the methods presented in chapter 5.1, Weibull parameter σ_0 can be estimated for given values of m . Here we analyse three representative cases (see [Figure 5.7](#)): large scatter of strength data ($m=10$ - blue lines), medium scatter ($m=18$ - red dotted lines) and small scatter ($m=35$ - purple dashed lines). Hence, the widest range of σ_0 -values, corresponding to $m=10$, is 358–488 MPa. It gives us a rough understanding about the possible values for the interface strength, which are shown to be lower than the strength values for the surrounding homogeneous materials (Al_2O_3 and $Y-ZrO_2$). In the small scatter case ($m=35$), the interval for the strength values is only 35 MPa. This allows to approximate σ_0 with the average value (398 MPa) from the interval with an error of 8.8%, which is an acceptable error comparing with the admissible errors, e.g. in determination of elastic constants.

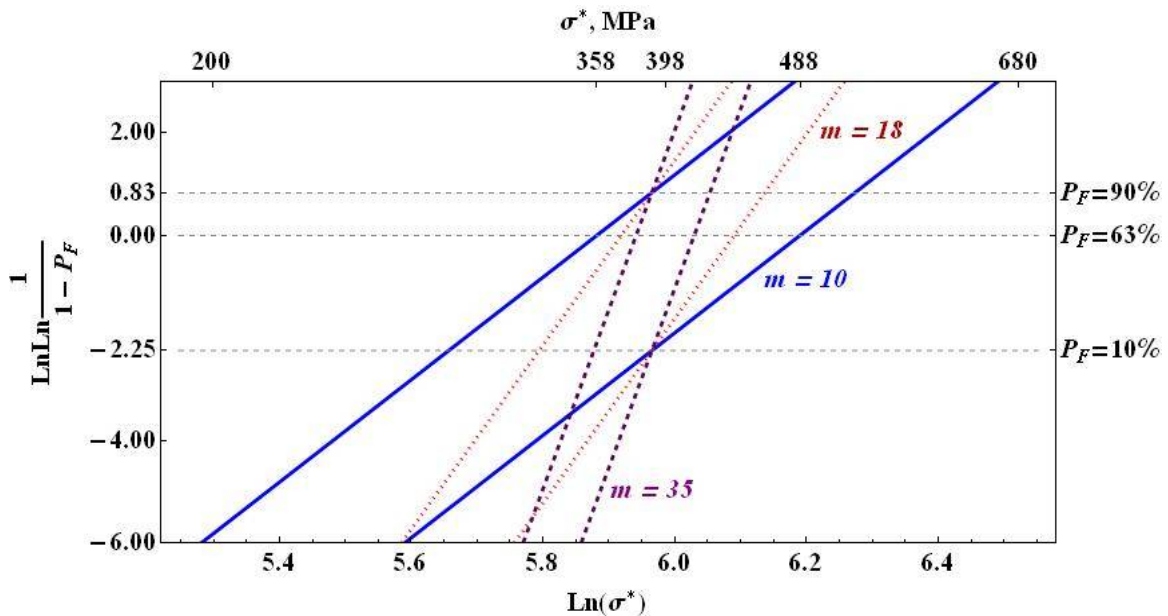


Figure 5.7 - Range of Weibull straight lines for different material properties

Following the discussion of this chapter, the question is addressed, how sensitive the interface failure probability is to the changes of Weibull parameters. Therefore, a parametric study was performed (see chapter 6) to examine the behaviour of the failure probability for the possible range of Weibull parameters

5. Experimental characterization of material and interface strength

m and σ_0 . The aim of the parametric study is twofold: first, to evaluate suitable bi-material sample geometries for new experiments in order to obtain the failure along the interface, and second, to explore possible domains of small sensitivity of failure probability to variations in one or both of the Weibull parameters for the strength distribution.

6. Numerical study and discussions

In this chapter an algorithm of failure probability calculations will be introduced by numerical evaluations of Brazilian disk and 4PB specimens. First, the stress analysis of the bi-material sample has to be performed. For this purpose, FE-models as a basis for STAU calculations are built in ABAQUS (see chapter 6.2). We will treat two-dimensional (2D) and three-dimensional (3D) models separately in order to test the available procedures in STAU program. Facilitating the task, as a pre-step before changing the STAU code, the numerical integration routine has been performed using the commercial software Mathematica (Wolfram Research). For the 3D problems, two different crack models are considered: “through-wall” crack model and “penny-shaped” crack model (see chapter 6.1). The preference for one or the other model will be discussed below.

At the present stage, the stresses in each node of the interface line (2D case) or interface plane (3D case) are taken from the FE-model. This data form an input file which is read by Mathematica for the following analysis. For each of the chosen crack models, equivalent stresses and mode-mixity parameters are determined and the failure probability is calculated at a chosen stress level resulting in a parametric study for the Weibull parameters (see chapter 6.3).

The results of the chapter are discussed in order to give the recommendations for next experimental observations and measurements as well as for future possible extensions of the STAU program.

6.1 Crack models under consideration

For the 2D case we consider a bi-material component, where the interface is introduced by a line. All natural flaws are supposed to be oriented along the interface. It is sufficient to describe them through the “through-wall” crack model,

6. Numerical study and discussions

where the only characteristics of the interface crack is its length. According to the given determination of equivalent stresses (chapter 3.4) and expressions (2.19), (3.25) and (3.26), one will obtain:

$$\sigma_{eq} = \sqrt{\sigma_n^2 + \sigma_\tau^2}, \quad (6.1)$$

where σ_n, σ_τ - are normal and shear stresses acting along the bi-material interface.

For the 3D model, the interface is presented by a two-dimensional plane. In this chapter two different crack models are examined. First, “through-wall” cracks having a characteristic length a are assumed to be arbitrarily oriented with respect to the interface plain. The stress state at the tip of such a crack is described by normal stresses (σ_n), in-plane ($\sigma_{\tau 1}$) and out-of-plane ($\sigma_{\tau 2}$) shear stresses (see [Figure 6.1a](#)).

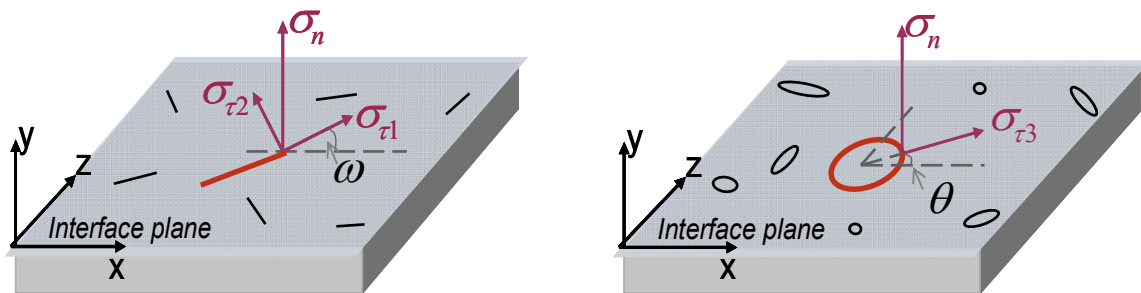


Figure 6.1 - Stress state in arbitrary point of interface for 3D case: a) “through-wall” crack model; b) “penny-shaped” crack model

“Penny-shaped” cracks are modelled as the cracks of radius a . In each point of the crack circumference, the stress state is presented by a resultant shear stress vector ($\sigma_{\tau 3}(\theta)$) and by the normal stress (σ_n) (see [Figure 6.1b](#)).

To take properly out-of-plane stress in the 3D case into account, we have to introduce in the equation for the interface energy release rate (2.19) one additional (mode-III) term [6]:

$$G_i = \frac{1}{H_1} (K_1^2 + K_2^2) + \frac{1}{H_2} K_{III}^2, \quad (6.2)$$

where the in-plane stress field in the vicinity of the crack tip is governed by a complex stress intensity factor $K = K_1 + iK_2$, and the out-of-plane stress field is governed by a real stress intensity factor K_{III} . Parameter H_2 depends on material properties of considered bi-material and has the following form:

$$\frac{1}{H_2} = \frac{\mu_1 + \mu_2}{4\mu_1\mu_2}.$$

The critical energy release rate from equation (2.24) in the three-dimensional case is extended to $G_{icr} = G_{Icr} (1 + \tan^2 \psi) (1 + \tan^2 \phi)$, where ϕ is a second mode-mixity parameter, which measures the relative amount of out-of-plane stresses to in-plane stresses and determined as:

$$\phi = \text{ArcTan} \left(\sqrt{\frac{H_1}{H_2} \frac{K_{III}}{\sqrt{K_1^2 + K_2^2}}} \right) \quad (6.3)$$

Taking into account the above expression for G_i , the interface failure probability becomes:

$$P_F = 1 - \exp \left(- \frac{1}{A_0} \int_{A_i} \frac{1}{2\pi} \int_{\Omega} \left(\frac{\sigma_{eq}(x, z, \omega)}{\sigma_0 \sqrt{(1 + \tan^2 \psi) (1 + \tan^2 \phi)}} \right)^m d\Omega dA_i \right) \quad (6.4)$$

The procedure for determination of equivalent stresses for each crack model is described in Appendix B. Finally for “through-wall” cracks model the expression for equivalent stress is:

$$\sigma_{eq} = \sqrt{\sigma_n^2 + \sigma_{\tau_1}^2 + \frac{H_1}{(1 + 4\varepsilon^2)H_2} \sigma_{\tau_2}^2}, \quad (6.5)$$

where σ_{τ_1} and σ_{τ_2} are determined from the results of the FE simulations in the following way:

$$\begin{aligned}
 \sigma_n &= \sigma_{yy}^{FE} \\
 \sigma_{\tau 1} &= \sigma_{xy}^{FE} \cos \omega + \sigma_{yz}^{FE} \sin \omega \\
 \sigma_{\tau 2} &= \sigma_{yz}^{FE} \cos \omega - \sigma_{xy}^{FE} \sin \omega
 \end{aligned} \tag{6.6}$$

For “penny-shaped” cracks, the combination of normal ($\sigma_n = \sigma_{yy}^{FE}$) and shear stresses ($\sigma_{\tau 3} = \sqrt{(\sigma_{xy}^{FE})^2 + (\sigma_{yz}^{FE})^2}$) leads to following equivalent stress:

$$\sigma_{eq} = \sqrt{\sigma_n^2 + Y_{II}^2 \sigma_{\tau 3}^2 \cos^2 \theta + \frac{H_1}{|\Gamma(2+i\varepsilon)/\Gamma(0.5+i\varepsilon)|^2 H_2} Y_{III}^2 \sigma_{\tau 3}^2 \sin^2 \theta}, \tag{6.7}$$

where Y_{II} and Y_{III} depend on the elastic properties of the joined materials (see Appendix B), $\Gamma(\varepsilon)$ is a gamma function, θ is the angle along the circumference of the crack, with respect to the direction of the shear stress. Failure is triggered by the point at which the equivalent stress has its maximum. It could be shown that the maximum of σ_{eq} for “penny-shaped” cracks is achieved for $\theta = 0$ (i.e. $\cos \theta = 1$ and $\sin \theta = 0$).

Also, in the case of “penny-shaped” cracks, the orientation problem vanishes completely. This fact allows to simplify the integration procedure in failure probability formula (6.4).

6.2 Stress analysis of interfaces

In this chapter, finite element models are generated for 2D as well as for 3D cases in order to study the stress state at the interface. The stress analysis is provided for initially uncracked components. Then, using the methods presented in chapter 4.2, the stress states at the tip of probable cracks can be determined. As a consequence, with respect to expressions (6.1), (6.5) and (6.7) for different crack models equivalent stresses are calculated as well as the mode-mixity parameters.

6.2.1 Two-dimensional finite element models

For a parametric study in 2D, the Brazilian disk specimen was chosen. The geometry of the bi-material component is shown in [Figure 6.2a](#), where the thin Al_2O_3 -layer ($E_1 = 347GPa$, $\nu_1 = 0.21$) is surrounded by $Y-ZrO_2$ material ($E_2 = 213GPa$, $\nu_2 = 0.32$). The Brazilian disk is under a diametrical compression ($F = 50kN$). The geometry was selected to take advantage of symmetry in the modelling – further, only the left interface between Alumina and Zirconia materials is considered.

Three FE models were built in order to examine the influence of the interlayer thickness ($t = 0.1mm$, $t = 1.0mm$ and $t = 3.0mm$) on the interface stress field. The analytical solution for a homogeneous Brazilian disk was taken as the limit for the infinitesimal interlayer thickness. Analytical expressions for stress components are given in [69]. The radius of the disk in every case is $R = 22.5mm$.

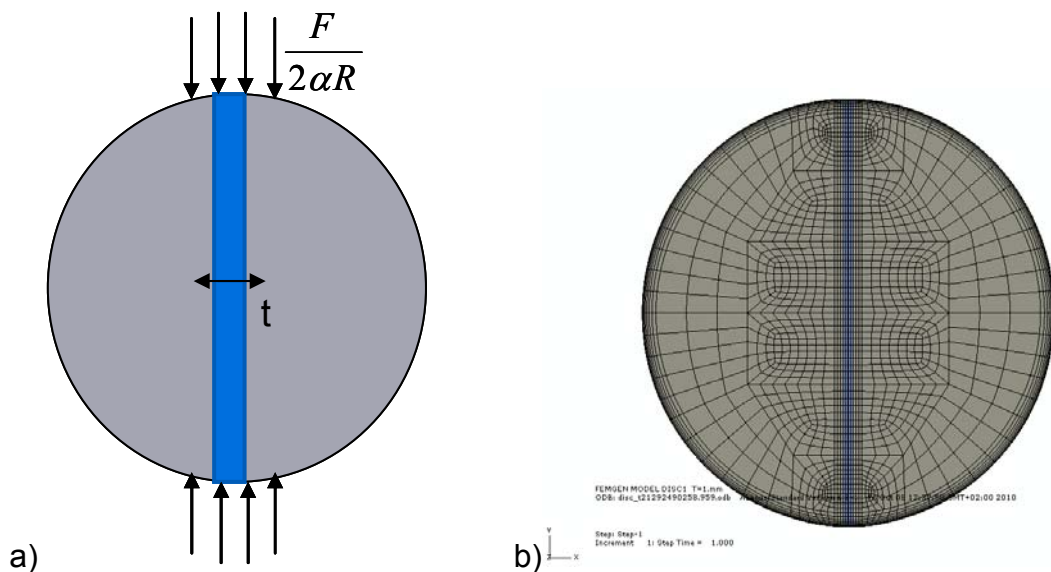


Figure 6.2 - a) Geometry of the Brazilian disk specimen; b) FE mesh for Brazilian disk bi-material component

Finite element models were built in ABAQUS [1]. The two-dimensional mesh used for Brazilian disk is shown in [Figure 6.2b](#). It contains 2,460 eight noded quadratic elements with 7,473 nodal points; 492 of those elements are lying in the interlayer.

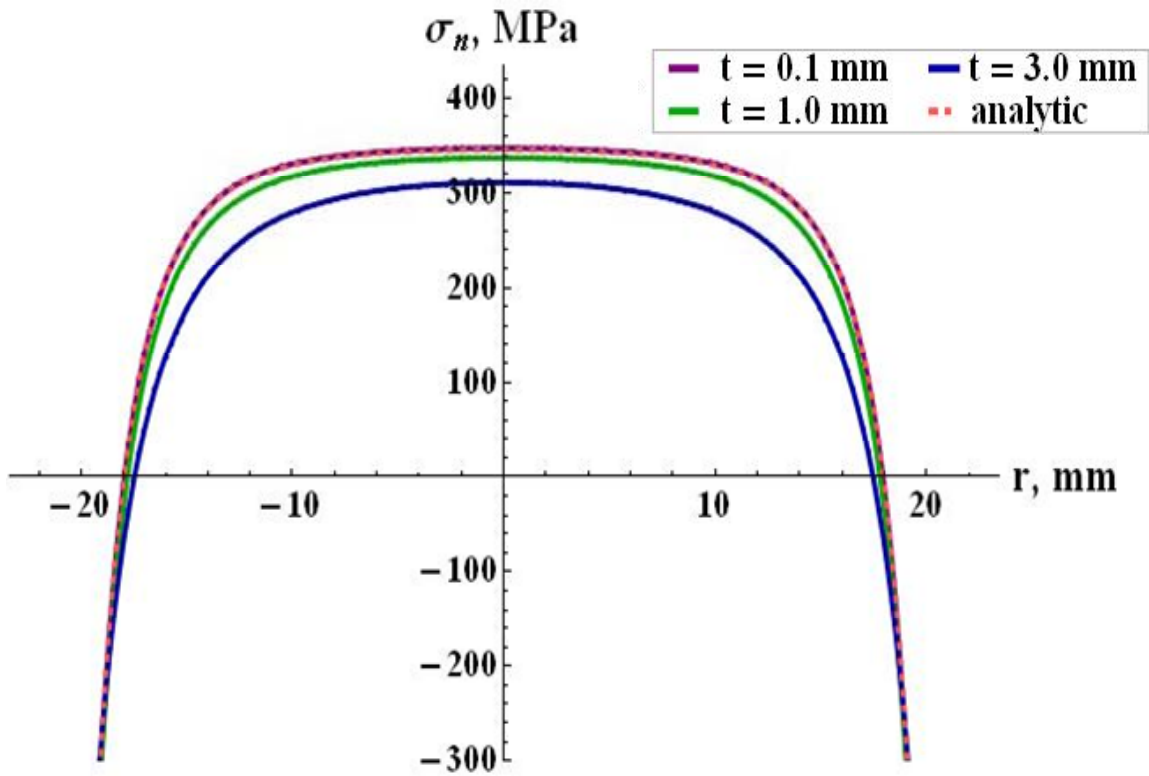


Figure 6.3 - Normal stresses at the interface of 2D Brazilian disk for the geometry shown in Figure 6.2

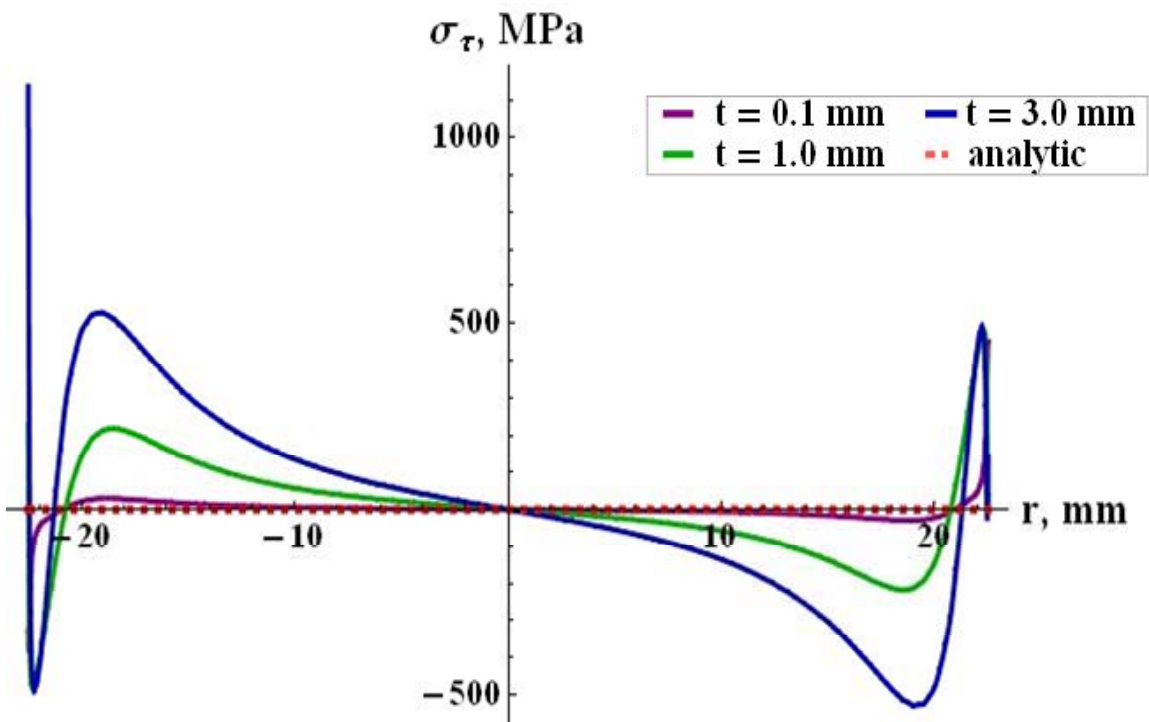


Figure 6.4 - Shear stresses on the interface of 2D Brazilian disk for the geometry shown in Figure 6.2

For the different geometries of Brazilian disk, the normal and shear stresses at the interface were calculated. [Figure 6.3](#) and [Figure 6.4](#) show the results together with the analytical solution according to [69].

The FE results compare well with the analytic solution, especially for the case of Al_2O_3 -layer with thickness $t = 0.1mm$. Apparently, with increasing inter-layer thickness the tensile stresses at the interface between the two materials decrease and more pronounced interface shear stresses occur, when the interface is shifted from the middle line. It should be noted that for the homogeneous material, a pure mode-I stress acts at the middle line, while even in the case of a very thin interlayer, the stress state at the interface has non-vanishing shear stresses (Figure 6.4).

6.2.2 Three-dimensional finite element models

For the parametric study in 3D, two different specimen geometries were considered: 4PB and Brazilian disk specimens.

The geometry of the 4PB bi-material component is shown in [Figure 6.5](#) (due to symmetry reasons (x and z are axes of symmetry) only one quarter of the specimen is considered, where the $Y-ZrO_2$ material ($E_2 = 213GPa$, $\nu_2 = 0.32$) is surrounded by a thin Al_2O_3 -layers ($E_1 = 347GPa$, $\nu_1 = 0.21$). As a FE loading history, the component was first cooled down from $950^{\circ}C$ to room temperature, in order to recreate the process of sample preparation and to study the role of thermal stresses. After cooling, the bending specimen was subject to uniform distributed force, applied to the upper role ($F = 143N$). Size parameters are the following: $x \in (0mm; 11mm)$, $z \in (0mm; 2.2mm)$ and the origin of coordinate system is chosen in the way that $y = 0$ at the interface.

Finite element models were built in ABAQUS. The three-dimensional mesh used for 4PB specimen contains 4,940 elements (1,512 elements of C3D8R type and 3,428 elements of C3D20R type) with 21,637 nodal points.

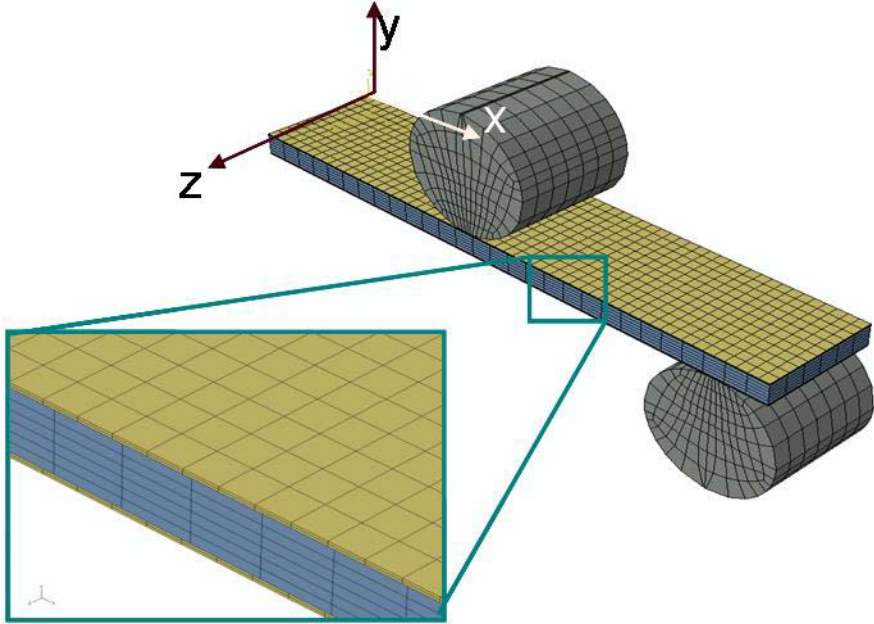
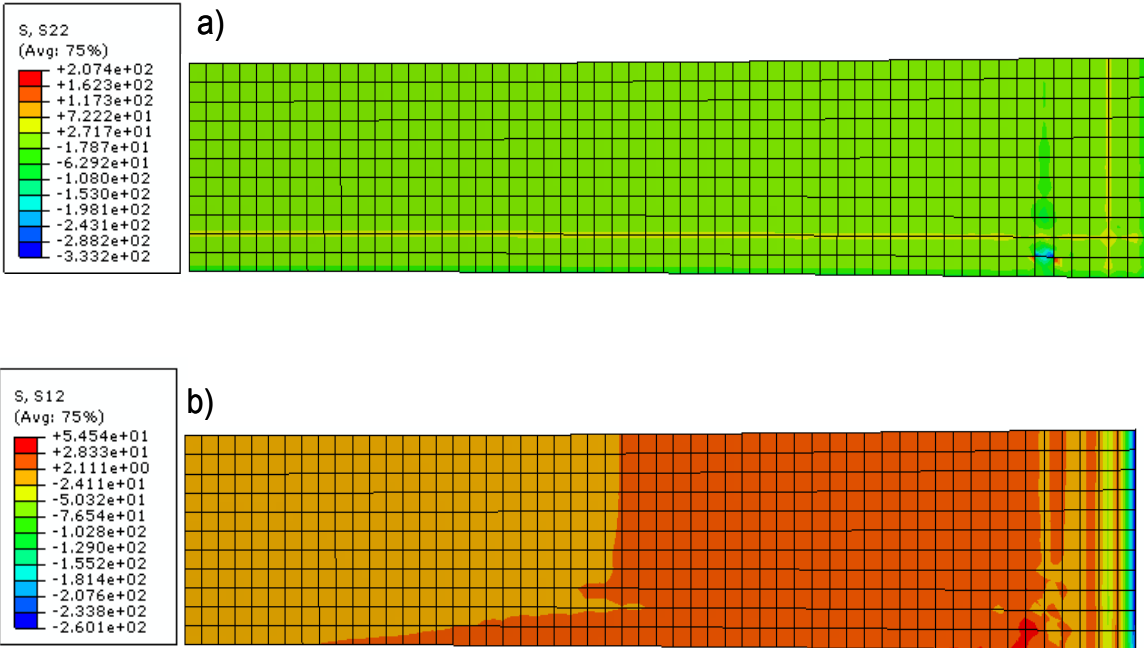


Figure 6.5 – Geometry and FE mesh for 4PB bi-material component, consisting of Zirconia surrounded by thin Alumina layers

The stresses acting at lower $Al_2O_3 - Y-ZrO_2$ interface after all thermal and mechanical loading steps are presented in Figure 6.6.



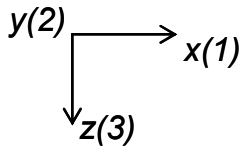
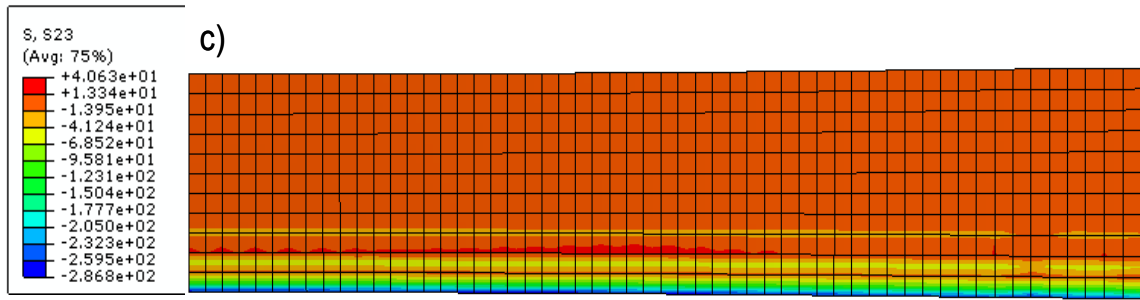


Figure 6.6 – Stress state at the interface of 4PB specimen from FE-model: a) normal stress; b) in-plane shear stress and c) out-of-plane shear stress

A second considered geometry is the Brazilian disk geometry, which is shown in Figure 6.7. Here, a diametrical Al_2O_3 -layer is surrounded by $Y-ZrO_2$. As in the 2D case, the Brazilian disk is under diametrical compression ($F = 50kN$). The load was chosen in the way to obtain interface tensile stresses of the order of material toughness values with purpose to ensure interface failure. The thickness of the interlayer is taken to be $t = 1.0mm$, the radius of the disk is $R = 22.5mm$ and the thickness of the whole component is $w = 5.0mm$.

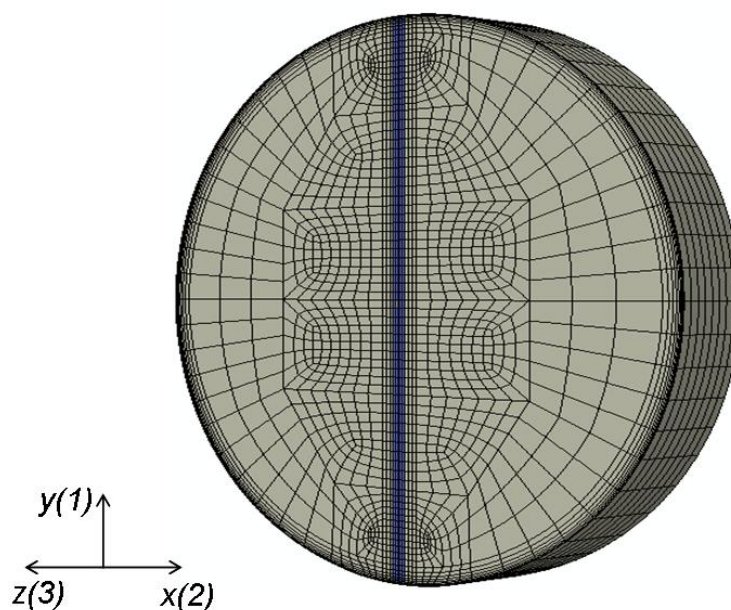


Figure 6.7 - Geometry and FE mesh for Brazilian bi-material disk

6. Numerical study and discussions

The FE-model of the Brazilian disk specimen contains 19,680 cubic elements of C3D20 type with 87,313 nodal points in total.

In Figure 6.8 the interface stress distributions on the left interface are presented.

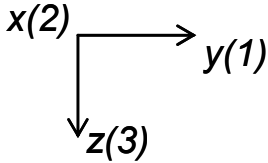
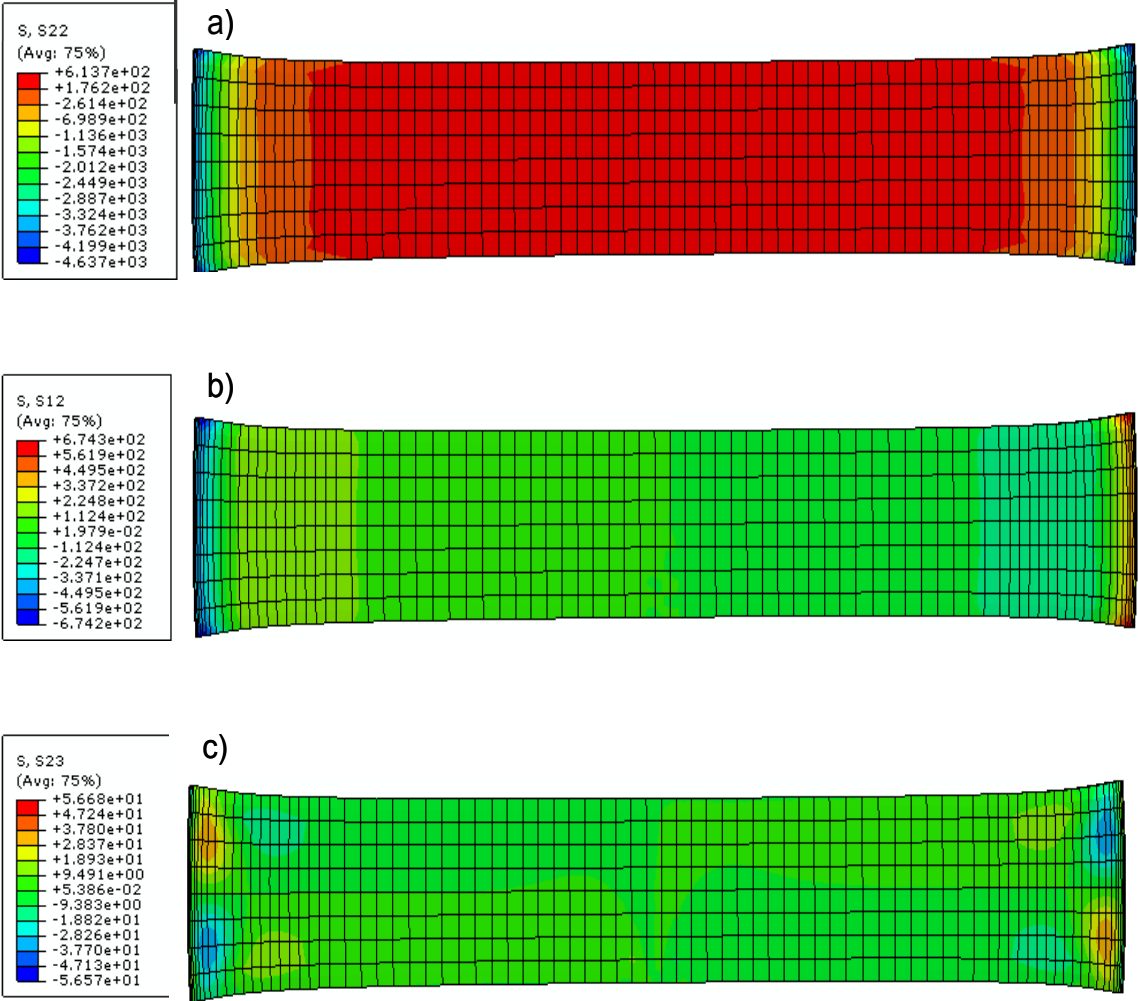


Figure 6.8 – Stress state at the interface of Brazilian disk specimen from FE-model: a) normal stress; b) in-plane shear stress and c) out-of-plane shear stress

Using the stress results obtained from FE models, the analysis of equivalent stresses and mode-mixity parameters is now possible.

6.2.3 Equivalent stress and mode-mixity parameter

In the 2D case for Brazilian disk specimen with respect to the proposed crack model (6.1), equivalent stresses are calculated along the interface (see Figure 6.9). Computation of mode-mixity parameter ψ according to (2.18) is reflected in Figure 6.10.

For the case of the homogeneous disk, where the stress state is described by the analytical solution [69], the mode-mixity parameter ψ equals zero along the middle line. With increasing thickness of the inter-layer stress will slowly change from mode-I to mixed-mode. In Figure 6.10 one can see that for Brazilian disk of type one ($t = 0.1\text{mm}$) shear effects in the centre of the specimen are weak. Whereas for Brazilian disk of third type ($t = 3.0\text{mm}$) the behaviour of mode-mixity parameter is completely different and pure mode-I stress state is achieved only at few points along the interface.

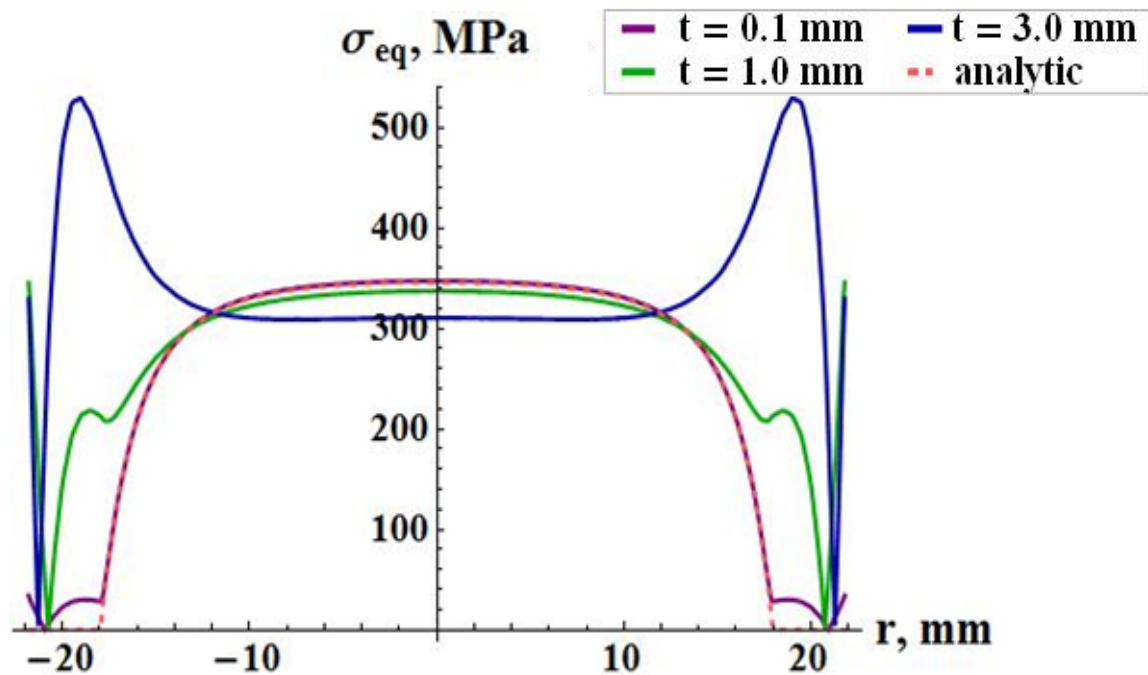


Figure 6.9 – Equivalent stresses at the interface of the Brazilian disk based on the 2D FE simulation (see Figure 6.3 and Figure 6.4)

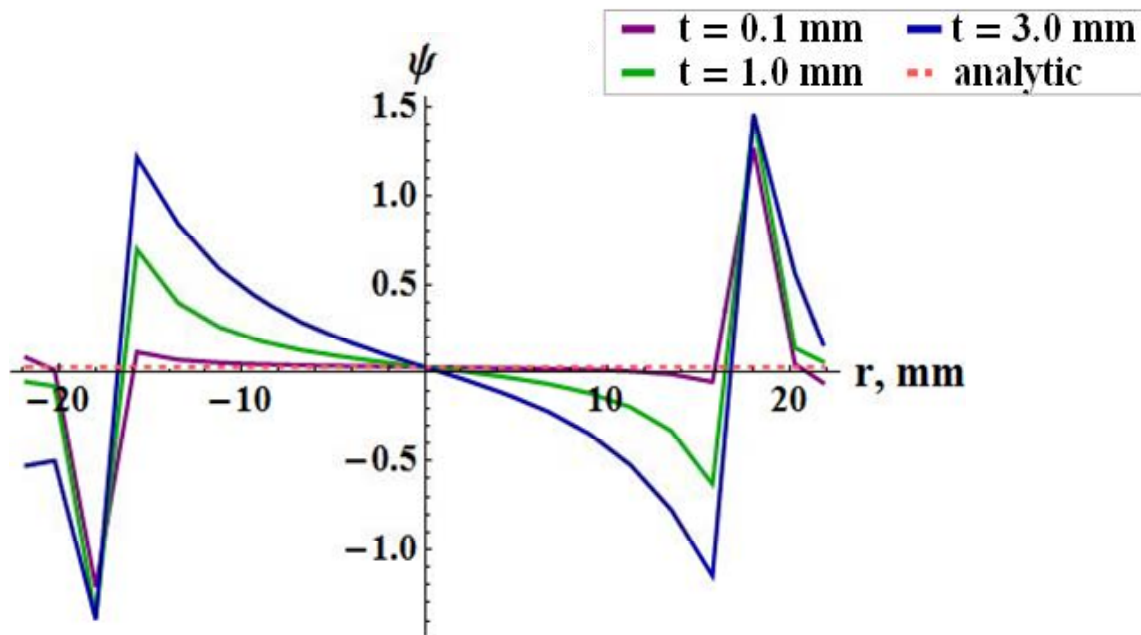


Figure 6.10 – Mode-mixity parameter at the interface of the Brazilian disk based on the 2D FE simulation (see Figure 6.3 and Figure 6.4)

With respect to the expression of failure probability (3.31) it is obvious, that the most dangerous places of interface are those, where σ_{eq} reaches the maximum value and those, where the mode-mixity parameter ψ goes to zero. For the Brazilian disk of type one ($t = 0.1mm$) and type two ($t = 1.0mm$), as well as for homogeneous material, it is most probable to have the cracks origin at the centre of the disk ($r \approx 0$), where the tensile stress has its maximum value and shear stresses are almost vanishing. In the case of a wide inter-layer ($t = 3.0mm$), when the interface is sufficiently remote from the middle line, the fracture would be expected to occur near the edges of the disk ($r \approx 17-19mm$).

In case of 3D components, equivalent stresses were calculated for two different crack models. In [Figure 6.11](#) they are shown for both geometries in the case of a “penny-shaped” crack model.

A comparison of the stress state for different crack models shows that, in the case of “penny-shaped” cracks, equivalent stresses are lower than those, obtained for “through-wall” cracks, although shear stresses have a bigger influence on “penny-shaped” cracks than on “through-wall” cracks.

Mode-mixity parameters were calculated over the whole interface as a functions of two coordinates x and z and the crack orientation angle ω . For 4PB specimen ψ - and ϕ -parameters are shown in [Figure 6.12](#).

6.2 Stress analysis of interfaces

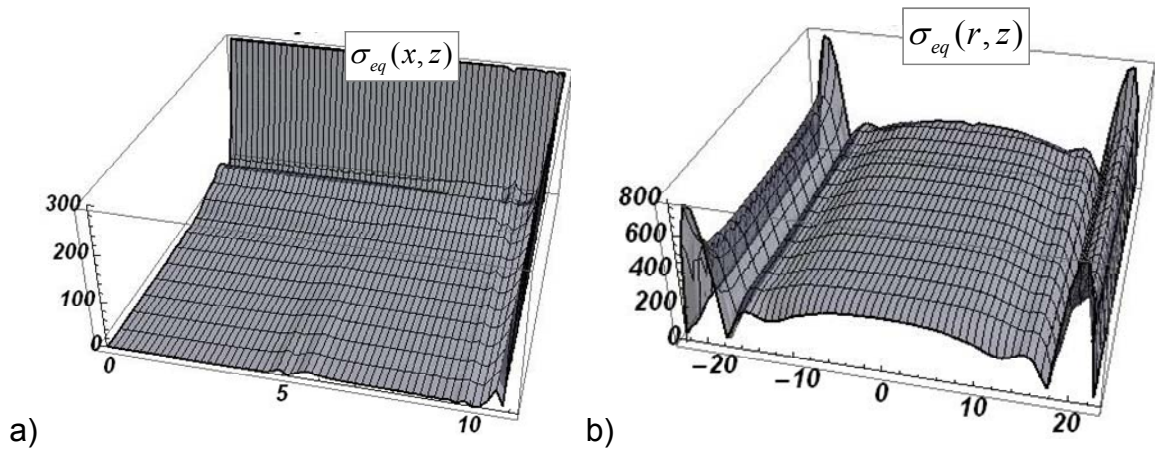


Figure 6.11 – Equivalent stresses for the “penny-shaped” crack model at the interface of: a) 3D 4PB specimen; b) 3D Brazilian disk

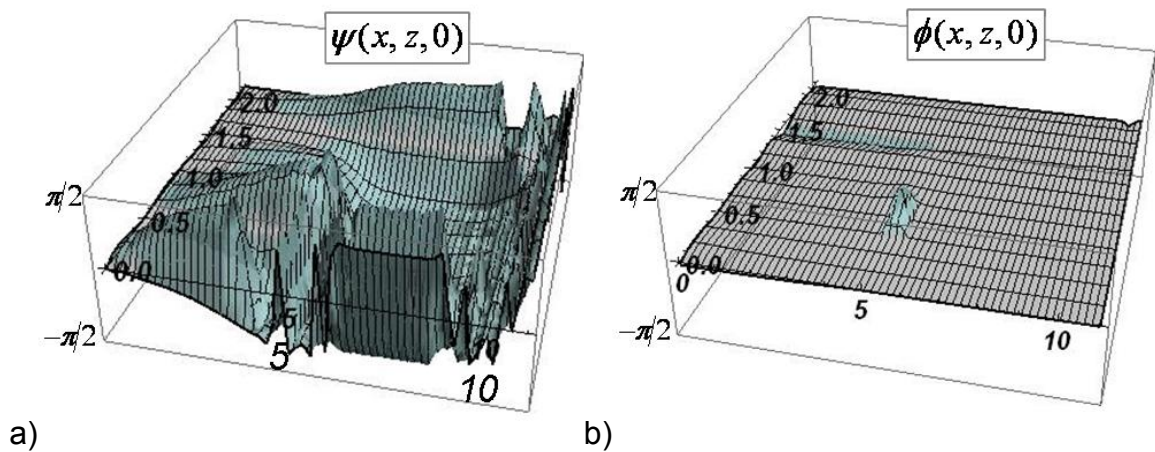


Figure 6.12 – Mode-mixity parameters at the interface of 3D 4PB specimen: a) ψ -parameter; b) ϕ -parameter (both for “through-wall” crack model)

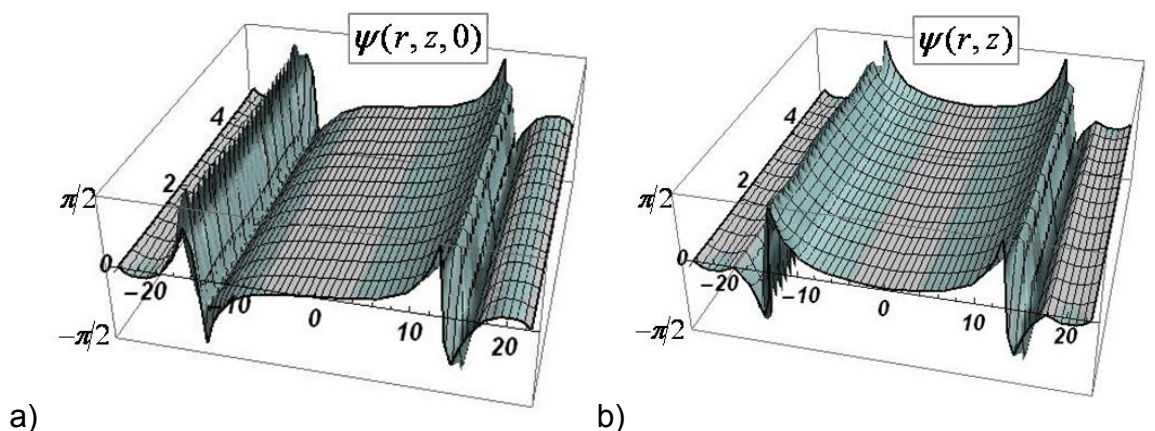


Figure 6.13 – Mode-mixity parameters ψ at the interface of 3D Brazilian disk: a) “through-wall” crack model; b) “penny-shaped” crack

Both parameters, according to their definitions (2.18) and (6.3) are laying in the interval $(-\pi/2; \pi/2)$. The oscillation of the ψ -parameter is due to the coarse mesh of FE-model, which was built with the only purpose of testing the algorithm of failure probability determination. Although it gives the relevant stress values, it is not sufficiently fine for the calculation of the mode-mixity parameter. It turned out that ψ , as an arctangent function, is sensitive even to slight changes of normal and shear stresses with respect to each other. From Figure 6.12, it is still possible to distinguish qualitatively, between a mode-I stress state (shown by grey colour) and a mixed-mode stress state (blue colour). For the ϕ -parameter regions where the out-of plane stress appears are shown in blue.

In the case of 3D Brazilian disk, the ϕ -parameter equals zero along the interface. In [Figure 6.13](#), the phase angle ψ is shown for two crack models in order to compare the results. One can see a difference, which appears due to the different determination of in-plane shear stresses for “penny-shaped” and “through-wall” cracks. Regardless of the model choice, the regions of the mode-I stress state at the centre of the disk and the adjacent mode-mixity regions are identical.

6.3 Interface failure probability results

The final step of numerical analysis is the failure probability calculation. It requires integration over the interface plane and over the crack orientation if appropriate (for example in “through-wall” crack model, where the crack orientation in the stress field plays an important role). The role of Weibull parameters as well as of mode-mixity parameters will be discussed below.

6.3.1 Parametric study

Interface failure probability P_F is calculated for the two crack models in above-considered components. The behaviour of the function $P_F = P_F(m, \sigma_0)$ is shown in [Figure 6.14](#) for the Brazilian disk problem with “penny-shaped” natural flaws. Results for other cases show qualitatively similar behaviour and they are described later in more detail. It has to be noted that the plot $P_F(m, \sigma_0)$ is

obtained for the prescribed fixed load. Large values of P_F correspond to, e.g., small values of the strength parameter σ_0 . The location of transition region is determined by the selected load level of $50kN$ applied in diametrically compressive way, which causes equivalent interface stresses stress shown in Figure 6.11b.

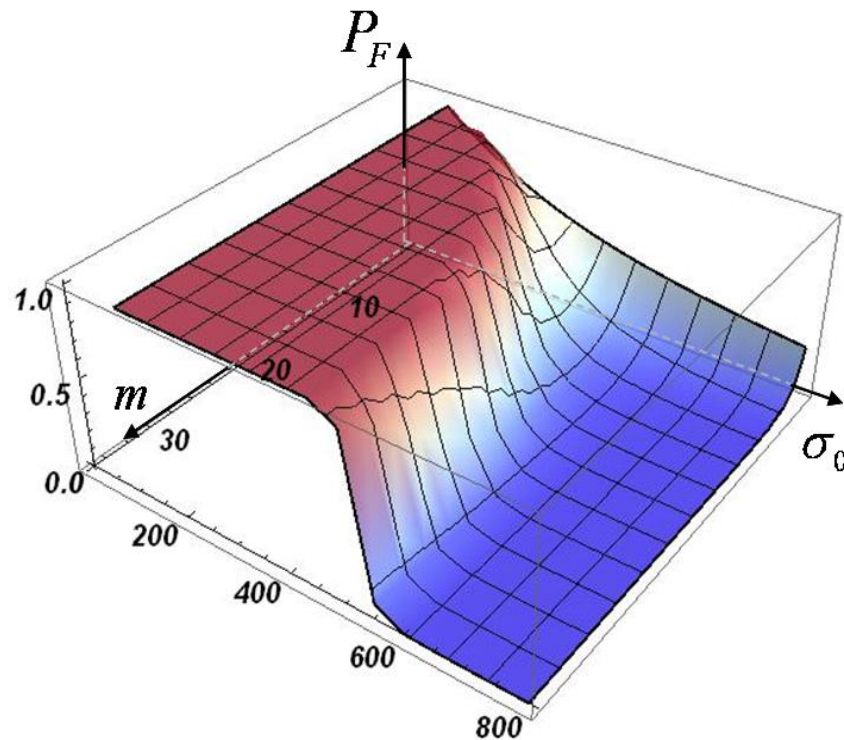


Figure 6.14 – Interface failure probability as a function of Weibull parameters for 3D Brazilian disk problem

The plot of interface failure probability exhibits three main zones. For low values of the strength parameter σ_0 and the whole range of the parameter m , failure generally occurs and P_F is 100% for the considered loading case (shown by the red plane). The opposite situation is in the case of strong interfaces – failure probability goes to zero, except for very small m -values. The third zone in the middle is the most interesting for the interpretation of the parametric study. In this transition zone, the values of the interface reliability are changing from 0% to 100%. For small values of the shape parameter m the transition is very wide, whereas for the high values of m a sharp transition is present and the transition width is only 50MPa.

6. Numerical study and discussions

This is shown more clearly in [Figure 6.15](#), where the contour plot of interface failure probability as a function of the Weibull parameters is introduced. The vertical lines correspond to the interval of Figure 5.7 based on the fractographic observation and on an assumed Weibull modulus of $m = 10$.

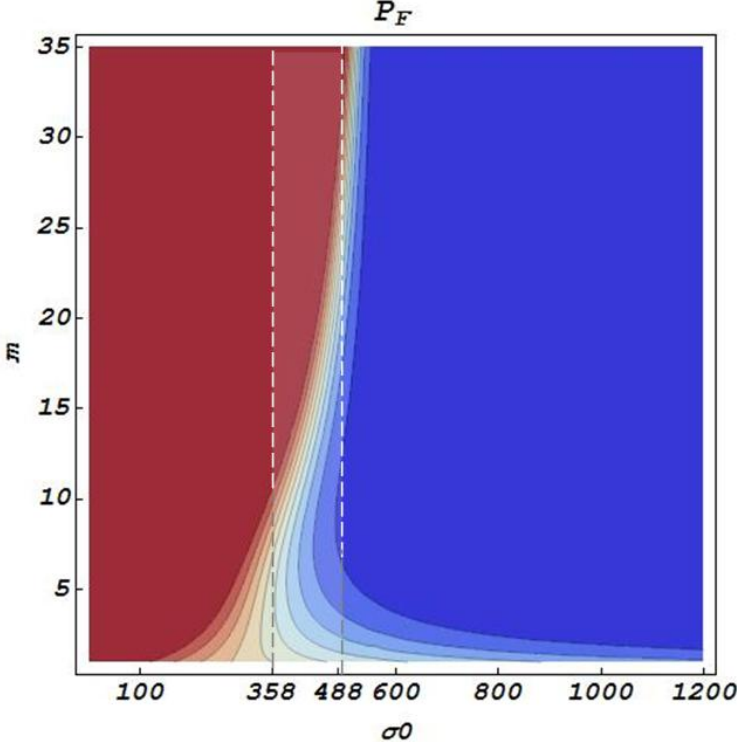


Figure 6.15 – Contour plot $P_f(m, \sigma_0)$ for 3D-Brazilian disk specimen

Table 6.1 – Interface failure probability for 4PB specimen

4PB specimen	$m = 10$		$m = 18$		$m = 25$	
	Through-wall	Penny-shaped	Through-wall	Penny-shaped	Through-wall	Penny-shaped
$\sigma_0 = 80MPa$	100.0%	100.0%	100.0%	100.0%	100.0%	100.0%
$\sigma_0 = 120MPa$	90.29%	41.30%	100.0%	100.0%	100.0%	100.0%
$\sigma_0 = 150MPa$	22.15%	5.56%	99.57%	35.90%	100.0%	93.67%
$\sigma_0 = 180MPa$	39.63%	9.20%	18.51%	1.65%	67.62%	28.52%
$\sigma_0 = 420MPa$	$\square 10^{-5} \%$	$\square 10^{-6} \%$	$\square 10^{-8} \%$	$\square 10^{-9} \%$	$\square 10^{-9} \%$	$\square 10^{-11} \%$

For a more detailed comparison of the “through-wall” and “penny-shaped” crack models the values of interface failure probability are determined for some

6.3 Interface failure probability results

combinations the of Weibull parameters. For the considered loading cases, the results are shown in [Table 6.1](#) for 3D 4PB specimen and in [Table 6.2](#) for Brazilian disk, correspondingly.

Table 6.2 – Interface failure probability for Brazilian disk specimen

Brazilian disk specimen	$m = 10$		$m = 18$		$m = 25$	
	Through-wall	Penny-shaped	Through-wall	Penny-shaped	Through-wall	Penny-shaped
$\sigma_0 = 380MPa$	84.50%	64.98%	100.0%	100.0%	100.0%	100.0%
$\sigma_0 = 420MPa$	49.61%	32.00%	99.84%	98.32%	100.0%	100.0%
$\sigma_0 = 480MPa$	16.50%	9.65%	44.06%	30.89%	89.69%	77.11%
$\sigma_0 = 550MPa$	4.52%	2.57%	4.89%	3.14%	7.28%	4.79%
$\sigma_0 = 720MPa$	0.31%	0.17%	0.04%	0.02%	0.009%	0.006%

For both geometries we can observe the decreasing numerical values for the interface failure probability with increasing interface strength σ_0 . The dependence of the failure probability function on m is more complex and accounts the position of strength parameter σ_0 with respect to the transition zone. For low σ_0 -values, in the beginning of transition zone, the numerical values of failure probability are growing with increasing parameter m . When σ_0 belongs to the centre of transition zone, P_F first decreases and then increase with increasing m (see e.g. line $\sigma_0 = 180MPa$ in Table 6.1). For σ_0 at the end of the transition zone, the failure probability decreases with increasing m , what is shown for $\sigma_0 = 420MPa$ in Table 6.1 and $\sigma_0 = 720MPa$ in Table 6.2. This behaviour is observed until σ_0 is high enough that for any m -value the probability of interface failure vanishes ($P_F = 0$).

It can be also seen that the reliability of components with “penny-shaped” approach is higher than for the same components with “through-wall” cracks. This is a direct consequence of the fact, that stress concentrations around circular flaws are less pronounced than those at the tips of elliptical cracks or “through-wall” cracks [23].

6. Numerical study and discussions

In [Figure 6.16](#) the influence of the crack model on the failure probability as function of material strength is shown for two selected m -values. The purple lines indicate the penny-shaped crack model and the blue lines represent the through-wall crack model. Numerical results correspond again to the reference loading case of the Brazilian disk. Very high and low values of parameter σ_0 lead to the same values of P_F or the difference between different mechanical approaches is negligibly small. In an intermediate range of the Weibull parameter σ_0 , where the numerical value of failure probability is sensitive to the choice of the crack model (e.g. for $\sigma_0 = 400MPa$ difference in P_F between “trough-wall” and “penny-shaped” cracks is about 20%, while for $\sigma_0 = 500MPa$ it is just 0.04%).

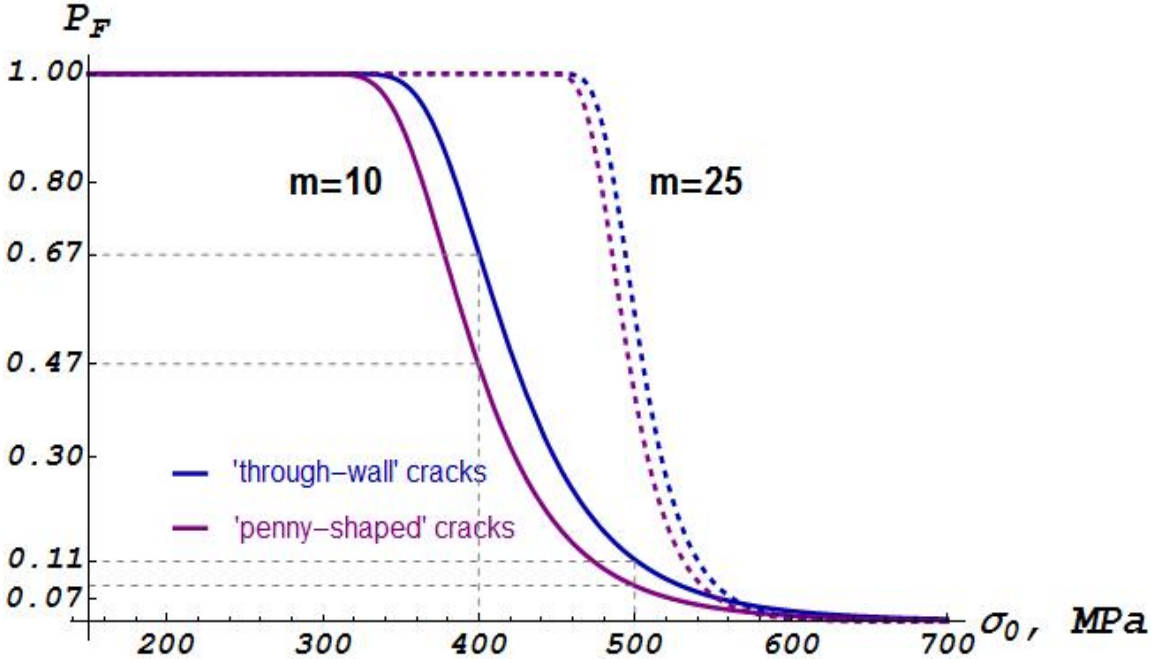


Figure 6.16 – Comparison of the interface failure probability for different crack models by example of reference loading case of Brazilian disk

An important result of this chapter is that the algorithm for calculating the failure probability for three-dimensional problems works consistently. This algorithm allows to use different crack models, e.g. through-wall and penny-shaped cracks which were discussed before. The influence of Weibull parameters on the failure probability can be studied for any reference loading case and any specimen’s geometry. The interpretation of results regarding the

discussion about possible specimen configurations in future experiments is introduced in chapter 6.4.

6.3.2 Role of the mode-mixity parameter

On the basis of stress analysis for 2D Brazilian disk specimens (chapter 6.2.1), the interface failure probability was calculated for all four component geometries. Numerical results for three selected (m, σ_0) -combinations are introduced in Table 6.3 with the purpose to evaluate the role of the mode-mixity parameter ψ . Therefore, for each pair of Weibull parameters values of failure probability are compared according to the exact and the conservative approaches (see chapter 4.3), where the conservative model [50] gives the upper critical value of the failure probability, which is achieved for $\psi = 0$ along the interface.

Table 6.3 – Interface failure probability: comparison of the exact and conservative ($\psi = 0$) approach

	$m = 10, \sigma_0 = 320MPa$		$m = 10, \sigma_0 = 430MPa$		$m = 18, \sigma_0 = 380MPa$	
	exact	conservative	exact	conservative	exact	conservative
Analytical	63.26%	63.26%	5.08%	5.08%	6.95%	6.95%
$t = 0.1mm$	64.75%	64.99%	5.29%	5.32%	7.47%	7.55%
$t = 1.0mm$	69.26%	71.77%	5.96%	6.38%	12.6%	13.22%
$t = 3.0mm$	61.89%	100.0%	4.90%	69.05%	10.49%	100%

For loading cases, where the role of shear stresses is small, the difference between the two approaches is less than the hundredth part of a percent. Even for moderate variations of shear stresses ($t = 1.0mm$), the dependence of the P_F on ψ -parameter is not strong. It should be noted that in this particular loading case, the normal stresses still dominate the shear stresses. However, for the example of the Brazilian disk with an interlayer $t = 3.0mm$, where shear stresses are high (see Figure 6.4) and normal stresses become lower (see Figure 6.3), the interface is subjected to the stress state, which is different from mode-I (see Figure 6.10), and one can see that the difference between the exact and the conservative approaches is large.

Another tendency can be noticed - interface failure probability increases with moving the interface away from the middle line for any material combination. This behaviour is observed until a certain value of the interlayer thickness is reached. Then, the values of the failure probability decrease slowly. This observation is explained by the influence of two counteracting factors: first, increasing of shear stresses from zero in the case of the homogeneous disk to much more higher values in the case of interlayer with thickness $t = 3.0mm$, as it is shown in the Figure 6.4, leads to the increasing of the equivalent stresses and causes higher failure probability. On the other hand, the normal stresses (see Figure 6.3) decrease.

6.4 Discussion

By the example of a 2D Brazilian disk model, the contribution of the mode-mixity parameter ψ to the determination of interface failure probability was considered. A conservative solution, assuming pure mode-I stress state acting at the interface, allows to reduce possible error in failure probability calculation similar to use of additional safety factors in failure analysis. But on the other hand, as it was shown by the example of the disk with interface slightly away from the middle line, it is possible to overestimate the failure probability.

A comparison of the interface failure probability values for 2D as well as for 3D Brazilian disk models (see Table 6.2 and Table 6.3) shows a deviation in failure probability values at nominal equal load. In [Figure 6.17](#) failure probability is plotted as a function of the strength parameter σ_0 and for a constant value of $m = 10$. The difference can be mostly attributed to effects of load application modelling in studied examples. In the case of 3D component, the failure probability is sensitive to stress concentrations which appear in the region of applied load. In [Figure 6.18](#) the local failure probability is shown. It is regarded as the failure probability density function with respect to the surface or volume. Thus, the stresses acting at the edges of 3D specimen (see Figure 6.18b) cause very high failure probability comparing with stresses acting near the middle line and close to the material interface. Since the calculations are performed with the aim of establishing the methodology for the failure probability calculations, no

refinement of the load application way was done for 3D model. In 2D case the applied compressive load was distributed over the circular arc of 15° .

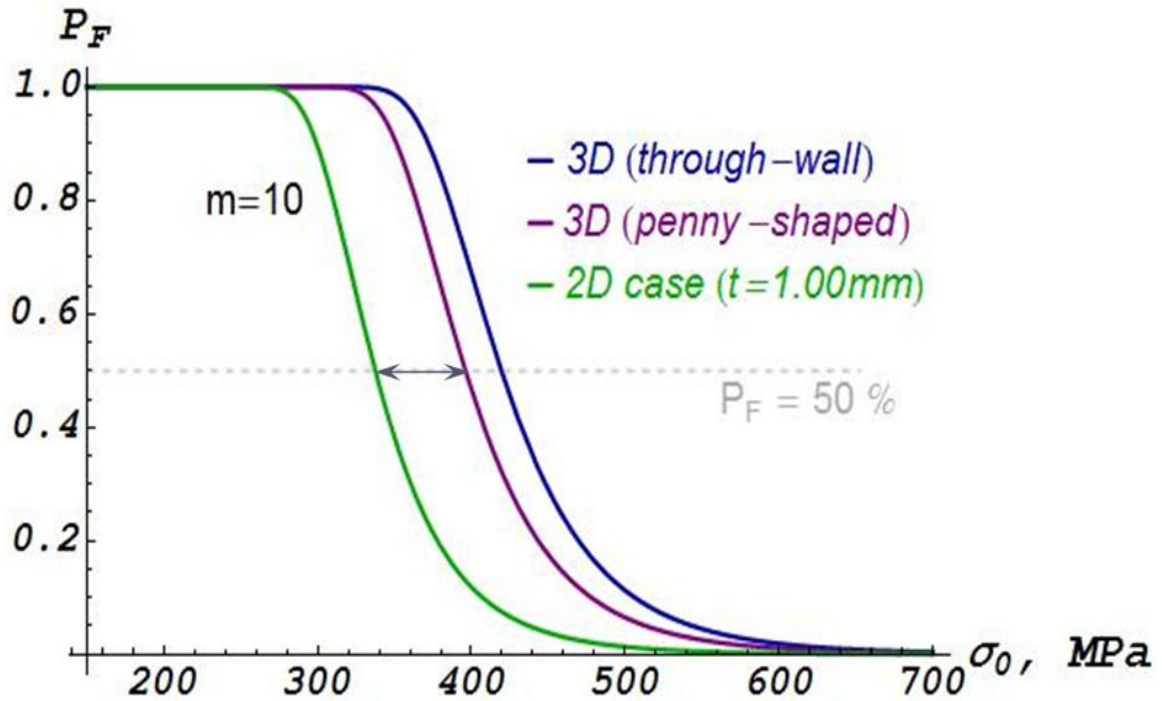


Figure 6.17 – Comparison of 2D and 3D models: interface failure probability of Brazilian disk with radius $R = 22.5\text{mm}$

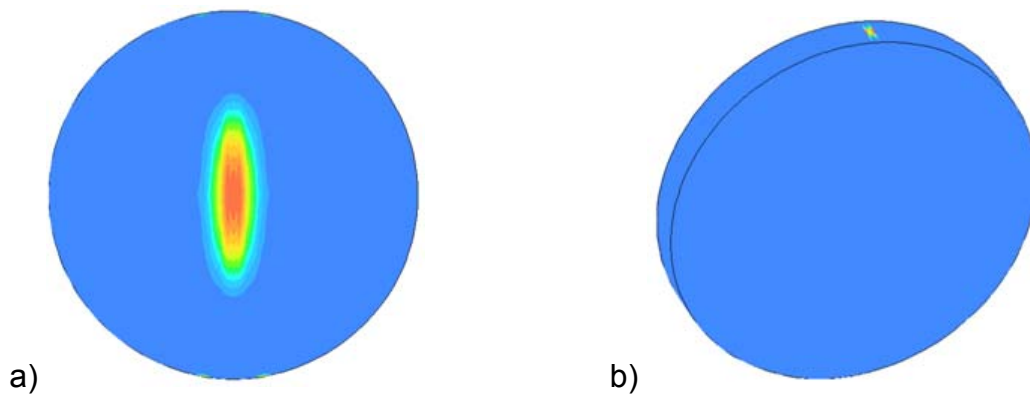


Figure 6.18 – Local risk of failure for Brazilian disk specimen: a) 2D model; b) 3D-model

Figure 6.19 proves that the difference between 2D and 3D models appears mainly due to the stress concentrations at the point of applied loading. Interface failure probability was calculated for different lengths of the central part of the interface. Strength parameters σ_0 , corresponding to a failure probability of 50%, were taken as representative values and shown in Figure 6.19 (see arrows in Figure 6.17 and Figure 6.19). Results of this analysis allow to compare 2D (green curve) and 3D (purple curve) approaches for failure probability calculations, excluding the effects appearing on the edges of the disk. One can see, that already at a distance of 4.5mm from the points of applied force ($r = 36\text{mm}$) both models are in good agreement. The difference in the interface strength values obtained from 2D and 3D (“penny-shaped” crack) models is 6MPa only and it vanishes with moving away from the disk edges.

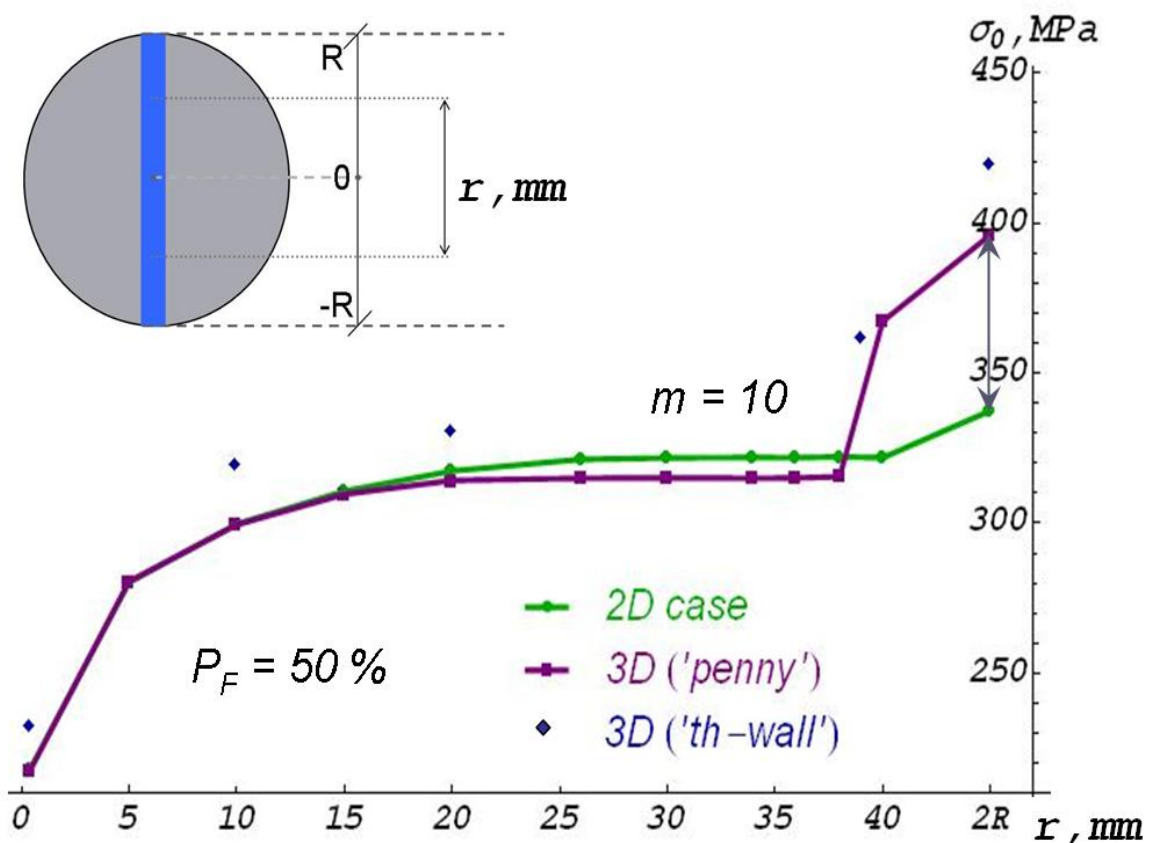


Figure 6.19 – Comparison of 2D and 3D (“penny-shaped”) models: strength of the Alumina-Zirconia interface, corresponding to a failure probability of 50% ($P_F = 0.5$), for reference loading case of Brazilian disk

The Brazilian disk component configurations are recommended to experiments in order to obtain sufficient statistical strength data. By putting the interface close to the middle line the interface failure appears to be high (see Figure 6.18a). On the other hand, the combination of interface strength parameters has to be sufficient to ensure specimen cracking in the middle of the disk, where homogeneous Alumina material ($m=15$, $\sigma_0=347\text{MPa}$) is located. Calculations of the volume failure probability for the considered loading case of the Brazilian disk were carried out in STAU. Failure probability of the homogeneous Al_2O_3 bulk material is 12%, while for the interface with the same values of Weibull parameters, interface failure probability reaches 44%. This is the indication that the described Brazilian disk configuration is suitable for interface strength testing. The role of the thickness of the interlayer, respectively the role of the distance between the interface and the middle line has already been discussed in chapter 6.3.2. However, it is important to account for contact stresses which may govern the failure in a Brazilian disk test. Thus, the load concentration effects have to be eliminated in experimental settings.

With the results of this work, the implementation of modified Weibull theory into the existing version of STAU is possible. It should be noted that the calculation of the interface failure probability based on the “penny-shaped” crack model is less resource-intensive than it is for the “through-wall” crack model. The final choice of the crack model has, however, to be done in agreement with the experimental observations of the interface crack shape. The “penny-shaped” crack model is probably more appropriate to describe the form of natural defects.

In this chapter, the influence of different parameters on the interface failure probability was studied. The role of Weibull modulus and interface mode-mixity stress state as well as the component geometries and two different crack models were examined.

7. Summary

In the present work, a framework for the probabilistic description of brittle failure of interfaces in bi-material ceramic joints was developed. The results were applied to assess the sensitivity of failure probability with respect to Weibull parameters and mixed-mode parameter on the basis of limited data for strength measurements. Using two different specimen geometries, the method was tested and hints towards future experiments were obtained.

To assess the interface failure probability, the Weibull theory used for brittle ceramic materials needed some modification – to take properly interface stress states into account. The extension of the classical probabilistic model is based on the weakest-link approach and requires a suitable fracture mechanics model to describe the conditions of an interface crack propagation, especially to cope with the oscillating mixed-mode character of the stress field at the tip of interface crack. An energy release fracture criterion was chosen for this purpose. Assigning this approach to combine probabilistic and fracture mechanics methods, the Weibull failure relations for brittle interfaces in bi-material joints were derived. A mode-mixity parameter, ψ , occurs in the generalized expression for the failure probability. The impact of this term was investigated by a decomposition of the general interface problem into two auxiliary mechanical problems, for which analytical solutions are possible.

The solution algorithm for the stress state on the interface is built on the evaluation of singular integral equations and complex variable method, and was numerically presented for the problem of an interface crack in a finite bi-material strip under remote uniform tensile and shear loading. The results obtained can be used for a general treatment of the weakest-link interface failure probability where the remote stresses for the boundary conditions are obtained from a Finite Element stress analysis of the whole component under consideration. Neglecting

7. Summary

the mode-mixity parameter ψ in the obtained solution leads to a conservative assessment of the failure probability for interface cracks in a gradually varying remote stress field. On the other hand, in this work it was explicitly shown that this conservative approach for failure probability determination can result in an appreciable overestimation for some loading combinations.

The calculations of component's reliability are normally based on the experimental characterization of the material strength parameters by some reference geometrical and loading configurations. However, interface strength data for natural interface cracks were not available. From experiments carried out elsewhere only a limited amount of data could be used to calibrate the model.

Special attention was, therefore, devoted to a numerical parametric study, with the purpose to compensate the insufficiency of statistical interface strength data. The main purpose of this approach, provided to verify the suggested method of failure probability determination, was to investigate the sensitivity of interface reliability with respect to variations of the Weibull parameters. The behaviour of the failure probability with respect to the interface strength parameter shows a transition zone between regions of high and of very low failure probability, respectively, whose width was essentially given by the second parameter of the Weibull distribution. The shape of the transition zone was also studied and quantitatively described for some reference loading cases by the examples of 4PB and Brazilian disk specimens.

An important contribution to the characterization of interface failure consists of the description and investigation of two different crack models for the fracture mechanics approach, which are probably appropriate for the form of natural flaws at the interface. A comparison of "through-wall" and "penny-shaped" crack models regarding the numerical values of the interface failure probability shows only qualitatively consistency of the results. Quantitatively, it was observed that the presence of "through-wall" natural flaws causes higher stress concentrations and as a consequence higher failure probability for the same reference remote loading case. Also, it was revealed that the calculation of interface failure probability based on the "penny-shaped" crack model is less resource-intensive.

The importance of the numerical study provided in this work relates to the planning of future experiments and in the ability to give the necessary

interpretation of test results. At the same time, this work presents an adequate algorithm which allows prediction of the brittle failure, caused by unstable propagation of interface natural cracks. As soon as experimental interface strength data are available, this algorithm tested by simple two- and three-dimensional bi-material geometries, can be used for any real application, e.g. Lambda-sensors. The proposed algorithm can be extended for the case of cyclic mechanical loading or complex thermal and electromagnetic loading conditions.

Finally, the method of interface failure probability calculation for bi-material ceramic joints under remote multiaxial stress field developed in this work is ready to be implemented in an updated version of the existing finite-element postprocessing program STAU. This provides an opportunity to a wide range of industrial applications related to using or manufacturing ceramic components with brittle interfaces, to improve the reliable operation of the products.

Reference list

- [1] ABAQUS. Analysis User's Manual, Version 6.7. 2007.
- [2] Abramowitz, M., Stegun, I.: Handbook of mathematical functions: with formulas, graphs and mathematical tables. Applied Mathematics Series (55), Chapter 8: pp.331-341, Dover, New York, 1964.
- [3] Allwood, J., Ashby, M., Gutowski, T., Worrell, E.: Material efficiency: a white paper. *Resources, Conservation and Recycling* 55, pp. 362–381, 2011.
- [4] Banks-Sills, L.: Weight functions for interface cracks. *International Journal of Fracture* 60(1), pp. 89–95, 1993.
- [5] Banks-Sills, L., Ashkenazi, D.: A note on fracture criteria for interface fracture. *International Journal of Fracture* 103(2), pp. 177–188, 2000.
- [6] Banks-Sills, L., Konovalov, N., Fliesher, A.: Comparison of two- and three-dimensional analyses of interface fracture data obtained from Brazilian disk specimens. *International Journal of Structural Integrity* 1(1), pp. 20–42, 2010.
- [7] Banks-Sills, L., Schwartz, J.: Fracture testing of Brazilian disk sandwich specimens. *International Journal of Fracture* 118(3), pp. 191–209, 2002.
- [8] Banks-Sills, L., Travitzky, N., Ashkenazi, D.: Interface fracture properties of a bimaterial ceramic composite. *Mechanics of Materials* 32(12), pp. 711–722, 2000.

- [9] Batdorf, S.B., Heinisch, H.L.: Weakest link theory reformulated for arbitrary fracture criterion. *Journal of the American Ceramic Society* 61(7-8), pp. 355–358, 1978.
- [10] Benard, A., Bos-Levenbach, E.C.: Het uitzetten van waarnemingen op waarschijnlijkheids-papier (The plotting of observations on probability paper). *Statististica Neerlandica* 7, pp. 163–173, 1953.
- [11] Beremin, F.M., Pineau, A., Mudry, F., Devaux, J.C., D'Escatha, Y., Ledermann, P.: A local criterion for cleavage fracture of a nuclear pressure vessel steel. *Metallurgical and Materials Transactions A* 14(11), pp. 2277–2287, 1983.
- [12] Bogy, D.B., Wang, K.C.: Stress singularities at interface corners in bonded dissimilar isotropic elastic materials. *International Journal of Solids and Structures* 7(8), pp. 993–1005, 1971.
- [13] Bosch GmbH: Design of lambda sensor. online: www.bosch-lambdasonde.de/en/lambdasonde_aufbau.htm, accessed 07.02.2011.
- [14] Brückner-Foit, A., Heger, A., Heiermann, K., Hülsmeier, P., Mahler, A., Mann, A., Ziegler, C.: STAU 5 – user's manual – a post processor for a finite element program to calculate the failure probability under thermal shock loading. Institut für Materialforschung II, Karlsruhe, 2005.
- [15] Brückner-Foit, A., Hülsmeier, P., Sckuhr, M., Riesch-Oppermann, H.: Limitations of the Weibull theory in stress fields with pronounced stress gradients. Proceedings of the 45th ASME Gas Turbine and Aeroengine Conference: ASME TURBO EXPO LAND, SEA & AIR 2000, Munich, Germany, 8-11 May 2000.
- [16] Charalambides, M., Kinloch, A., Wang, Y., Williams, J.G.: On the analysis of mixed-mode failure. *International Journal of Fracture* 54(3), pp. 269–291, 1992.
- [17] Comninou, M.: An overview of interface cracks. *Engineering Fracture Mechanics* 37(1), pp. 197–208, 1990.

-
- [18] Comninou, M., Dundurs, J.: A closed crack tip terminating at an interface. *Journal of Applied Mechanics* 46, pp. 97–100, 1979.
- [19] Comninou, M.: The interface crack. *Journal of Applied Mechanics* 44(4), pp. 631–636, 1977.
- [20] Cotterell, B., Rice, J.: Slightly curved or kinked cracks. *International Journal of Fracture* 16(2), pp. 155–169, 1980.
- [21] Dundurs, J.: Effect of elastic constants on stress in a composite under plane deformation. *Journal of Composite Materials* 1(3), pp. 310–322, 1967.
- [22] Dundurs, J.: Discussion: "Edge-bonded dissimilar orthogonal elastic wedges under normal and shear loading" by D. B. Bogy. *Journal of Applied Mechanics* 36, pp. 650–652, 1969.
- [23] Engelder, T.: Continental Tectonics, Pergamon Press, Oxford, chapter 3: Brittle crack propagation, pp. 43–52, 1994.
- [24] England, A.H.: A crack between dissimilar media. *Journal of Applied Mechanics, Trans. ASME* 32, pp. 400–402, 1965.
- [25] Erdogan, F.: Stress distributions in bonded dissimilar materials with cracks. *Journal of Applied Mechanics, Trans. ASME* 32, pp. 403–410, 1965.
- [26] Evans, A.G.: A general approach for the statistical analysis of multiaxial fracture. *Journal of the American Ceramic Society* 61(7-8), pp. 302–308, 1978.
- [27] Fenner, D.N.: Stress singularities in composite materials with an arbitrarily oriented crack meeting an interface. *International Journal of Fracture* 12(5), pp. 705–721, 1976.
- [28] Gorbatikh, L.: On elastic compliances of interfacial cracks. *International Journal of Fracture* 127(2), pp. L141–L148, 2004.

- [29] Govorukha, V., Loboda, V.: On the boundary integral equations approach to a semi-infinite strip investigation. *Acta Mechanica* 128(1-2), pp. 105–115, 1998.
- [30] Griffith, A.A.: The phenomena of rupture and flow in solids. *Philosophical Transactions of the Royal Society of London A* 221, p. 163–198, 1921.
- [31] Gumbel, E.: Statistics of Extremes. Chapter 4: pp. 113-155, Columbia University Press, 1958.
- [32] Hbaieb, K., McMeeking, R., Lange, F.: Crack bifurcation in laminar ceramics having large compressive stress. *International Journal of Solids and Structures* 44(10), pp. 3328–3343, 2007.
- [33] He, M.Y., Hutchinson, J.W.: Kinking of a crack out of an interface: tabulated solution coefficients. *Technical Report MECH-113*, Harvard University, 1989.
- [34] He, M., Hutchinson, J.W.: Crack deflection at an interface between dissimilar elastic materials. *International Journal of Solids and Structures* 25(9), pp. 1053–1067, 1989.
- [35] He, M., Hutchinson, J.W.: Kinking of a crack out of an interface. *Journal of Applied Mechanics* 56(2), pp. 270–278, 1989.
- [36] Heger, A., Brückner-Foit, A., Munz, D.: STAU — ein Programm zur Berechnung der Ausfallwahrscheinlichkeit mehrachsiger beanspruchter keramischer Komponenten als Post-Prozessor für Finite-Elemente-Programme. *Technical report*, Institute for Reliability and Failure Analysis, University of Karlsruhe, Germany, 1991.
- [37] Herrmann, K.P., Loboda, V.V.: Special approach for the determination of fracture mechanical parameters at an interface crack tip. *Archive of Applied Mechanics* 68(3-4), pp. 227–236, 1998.
- [38] Hills, D.A., Barber, J.R.: Interface cracks. *International Journal of Mechanical Sciences* 35(1), pp. 22–37, 1993.

-
- [39] Härtelt, M.: Probabilistische Lebensdauervorhersage für keramische Bauteile unter komplexer zyklischer Beanspruchung. Ph.D. thesis, Karlsruher Institut für Technologie (KIT), 2009.
- [40] Hutchinson, J.W., Suo, Z.: Mixed mode cracking in layered materials. *Advances in applied mechanics*, volume 29, Elsevier, pp. 63–191, 1991.
- [41] Lazarus, V., Leblond, J.B.: Three-dimensional crack-face weight functions for the semi-infinite interface crack—I: variation of the stress intensity factors due to some small perturbation of the crack front. *Journal of the Mechanics and Physics of Solids* 46(3), pp. 489–511, 1998.
- [42] Löbel, G., Zeilinger, H., Deska, R.: Theoretische Grundlagen für die Anwendung der Bruchmechanik auf Faserverbundwerkstoffe. *Materialwissenschaft und Werkstofftechnik* 15(8), pp. 277–287, 1984.
- [43] Lin, T., Evans, A.G., Ritchie, R.O.: A statistical model of brittle fracture by transgranular cleavage. *Journal of the Mechanics and Physics of Solids* 34(5), pp. 477–497, 1986.
- [44] Loboda, V.V.: The problem of an orthotropic semi-infinite strip with a crack along the fixed end. *Engineering Fracture Mechanics* 55(1), pp. 7–17, 1996.
- [45] Loboda, V.V., Tauchert, T.R.: Stresses in an orthotropic semi-infinite strip due to edge loads. *Acta Mechanica* 55(1-2), pp. 51–68, 1985.
- [46] Lube, T.: Mechanical properties of ceramic laminates. *Key Engineering Materials* 333, pp. 87–96, 2007.
- [47] Mak, A.F., Keer, L.M., Chen, S.H., Lewis, J.L.: A no-slip interface crack. *Journal of Applied Mechanics* 47(2), pp. 347–350, 1980.
- [48] Malyshev, B., Salganik, R.: The strength of adhesive joints using the theory of cracks. *International Journal of Fracture Mechanics* 1(2), pp. 114–118, 1965.

- [49] Matsuo, Y.: Probabilistic analysis of the brittle fracture loci under biaxial stress state. *Bulletin of JSME* 24, pp. 290–294, 1981.
- [50] Melikayeva, I., Riesch-Oppermann, H., Govorukha, V.B., Kraft, O.: A generalized Weibull approach to interface failure in bi-material ceramic joints. *Archive of Applied Mechanics* (published online), DOI: 10.1007/s00419-010-0503-y, 08.01.2011.
- [51] Melikayeva, I., Riesch-Oppermann, H., Kraft, O.: Generalization of Weibull theory for interface failure in bi-material ceramic joints. Proc. of the 18th European Conference on Fracture, Dresden, 30 August - 3 September, on CD-ROM, 2010.
- [52] Mikhlin, S.G.: Singular integral equations (rus). *Uspekhi Mat. Nauk* 3(25), pp. 29–112, 1948.
- [53] Munz, D., Fett, T.: Ceramics: mechanical properties, failure behaviour, materials selection. Springer-Verlag Berlin Heidelberg, 1999.
- [54] Muskhelishvili, N.I.: Singuläre Integralgleichungen (Singular Integral Equations). Chapter 2, § 45: pp. 172-177, Akademie-Verlag, Berlin, 1965.
- [55] Muskhelishvili, N.I.: Nekotorye osnovnye zadachi matematicheskoy teorii uprogosti (Some Basic Problems of the Mathematical Theory of Elasticity). Chapter 2 (II), §41: pp. 139-147, Nauka, Moscow, 1966.
- [56] Muskhelishvili, N.I.: Nekotorye osnovnye zadachi matematicheskoy teorii uprogosti (Some Basic Problems of the Mathematical Theory of Elasticity). Chapter 6 (I), §110: pp. 391-401, Nauka, Moscow, 1966.
- [57] Nemeth, N.N., Powers, L.M., Janosik, L.A., Gyekenyesi, J.P.: CARES/LIFE ceramics analysis and reliability evaluation of structures life prediction program. *Technical report*, NASA/TM-2003-106316, Cleveland, Ohio, 2003.

-
- [58] Neville, D.J., Knott, J.: Statistical distributions of toughness and fracture stress for homogeneous and inhomogeneous materials. *Journal of the Mechanics and Physics of Solids* 34(3), pp. 243–291, 1986.
- [59] Oechsner, M., Hillman, C., Lange, F.F.: Crack bifurcation in laminar ceramic composites. *Journal of the American Ceramic Society* 79(7), pp. 1834–1838, 1996.
- [60] Poncelet, M., Doudard, C., Calloch, S., Weber, B., Hild, F.: Probabilistic multiscale models and measurements of self-heating under multiaxial high cycle fatigue. *Journal of the Mechanics and Physics of Solids* 58(4), pp. 578–593, 2010.
- [61] Rice, J.: Elastic fracture mechanics concepts for interfacial cracks. *Journal of Applied Mechanics, TRANS. ASME* 55, pp. 98–103, 1988.
- [62] Riesch-Oppermann, H., Härtelt, M., Kraft, O.: STAU - a review of the Karlsruhe weakest link finite element postprocessor with extensive capabilities. *International Journal of Materials Research* 99(10), pp. 1055–1065, 2008.
- [63] Suga, T., Elssner, G., Schmauder, S.: Composite parameters and mechanical compatibility of material joints. *Journal of Composite Materials* 22(10), pp. 917–934, 1988.
- [64] Tahir, A.M.: Fracture mechanics characterization of ceramics-ceramics interfaces. Master's thesis, Friedrich Alexander Universität Erlangen-Nürnberg, 2010.
- [65] Texarkana Orthopedics: Joint replacements. online: www.texarkanaortho.com/joint-replacement/, accessed 07.02.2011.
- [66] Tong, J.: Interfacial fracture toughness of synthetic bone-cement interface. *Key engineering materials* 312, pp. 251–256, 2006.
- [67] Tranter, C.J.: Integral transforms in mathematical physics. Chapter 3: pp. 32–45, Methuen, London/ Wiley, New York, 1956.

- [68] Turner, M., Dalgleish, B., He, M., Evans, A.: A fracture resistance measurement method for bimaterial interfaces having large debond energy. *Acta Metallurgica et Materialia* 43(9), pp. 3459–3465, 1995.
- [69] Vardar, O., Finnie, I.: An analysis of the Brazilian disk fracture test using the Weibull probabilistic treatment of brittle strength. *International Journal of Fracture* 11(3), pp. 495–508, 1975.
- [70] Weibull, W.: A statistical theory of the strength of materials. *Ingeniorsvetenskapsakademiens Handlingar* 151, pp. 1–45, 1939.
- [71] Williams, M.L.: The stresses around a fault or crack in dissimilar media. *Bulletin of the Seismological Society of America* 49(2), pp. 199–204, 1959.
- [72] Wu, S.J., Knott, J.F.: On the statistical analysis of local fracture stresses in notched bars. *Journal of the Mechanics and Physics of Solids* 52(4), pp. 907–924, 2004.
- [73] Yahsi, O., Gocmen, A.: Contact problem for two perfectly bonded dissimilar infinite strips. *International Journal of Fracture* 34, pp. 161–177, 1987.
- [74] Ziegler, C.: Bewertung der Zuverlässigkeit keramischer Komponenten bei zeitlich veränderlichen Spannungen und bei Hochtemperaturbelastung. Ph.D. thesis, Universität Karlsruhe (TH), 1998.
- [75] Zweben, C., Rosen, B.W.: A statistical theory of material strength with application to composite materials. *Journal of the Mechanics and Physics of Solids* 18(3), pp. 189–206, 1970.

Appendix A

For the upper material the expressions of integral kernels are listed below:

1) Integral kernels in formula (4.13) for the derivative of displacements $\frac{\partial U_1^{(1)}}{\partial x_1}$ are:

$$A_1^{(1)}(x_1, x_2, \tau) = \frac{1}{4h_1\mu_1(\lambda_1 + 2\mu_1)} \left\{ 2\mu_1 \left[\frac{\sinh(\eta_1[x_1 + \tau])}{\cosh(\eta_1[x_1 + \tau]) + \cos(\eta_1 x_2)} - \frac{\sinh(\eta_1[x_1 - \tau])}{\cosh(\eta_1[x_1 - \tau]) + \cos(\eta_1 x_2)} \right] - \right. \\ \left. -\eta_1(\lambda_1 + \mu_1) \left[\frac{(x_1 + \tau)[1 + \cos(\eta_1 x_2) \cosh(\eta_1[x_1 + \tau])]}{[\cos(\eta_1 x_2) + \cosh(\eta_1[x_1 + \tau])]^2} - \frac{(x_1 - \tau)[1 + \cos(\eta_1 x_2) \cosh(\eta_1[x_1 - \tau])]}{[\cos(\eta_1 x_2) + \cosh(\eta_1[x_1 - \tau])]^2} \right] \right\}$$

$$B_1^{(1)}(x_1, x_2, \tau) = \frac{1}{2h_1(\lambda_1 + 2\mu_1)} \left\{ \lambda_1 \left[\frac{\sinh(\eta_1[x_1 + \tau])}{\cosh(\eta_1[x_1 + \tau]) + \cos(\eta_1 x_2)} - \frac{\sinh(\eta_1[x_1 - \tau])}{\cosh(\eta_1[x_1 - \tau]) + \cos(\eta_1 x_2)} \right] + \right. \\ \left. +\eta_1(\lambda_1 + \mu_1) \left[\frac{(x_1 + \tau)[1 + \cos(\eta_1 x_2) \cosh(\eta_1[x_1 + \tau])]}{[\cos(\eta_1 x_2) + \cosh(\eta_1[x_1 + \tau])]^2} - \frac{(x_1 - \tau)[1 + \cos(\eta_1 x_2) \cosh(\eta_1[x_1 - \tau])]}{[\cos(\eta_1 x_2) + \cosh(\eta_1[x_1 - \tau])]^2} \right] \right\}$$

$$C_1^{(1)}(x_1, x_2, \tau) = \frac{1}{4h_1\mu_1(\lambda_1 + 2\mu_1)} \left\{ -2\mu_1 \left[\frac{\sinh(\eta_1[x_1 + \tau])}{\cosh(\eta_1[x_1 + \tau]) - \cos(\eta_1 x_2)} - \frac{\sinh(\eta_1[x_1 - \tau])}{\cosh(\eta_1[x_1 - \tau]) - \cos(\eta_1 x_2)} \right] + \right. \\ \left. +\eta_1(\lambda_1 + \mu_1) \left[\frac{(x_1 + \tau)[1 - \cos(\eta_1 x_2) \cosh(\eta_1[x_1 + \tau])]}{[\cos(\eta_1 x_2) - \cosh(\eta_1[x_1 + \tau])]^2} - \frac{(x_1 - \tau)[1 - \cos(\eta_1 x_2) \cosh(\eta_1[x_1 - \tau])]}{[\cos(\eta_1 x_2) - \cosh(\eta_1[x_1 - \tau])]^2} \right] \right\}$$

$$D_1^{(1)}(x_1, x_2, \tau) = \frac{1}{2h_1(\lambda_1 + 2\mu_1)} \left\{ -\lambda_1 \left[\frac{\sinh(\eta_1[x_1 + \tau])}{\cosh(\eta_1[x_1 + \tau]) - \cos(\eta_1 x_2)} - \frac{\sinh(\eta_1[x_1 - \tau])}{\cosh(\eta_1[x_1 - \tau]) - \cos(\eta_1 x_2)} \right] - \right. \\ \left. -\eta_1(\lambda_1 + \mu_1) \left[\frac{(x_1 + \tau)[1 - \cos(\eta_1 x_2) \cosh(\eta_1[x_1 + \tau])]}{[\cos(\eta_1 x_2) - \cosh(\eta_1[x_1 + \tau])]^2} - \frac{(x_1 - \tau)[1 - \cos(\eta_1 x_2) \cosh(\eta_1[x_1 - \tau])]}{[\cos(\eta_1 x_2) - \cosh(\eta_1[x_1 - \tau])]^2} \right] \right\}$$

2) Integral kernels in formula (4.14) for the derivative of displacements $\frac{\partial U_2^{(1)}}{\partial x_2}$ are:

$$A_2^{(1)}(x_1, x_2, \tau) = \frac{\eta_1(\lambda_1 + \mu_1)}{4h_1\mu_1(\lambda_1 + 2\mu_1)} \left\{ \frac{(x_1 + \tau)[1 + \cos(\eta_1 x_2) \cosh(\eta_1[x_1 + \tau])]}{[\cos(\eta_1 x_2) + \cosh(\eta_1[x_1 + \tau])]^2} - \frac{(x_1 - \tau)[1 + \cos(\eta_1 x_2) \cosh(\eta_1[x_1 - \tau])]}{[\cos(\eta_1 x_2) + \cosh(\eta_1[x_1 - \tau])]^2} \right\}$$

$$B_2^{(1)}(x_1, x_2, \tau) = \frac{-1}{2h_1(\lambda_1 + 2\mu_1)} \left\{ (\lambda_1 + 2\mu_1) \left[\frac{\sinh(\eta_1[x_1 + \tau])}{\cosh(\eta_1[x_1 + \tau]) + \cos(\eta_1 x_2)} - \frac{\sinh(\eta_1[x_1 - \tau])}{\cosh(\eta_1[x_1 - \tau]) + \cos(\eta_1 x_2)} \right] + \eta_1(\lambda_1 + \mu_1) \left[\frac{(x_1 + \tau)[1 + \cos(\eta_1 x_2) \cosh(\eta_1[x_1 + \tau])]}{[\cos(\eta_1 x_2) + \cosh(\eta_1[x_1 + \tau])]^2} - \frac{(x_1 - \tau)[1 + \cos(\eta_1 x_2) \cosh(\eta_1[x_1 - \tau])]}{[\cos(\eta_1 x_2) + \cosh(\eta_1[x_1 - \tau])]^2} \right] \right\}$$

$$C_2^{(1)}(x_1, x_2, \tau) = \frac{-\eta_1(\lambda_1 + \mu_1)}{4h_1\mu_1(\lambda_1 + 2\mu_1)} \left\{ \frac{(x_1 + \tau)[1 - \cos(\eta_1 x_2) \cosh(\eta_1[x_1 + \tau])]}{[\cos(\eta_1 x_2) - \cosh(\eta_1[x_1 + \tau])]^2} - \frac{(x_1 - \tau)[1 - \cos(\eta_1 x_2) \cosh(\eta_1[x_1 - \tau])]}{[\cos(\eta_1 x_2) - \cosh(\eta_1[x_1 - \tau])]^2} \right\}$$

$$D_2^{(1)}(x_1, x_2, \tau) = \frac{-1}{2h_1(\lambda_1 + 2\mu_1)} \left\{ -(\lambda_1 + 2\mu_1) \left[\frac{\sinh(\eta_1[x_1 + \tau])}{\cosh(\eta_1[x_1 + \tau]) - \cos(\eta_1 x_2)} - \frac{\sinh(\eta_1[x_1 - \tau])}{\cosh(\eta_1[x_1 - \tau]) - \cos(\eta_1 x_2)} \right] - \eta_1(\lambda_1 + \mu_1) \left[\frac{(x_1 + \tau)[1 - \cos(\eta_1 x_2) \cosh(\eta_1[x_1 + \tau])]}{[\cos(\eta_1 x_2) - \cosh(\eta_1[x_1 + \tau])]^2} - \frac{(x_1 - \tau)[1 - \cos(\eta_1 x_2) \cosh(\eta_1[x_1 - \tau])]}{[\cos(\eta_1 x_2) - \cosh(\eta_1[x_1 - \tau])]^2} \right] \right\}$$

3) Integral kernels in formula (4.15) for stress component $\sigma_{22}^{(1)}$ can be calculated as:

$$A_3^{(1)}(x_1, x_2, \tau) = \lambda_1 A_1^{(1)}(x_1, x_2, \tau) + (\lambda_1 + 2\mu_1) A_2^{(1)}(x_1, x_2, \tau)$$

$$B_3^{(1)}(x_1, x_2, \tau) = \lambda_1 B_1^{(1)}(x_1, x_2, \tau) + (\lambda_1 + 2\mu_1) B_2^{(1)}(x_1, x_2, \tau)$$

$$C_3^{(1)}(x_1, x_2, \tau) = \lambda_1 C_1^{(1)}(x_1, x_2, \tau) + (\lambda_1 + 2\mu_1) C_2^{(1)}(x_1, x_2, \tau)$$

$$D_3^{(1)}(x_1, x_2, \tau) = \lambda_1 D_1^{(1)}(x_1, x_2, \tau) + (\lambda_1 + 2\mu_1) D_2^{(1)}(x_1, x_2, \tau)$$

For the lower material, similar to Eq. (4.14) and (4.15) the expressions for the derivatives of displacements are:

$$\begin{aligned} \frac{\partial u_1^{(2)}}{\partial x_1}(x_1, x_2) &= \int_0^{\infty} g_3(\tau) A_1^{(2)}(x_1, x_2, \tau) d\tau + \int_0^{\infty} g_4'(\tau) B_1^{(2)}(x_1, x_2, \tau) d\tau + \\ &+ \int_0^{\infty} f_1(\tau) C_1^{(2)}(x_1, x_2, \tau) d\tau + \int_0^{\infty} f_2'(\tau) D_1^{(2)}(x_1, x_2, \tau) d\tau \end{aligned} \quad (\text{A.1})$$

and

$$\begin{aligned} \frac{\partial u_2^{(2)}}{\partial x_2}(x_1, x_2) &= \int_0^{\infty} g_3(\tau) A_2^{(2)}(x_1, x_2, \tau) d\tau + \int_0^{\infty} g_4'(\tau) B_2^{(2)}(x_1, x_2, \tau) d\tau + \\ &+ \int_0^{\infty} f_1(\tau) C_2^{(2)}(x_1, x_2, \tau) d\tau + \int_0^{\infty} f_2'(\tau) D_2^{(2)}(x_1, x_2, \tau) d\tau \end{aligned} \quad (\text{A.2})$$

With the integral kernels listed below.

Therefore, the normal stress component can be rewritten in the following way:

$$\begin{aligned} \sigma_{22}^{(2)}(x_1, x_2) &= \int_0^{\infty} g_3(\tau) A_3^{(2)}(x_1, x_2, \tau) d\tau + \int_0^{\infty} g_4'(\tau) B_3^{(2)}(x_1, x_2, \tau) d\tau + \\ &+ \int_0^{\infty} f_1(\tau) C_3^{(2)}(x_1, x_2, \tau) d\tau + \int_0^{\infty} f_2'(\tau) D_3^{(2)}(x_1, x_2, \tau) d\tau, \end{aligned} \quad (\text{A.3})$$

1) Integral kernels for the derivative of displacements $\frac{\partial U_1^{(2)}}{\partial x_1}$ are:

$$A_1^{(2)}(x_1, x_2, \tau) = \frac{1}{4h_2\mu_2(\lambda_2 + 2\mu_2)} \left\{ -2\mu_2 \left[\frac{\sinh(\eta_2[x_1 + \tau])}{\cosh(\eta_2[x_1 + \tau]) - \cos(\eta_2[x_2 + h_2])} - \frac{\sinh(\eta_2[x_1 - \tau])}{\cosh(\eta_2[x_1 - \tau]) - \cos(\eta_2[x_2 + h_2])} \right] \right\} +$$

$$\begin{aligned}
 & +\eta_2(\lambda_2 + \mu_2) \left\{ \frac{(x_1 + \tau)[1 - \cos(\eta_2[x_2 + h_2]) \cosh(\eta_2[x_1 + \tau])]}{[\cos(\eta_2[x_2 + h_2]) - \cosh(\eta_2[x_1 + \tau])]^2} - \right. \\
 & \quad \left. - \frac{(x_1 - \tau)[1 - \cos(\eta_2[x_2 + h_2]) \cosh(\eta_2[x_1 - \tau])]}{[\cos(\eta_2[x_2 + h_2]) - \cosh(\eta_2[x_1 - \tau])]^2} \right\} \\
 B_1^{(2)}(x_1, x_2, \tau) = & \frac{1}{2h_2(\lambda_2 + 2\mu_2)} \left\{ -\lambda_2 \left[\frac{\sinh(\eta_2[x_1 + \tau])}{\cosh(\eta_2[x_1 + \tau]) - \cos(\eta_2[x_2 + h_2])} - \right. \right. \\
 & \quad \left. \left. - \frac{\sinh(\eta_2[x_1 - \tau])}{\cosh(\eta_2[x_1 - \tau]) - \cos(\eta_2[x_2 + h_2])} \right] - \right. \\
 & \quad \left. -\eta_2(\lambda_2 + \mu_2) \left[\frac{(x_1 + \tau)[1 - \cos(\eta_2[x_2 + h_2]) \cosh(\eta_2[x_1 + \tau])]}{[\cos(\eta_2[x_2 + h_2]) - \cosh(\eta_2[x_1 + \tau])]^2} - \right. \right. \\
 & \quad \left. \left. - \frac{(x_1 - \tau)[1 - \cos(\eta_2[x_2 + h_2]) \cosh(\eta_2[x_1 - \tau])]}{[\cos(\eta_2[x_2 + h_2]) - \cosh(\eta_2[x_1 - \tau])]^2} \right] \right\} \\
 C_1^{(2)}(x_1, x_2, \tau) = & \frac{1}{4h_2\mu_2(\lambda_2 + 2\mu_2)} \left\{ 2\mu_2 \left[\frac{\sinh(\eta_2[x_1 + \tau])}{\cosh(\eta_2[x_1 + \tau]) + \cos(\eta_2[x_2 + h_2])} - \right. \right. \\
 & \quad \left. \left. - \frac{\sinh(\eta_2[x_1 - \tau])}{\cosh(\eta_2[x_1 - \tau]) + \cos(\eta_2[x_2 + h_2])} \right] - \right. \\
 & \quad \left. -\eta_2(\lambda_2 + \mu_2) \left[\frac{(x_1 + \tau)[1 + \cos(\eta_2[x_2 + h_2]) \cosh(\eta_2[x_1 + \tau])]}{[\cos(\eta_2[x_2 + h_2]) + \cosh(\eta_2[x_1 + \tau])]^2} - \right. \right. \\
 & \quad \left. \left. - \frac{(x_1 - \tau)[1 + \cos(\eta_2[x_2 + h_2]) \cosh(\eta_2[x_1 - \tau])]}{[\cos(\eta_2[x_2 + h_2]) + \cosh(\eta_2[x_1 - \tau])]^2} \right] \right\} \\
 D_1^{(2)}(x_1, x_2, \tau) = & \frac{1}{2h_2(\lambda_2 + 2\mu_2)} \left\{ \lambda_2 \left[\frac{\sinh(\eta_2[x_1 + \tau])}{\cosh(\eta_2[x_1 + \tau]) + \cos(\eta_2[x_2 + h_2])} - \right. \right. \\
 & \quad \left. \left. - \frac{\sinh(\eta_2[x_1 - \tau])}{\cosh(\eta_2[x_1 - \tau]) + \cos(\eta_2[x_2 + h_2])} \right] + \right. \\
 & \quad \left. +\eta_2(\lambda_2 + \mu_2) \left[\frac{(x_1 + \tau)[1 + \cos(\eta_2[x_2 + h_2]) \cosh(\eta_2[x_1 + \tau])]}{[\cos(\eta_2[x_2 + h_2]) + \cosh(\eta_2[x_1 + \tau])]^2} - \right. \right. \\
 & \quad \left. \left. - \frac{(x_1 - \tau)[1 + \cos(\eta_2[x_2 + h_2]) \cosh(\eta_2[x_1 - \tau])]}{[\cos(\eta_2[x_2 + h_2]) + \cosh(\eta_2[x_1 - \tau])]^2} \right] \right\}
 \end{aligned}$$

2) Integral kernels for the derivative of displacements $\frac{\partial U_2^{(2)}}{\partial x_2}$ are:

$$A_2^{(2)}(x_1, x_2, \tau) = \frac{-\eta_2(\lambda_2 + \mu_2)}{4h_2\mu_2(\lambda_2 + 2\mu_2)} \left\{ \frac{(x_1 + \tau)[1 - \cos(\eta_2[x_2 + h_2])\cosh(\eta_2[x_1 + \tau])]}{[\cos(\eta_2[x_2 + h_2]) - \cosh(\eta_2[x_1 + \tau])]^2} - \frac{(x_1 - \tau)[1 - \cos(\eta_2[x_2 + h_2])\cosh(\eta_2[x_1 - \tau])]}{[\cos(\eta_2[x_2 + h_2]) - \cosh(\eta_2[x_1 - \tau])]^2} \right\}$$

$$B_2^{(2)}(x_1, x_2, \tau) = \frac{-1}{2h_2(\lambda_2 + 2\mu_2)} \left\{ -(\lambda_2 + 2\mu_2) \left[\frac{\sinh(\eta_2[x_1 + \tau])}{\cosh(\eta_2[x_1 + \tau]) - \cos(\eta_2[x_2 + h_2])} - \frac{\sinh(\eta_2[x_1 - \tau])}{\cosh(\eta_2[x_1 - \tau]) - \cos(\eta_2[x_2 + h_2])} \right] - \eta_2(\lambda_2 + \mu_2) \left[\frac{(x_1 + \tau)[1 - \cos(\eta_2[x_2 + h_2])\cosh(\eta_2[x_1 + \tau])]}{[\cos(\eta_2[x_2 + h_2]) - \cosh(\eta_2[x_1 + \tau])]^2} - \frac{(x_1 - \tau)[1 - \cos(\eta_2[x_2 + h_2])\cosh(\eta_2[x_1 - \tau])]}{[\cos(\eta_2[x_2 + h_2]) - \cosh(\eta_2[x_1 - \tau])]^2} \right] \right\}$$

$$C_2^{(2)}(x_1, x_2, \tau) = \frac{\eta_2(\lambda_2 + \mu_2)}{4h_2\mu_2(\lambda_2 + 2\mu_2)} \left\{ \frac{(x_1 + \tau)[1 + \cos(\eta_2[x_2 + h_2])\cosh(\eta_2[x_1 + \tau])]}{[\cos(\eta_2[x_2 + h_2]) + \cosh(\eta_2[x_1 + \tau])]^2} - \frac{(x_1 - \tau)[1 + \cos(\eta_2[x_2 + h_2])\cosh(\eta_2[x_1 - \tau])]}{[\cos(\eta_2[x_2 + h_2]) + \cosh(\eta_2[x_1 - \tau])]^2} \right\}$$

$$D_2^{(2)}(x_1, x_2, \tau) = \frac{-1}{2h_2(\lambda_2 + 2\mu_2)} \left\{ (\lambda_2 + 2\mu_2) \left[\frac{\sinh(\eta_2[x_1 + \tau])}{\cosh(\eta_2[x_1 + \tau]) + \cos(\eta_2[x_2 + h_2])} - \frac{\sinh(\eta_2[x_1 - \tau])}{\cosh(\eta_2[x_1 - \tau]) + \cos(\eta_2[x_2 + h_2])} \right] + \eta_2(\lambda_2 + \mu_2) \left[\frac{(x_1 + \tau)[1 + \cos(\eta_2[x_2 + h_2])\cosh(\eta_2[x_1 + \tau])]}{[\cos(\eta_2[x_2 + h_2]) + \cosh(\eta_2[x_1 + \tau])]^2} - \frac{(x_1 - \tau)[1 + \cos(\eta_2[x_2 + h_2])\cosh(\eta_2[x_1 - \tau])]}{[\cos(\eta_2[x_2 + h_2]) + \cosh(\eta_2[x_1 - \tau])]^2} \right] \right\}$$

3) Integral kernels in the expression of the stress component $\sigma_{22}^{(2)}$ are obtained in the same way as it was shown in paragraph 3) for the upper material by simple change of indexes of material number.

Thus, system of integral singular equations (4.16) can be presented in an expanded form:

$$\left\{ \begin{aligned}
 & \int_0^{\infty} \left[g_1(\tau)A_3^{(1)}(x_1, h_1, \tau) + g_2'(\tau)B_3^{(1)}(x_1, h_1, \tau) + f_1(\tau)C_3^{(1)}(x_1, h_1, \tau) + \right. \\
 & \qquad \qquad \qquad \left. + f_2'(\tau)D_3^{(1)}(x_1, h_1, \tau) d\tau \right] = P(x_1) \\
 & \int_0^{\infty} \left[g_3(\tau)A_3^{(2)}(x_1, -h_2, \tau) + g_4'(\tau)B_3^{(2)}(x_1, -h_2, \tau) + f_1(\tau)C_3^{(2)}(x_1, -h_2, \tau) + \right. \\
 & \qquad \qquad \qquad \left. + f_2'(\tau)D_3^{(2)}(x_1, -h_2, \tau) d\tau \right] = -P(x_1) \\
 & \int_0^{\infty} \left[g_1(\tau)A_3^{(1)}(x_1, 0, \tau) + g_2'(\tau)B_3^{(1)}(x_1, 0, \tau) + f_1(\tau)(C_3^{(1)}(x_1, 0, \tau) - C_3^{(2)}(x_1, 0, \tau)) + \right. \\
 & \qquad \qquad \qquad \left. + f_2'(\tau)(D_3^{(1)}(x_1, 0, \tau) - D_3^{(2)}(x_1, 0, \tau)) - g_4'(\tau)B_3^{(2)}(x_1, 0, \tau) - g_3(\tau)A_3^{(2)}(x_1, 0, \tau) \right] d\tau = 0 \\
 & \int_0^{\infty} \left[g_1(\tau)A_1^{(1)}(x_1, 0, \tau) + g_2'(\tau)B_1^{(1)}(x_1, 0, \tau) + f_1(\tau)(C_1^{(1)}(x_1, 0, \tau) - C_1^{(2)}(x_1, 0, \tau)) + \right. \\
 & \qquad \qquad \qquad \left. + f_2'(\tau)(D_1^{(1)}(x_1, 0, \tau) - D_1^{(2)}(x_1, 0, \tau)) - g_4'(\tau)B_1^{(2)}(x_1, 0, \tau) - g_3(\tau)A_1^{(2)}(x_1, 0, \tau) \right] d\tau = 0
 \end{aligned} \right.$$

Appendix B

Under equivalent stress we understand tensile stress acting in the component, which produces the same interface energy release rate as a mixed-mode stress state (see [Figure B.1](#)).

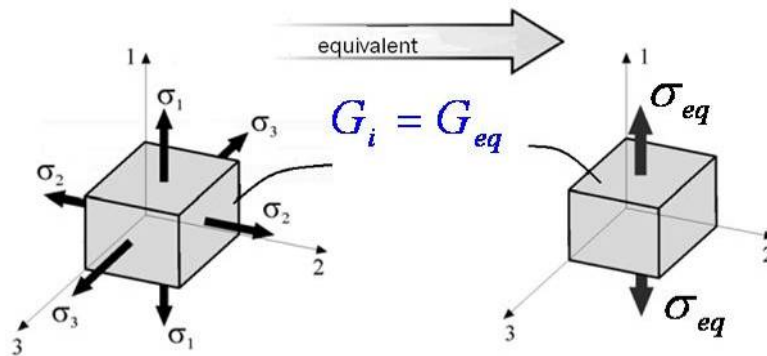


Figure B.1 - Equivalent stress criteria

The presentation of equivalent stresses through normal and shear stress components acting on the interface can be obtained from equation

$$G_{eq} = G_i, \quad (\text{B.1})$$

furthermore the interface energy release rate G_i determined in 3D case as :

$$G_i = \frac{1}{H_1} (K_1^2 + K_2^2) + \frac{1}{H_2} K_{III}^2 \quad (\text{B.2})$$

For “through-wall” crack model complex stress intensity factor K and real stress intensity factor K_{III} are:

$$K_1 + iK_2 = (1 + 2i\varepsilon)(\sigma_n + i\sigma_{\tau 1})\sqrt{\frac{\pi a}{2}}(a)^{-i\varepsilon} \quad (\text{B.3})$$

$$K_{III} = \sqrt{\frac{\pi a}{2}}\sigma_{\tau 2} \quad (\text{B.4})$$

Taking into account that $a^{-i\varepsilon} = \cos(\varepsilon \ln a) - i\sin(\varepsilon \ln a)$ and separating real and imaginary parts in equation (B.3), one will get:

$$K_1 = \sqrt{\frac{\pi a}{2}} \left[(\cos(\varepsilon \ln a) + 2\varepsilon \sin(\varepsilon \ln a))\sigma_n - (2\varepsilon \cos(\varepsilon \ln a) - \sin(\varepsilon \ln a))\sigma_{\tau 1} \right]$$

$$K_2 = \sqrt{\frac{\pi a}{2}} \left[(2\varepsilon \cos(\varepsilon \ln a) - \sin(\varepsilon \ln a))\sigma_n + (\cos(\varepsilon \ln a) + 2\varepsilon \sin(\varepsilon \ln a))\sigma_{\tau 1} \right]$$

Consequently,

$$\begin{aligned} K_1^2 + K_2^2 &= \frac{\pi a}{2} \left[\sigma_n^2 (\cos^2(\varepsilon \ln a) + 4\varepsilon^2 \sin^2(\varepsilon \ln a) + 4\varepsilon \sin(\varepsilon \ln a) \cos(\varepsilon \ln a)) + \right. \\ &\quad + \sigma_{\tau 1}^2 (\sin^2(\varepsilon \ln a) + 4\varepsilon^2 \cos^2(\varepsilon \ln a) - 4\varepsilon \sin(\varepsilon \ln a) \cos(\varepsilon \ln a)) - \\ &\quad - 2\sigma_n \sigma_{\tau 1} (2\varepsilon \cos^2(\varepsilon \ln a) - \sin(\varepsilon \ln a) \cos(\varepsilon \ln a) - \\ &\quad \quad \quad - 2\varepsilon \sin^2(\varepsilon \ln a) + 4\varepsilon^2 \sin(\varepsilon \ln a) \cos(\varepsilon \ln a)) + \\ &\quad + \sigma_n^2 (4\varepsilon^2 \cos^2(\varepsilon \ln a) + \sin^2(\varepsilon \ln a) - 4\varepsilon \sin(\varepsilon \ln a) \cos(\varepsilon \ln a)) + \\ &\quad + \sigma_{\tau 1}^2 (\cos^2(\varepsilon \ln a) + 4\varepsilon^2 \sin^2(\varepsilon \ln a) + 4\varepsilon \sin(\varepsilon \ln a) \cos(\varepsilon \ln a)) + \\ &\quad - 2\sigma_n \sigma_{\tau 1} (-2\varepsilon \sin^2(\varepsilon \ln a) - \sin(\varepsilon \ln a) \cos(\varepsilon \ln a) - \\ &\quad \quad \quad + 2\varepsilon \cos^2(\varepsilon \ln a) + 4\varepsilon^2 \sin(\varepsilon \ln a) \cos(\varepsilon \ln a)) \left. \right] = \\ &= \frac{\pi a}{2} (1 + 4\varepsilon^2) (\sigma_n^2 + \sigma_{\tau 1}^2) \end{aligned}$$

$$K_{III}^2 = \frac{\pi a}{2} \sigma_{\tau 2}^2$$

Thus, the latter two equations and (B.2) yield the following expression of interface energy release rate:

$$G_i = \frac{1}{H_1} \frac{\pi a}{2} (1 + 4\varepsilon^2) (\sigma_n^2 + \sigma_{\tau 1}^2) + \frac{1}{H_2} \frac{\pi a}{2} \sigma_{\tau 2}^2 \quad (\text{B.5})$$

On the other hand, equivalent stresses cause the following iERR:

$$G_{eq} = \frac{1}{H_1} \frac{\pi a}{2} (1 + 4\varepsilon^2) \sigma_{eq}^2 \quad (\text{B.6})$$

According to criteria (B.1) from equations (B.5) and (B.6) equivalent stress can be found as a combination of normal and shear stress acting along the crack line as:

$$\sigma_{eq} = \sqrt{\sigma_n^2 + \sigma_{\tau 1}^2 + \frac{H_1}{(1 + 4\varepsilon^2)H_2} \sigma_{\tau 2}^2}, \quad (\text{B.7})$$

For “penny-shaped” crack model complex stress intensity factor K and real stress intensity factor K_{III} are [28, 38]:

$$\begin{aligned} K_I + iK_2 &= 2\sqrt{\frac{a}{2}} \frac{\Gamma(2 + i\varepsilon)}{\Gamma(0.5 + i\varepsilon)} (a)^{-i\varepsilon} [\sigma_n + iY_{II} \sigma_{\tau 3} \cos \theta] \\ K_{III} &= 2\sqrt{\frac{a}{2}} Y_{III} \sigma_{\tau 3} \sin \theta \end{aligned} \quad (\text{B.8})$$

where $\Gamma(\varepsilon)$ is the gamma function, and parameters γ , Y_{II} and Y_{III} depend on elastic properties of joined materials:

$$\begin{aligned} \gamma &= \frac{\mu_1 + \mu_2}{4\mu_2(1 - \nu_1) + 4\mu_1(1 - \nu_2)}, \\ Y_{II} &= \frac{8\gamma\beta}{4\gamma\beta - (1 - \beta^2)\pi\varepsilon(1 + \varepsilon^2)}, \\ Y_{III} &= \frac{(1 - \beta^2)\varepsilon(1 + \varepsilon^2)}{4\gamma\beta - (1 - \beta^2)\pi\varepsilon(1 + \varepsilon^2)}. \end{aligned}$$

Repeating the same procedure as described above, one will obtain:

$$G_i = \frac{4a}{2H_1} \left| \frac{\Gamma(2+i\varepsilon)}{\Gamma(0.5+i\varepsilon)} \right|^2 \left(\sigma_n^2 + Y_{II}^2 \sigma_{\tau_3}^2 \cos^2 \theta \right) + \frac{4a}{2H_2} Y_{III}^2 \sigma_{\tau_3}^2 \sin^2 \theta \quad (\text{B.9})$$

and

$$G_{eq} = \frac{4a}{2H_1} \left| \frac{\Gamma(2+i\varepsilon)}{\Gamma(0.5+i\varepsilon)} \right|^2 \sigma_{eq}^2 \quad (\text{B.10})$$

Equations (B.9) and (B.10) lead to the following presentation of equivalent stresses:

$$\sigma_{eq} = \sqrt{\sigma_n^2 + Y_{II}^2 \sigma_{\tau_3}^2 \cos^2 \theta + \frac{H_1}{|\Gamma(2+i\varepsilon)/\Gamma(0.5+i\varepsilon)|^2 H_2} Y_{III}^2 \sigma_{\tau_3}^2 \sin^2 \theta} \quad (\text{B.11})$$